Manganese in Indium Arsenide: Charge Switching and Electronic Structure on the Atomic Scale

Dissertation
zur Erlangung des Doktorgrades
im Department Physik
der Universität Hamburg

vorgelegt von
Felix Marczinowski
aus Berlin

Hamburg
2010

Abstract

In this thesis investigations of individual manganese acceptors in the (110) surface of manganese-doped indium arsenide are presented. Acceptors in different embedding depths below the surface were studied by low temperature scanning tunneling microscopy and spectroscopy.

The **charging and decharging** of individual Mn acceptors with the STM tip is demonstrated. It can be detected in topographic measurements as well as in measurements of the current and the differential conductance. In maps of differential conductance voltage dependent rings of increased conductance around acceptors indicate the transition between the neutral and the negative charge state. The observation can be understood when the band-bending in the sample is taken into account. This increased differential conductance is not related to impurity states but can be explained as a compressed host density of states due to the modified local electrical potential between the two charge states. A simple **numerical model** is presented which is able to fully and accurately reproduce the observed effects. The model includes the local band-bending caused by the tip as well as by the impurity charge. The observed effects due to charge switching allow to separately characterize the tip-induced local potential as well as the charge distribution around the impurity.

The **bound hole wave function** of Mn impurities in different depths below the (110) surface is investigated in detail on the atomic scale. It exhibits a surface-related asymmetry in (001)-direction. This asymmetry decreases with increasing depth and vanishes for acceptors more than about ten layers below the surface. Tight-binding model (TBM) calculations show that the asymmetry is not present in a bulk environment and is caused by strain at the reconstructed (110) surface.

Two **excited states** of the acceptor as predicted by TBM calculations are found. They are detected in a spectroscopic measurement which employs controlled band-bending to probe states far away from the tip's Fermi energy. Several effects of the **interaction of impurity and host states** are found. A locally increased valence band density of states is measured, which is caused by the p-d exchange interaction between host states and d-states of the manganese impurity of $V_{\mathrm{pd}} = 2.19\,\mathrm{eV}$, according to TBM calculations. Due to the same reason, the conduction band density of states appears decreased at the acceptor position. Furthermore, there is an anisotropic oscillation of the conduction band density of states around the acceptor position. Tight-binding model calculations show that it is due to conduction band scattering by the neutral acceptor via p-d exchange interaction.

Zusammenfassung

In dieser Arbeit werden Untersuchungen an einzelnen Manganakzeptoren in verschiedenen Tiefen in der (110)-Oberfläche von mangandotiertem Indiumarsenid mittels Rastertunnelmikroskopie und -spektroskopie vorgestellt.

Das reproduzierbare **Laden und Entladen einzelner Dotieratome** durch die Tunnelspitze wird beschrieben. Beobachten läßt sich der Effekt in Messungen der Topographie, des Tunnelstroms und der differentiellen Leitfähigkeit. In Karten der differentiellen Leitfähigkeit erscheint er in Form von spannungsabhängigen Ringen um die Dotieratome, wo ein Akzeptor zwischen dem neutralen und dem einfach negativen Ladungszustand wechselt. Es wird eine Interpretation vorgestellt, die die Beobachtungen als Messung einer verdichteten Leitungsband-Zustandsdichte des Wirtskristalls erklärt. Kerngröße ist die lokale Bandverbiegung, die von der Tunnelspitze und vom Ladungszustand der Störstelle verursacht wird. Basierend auf dieser Interpretation wird ausgehend vom Tersoff-Hamann-Modell des Tunnelstroms ein **numerisches Modell** entwickelt, welches in der Lage ist, die Beobachtungen vollständig wiederzugeben. Auf dieser Grundlage lassen sich aus Messungen Rückschlüsse auf die Form des spitzeninduzierten Potentials, sowie die genaue Ladungsverteilung im Bereich der Störstelle ziehen.

Die **Lochwellenfunktion von Akzeptoren** in unterschiedlichen Tiefen wird systematisch und auf atomarer Längenskala untersucht. Sie weist an der (110)-Oberfläche eine starke Asymmetrie in (001)-Richtung auf, die mit der Tiefe unter der Oberfläche abnimmt und bis etwa zur zehnten Lage verschwindet. Rechnungen im Tight-Binding-Modell (TBM) für Akzeptoren im Volumen zeigen diese starke Asymmetrie nicht. Sie wird als Effekt der Rekonstruktion an der Oberfläche erklärt. Die TBM-Rechnungen ergeben zwei **angeregte Zustände des Akzeptors**, die im Experiment nachgewiesen werden können. Die Messung erfolgt dabei, anders als üblicherweise bei Rastertunnelspektroskopie, weit unterhalb der Spitzen-Fermienergie durch gezieltes Verändern der lokalen Bandverbiegung. Weiterhin werden verschiedene **Wechselwirkungen von Störstellenzuständen mit dem Wirtskristall** beschrieben. Bei negativen Probenspannungen im Leitungsband wird eine erhöhte Zustandsdichte gemessen. Dies ist eine Folge von p-d-Austauschwechselwirkung zwischen sp^3-Zuständen des Valenzbandes und d-Zuständen des Akzeptors, deren Stärke sich aus den TBM-Rechnungen als $V_{\mathrm{pd}} = 2.19\,\mathrm{eV}$ bestimmen läßt. Bei hohen Spannungen im Leitungsband wird eine lokale Unterdrückung der Zustandsdichte im Leitungsband beobachtet, die von anisotropen Oszillationen der Zustandsdichte umgeben ist. Rechnungen zeigen, daß beide Effekte auf p-d-Wechselwirkung zurückzuführen sind.

Contents

Chapter 1

Introduction

1.1 Dilute magnetic semiconductors

Practically all of the digital technologies that surround us and continue to evolve in their astounding exponential progression are based on two types of materials: semiconductors and ferromagnets. Semiconductors form the basis for high-speed logic circuits and short-term, volatile memory, while any non-volatile memory technologies based on semiconductors (e.g. flash memory, EEPROM) are sluggish and demand lots of power. Ferromagnetic materials on the other hand naturally provide storage persistence and high storage densities. But today they are usually found in the form of hard disks, a spinning glass or aluminium disk coated with a ferromagnetic alloy. This technological divide makes a large amount of additional, intermediary technologies necessary. It makes existing solutions slower, larger and more complicated than one would wish. Interestingly, this divide is older than the current technologies. It was already present in early computers made out of discrete logic parts, or even vacuum tubes, which used magnetic core memory.

With the discovery of ferromagnetism in Mn-doped InAs and GaAs[76; 78], a new area of research came into reach that promised to eliminate this gap in a particularly elegant way by combining spin-based and electronic phenomena in a single material. A strong interplay between magnetic and transport properties creates scientifically and technologically very interesting effects. These include gate-controlled ferromagnetism[77; 90], giant planar Hall-effects[99] and highly efficient spin injection across semiconductor interfaces[79; 98].

Ferromagnetic semiconductors have been investigated for quite some time now, and their peculiar spin-related phenomena due to the coexistence of semiconductor properties and magnetism were recognized as early as the 1960's[37; 38]. But the relatively recent successes[78; 106] in manufacturing so-called di-

luted magnetic semiconductors (DMS) based on III-V semiconductors with Curie temperatures as high as 185 K[81] by means of molecular beam epitaxy (MBE) sparked a whole new wave of interest in this class of materials. This is also due to the fact that the host materials' electronic properties are already well understood. So these types of systems are an ideal test bed for basic research to investigate the emergence of magnetic order in dilute systems. At the same time, quick technological utilization seems plausible.

As diluted magnetic semiconductors combine electronic elements with magnetism, without requiring external fields or other magnetic materials, the term spin-electronics or "spintronics" was coined for a range of phenomena appearing in these materials as well as for their technological utilization. As an added technological benefit, these materials can be easily interchanged for or combined with those in use today. The existing technologies for manufacturing semiconductors (crystal growth, handling, lithography, etc.) will continue to work just as well with this new class of materials. For example, combining non-magnetic and magnetic functions on the same die is a possibility.

But despite the huge interest and the progress towards higher Curie temperatures, the emergence of long-range magnetic order in these peculiar materials is still not very well understood. There is a whole range of models of magnetic interaction developed over the last seven or so decades, but how to apply them for a specific material remains a topic of debate. To fully understand magnetism in DMS, profound insight needs to be gained in the nature of local, indirect magnetic exchange interaction. This puts the focus on the atomic-scale properties, specifically the local, atomic-scale electronic structure of single magnetic dopants. Insight gained here will ultimately, through new material combinations, new growth and post-growth techniques etc., lead the way towards the ultimate goal, Curie-temperatures above room temperature.

The scanning tunneling microscope (STM) lends itself to this task particularly well. Atomic-scale features, adsorbed atoms and semiconductor dopants have been studied with the STM since its invention in the 1980's[10–14]. Improvements of stability and precision, as well as the advancement of low-temperature instruments continues to make smaller structures and smaller effects accessible to direct measurement.

1.2 Overview

The primary goal of the research presented in this work is to contribute to an accurate atomic-scale understanding of transition-metal dopants in InAs and other III-V semiconductors. The tool used to this end is low-temperature scanning tunneling microscopy, a local method of probing electronic states with unsurpassed spatial resolution.

We use this technique to investigate individual manganese dopants embedded in indium arsenide crystals. Manganese provides the localized magnetic moments and at the same time acts as an acceptor providing charge carriers. Manganese-

doped indium arsenide was chosen for several experimental advantages and for the fact that it is commercially readily available.

Chapter 2 introduces diluted magnetic semiconductors and the considerations regarding the origins of magnetic ordering. There, the general concepts needed to describe electronic and magnetic effects will be given. Next, in Chapter 3 the experimental method scanning tunneling microscopy will be introduced with its possibilities and properties. The terms and concepts necessary for later experimental chapters will be developed. Also, the idea of tip-induced band-bending in an STM experiment is explained, which lays the foundation for the analysis in Chapter 5. A description of the experimental facilities is also given here. Chapter 4 is devoted to the preparation and basic characterization of our samples. In its course, techniques to characterize individual dopant atoms in the surface will be developed, which are a prerequisite for the subsequent analyses.

Chapter 5 then focuses on our observation of two different charge states of the acceptors and how they can be controlled with the STM probe. Building on the ideas of tip-induced band-bending, a simple theoretical model is developed which is able to fully reproduce the experimental observations. After establishing the validity of the model, we can use it to separately infer sample properties, namely the screening behavior, and tip properties, i.e. the tip-induced potential, from our measurements.

Chapter 6 presents our findings related to the acceptor state and its wave function. The role of the indium arsenide surface reconstruction in warping the wave function is investigated and experimental evidence for the spin-orbit splitting of the acceptor state is presented. Finally, the acceptor's effect on the host bands will be discussed.

Chapter 2

Dilute magnetic semiconductors and (In,Mn)As

> One shouldn't work on semiconductors, that is a filthy mess; who knows if they really exist!
>
> Wolfgang Pauli (1931)

This chapter introduces the topic of dilute magnetic semiconductors and our sample system, manganese-doped indium arsenide. The theoretical approaches to the nature and properties of such materials and the Mn-acceptor will be presented. The different ways of describing the magnetic ordering are introduced as well as the controversy surrounding it. Finally, an overview is given of existing experimental work on systems of this type and the current state of knowledge and how our findings relate to it.

2.1   Dilute magnetic semiconductors

There is a rather wide range of semiconducting materials with embedded magnetic atoms, which can exhibit magnetic phenomena and which are commonly called dilute magnetic semiconductors[*]. Among them are II-VI materials such as e.g. CdSe, CdTe, ZnSe with Fe, Mn or Co as the magnetic dopant substituting for cations, or IV-VI compounds like PbTe and SnTe, as well as III-V compounds like InAs, GaAs and InSb[35; 52]. Rare-earth elements like Eu, Gd and Er have also been used as magnetic dopants. III-V-based materials have attracted the most attention, due to the prevalence of III-V materials in research as well as in applications and due to the fact that here, transition metals not only add magnetic

---

[*]sometimes "diluted magnetic semiconductors"

moments but also act as dopants providing charge carriers to the material which mediate the ferromagnetic ordering.

To achieve magnetic cooperative phenomena, a sizable amount (a few percent) of a magnetic element has to be incorporated into the semiconductor. Such an amount is beyond the solubility limit in III-V semiconductors and new growth methods like low-temperature molecular beam epitaxy (LT-MBE) had to be developed to address this issue. These methods could achieve non-equilibrium growth as well as suppress segregation and the formation of second phases, like MnAs clusters.

Reports of the first successful fabrication of (In,Mn)As by molecular beam epitaxy (MBE) in 1989[76] and later of ferromagnetic (Ga,Mn)As with a Curie temperature of 60 K in 1996[78] generated significant new interest, especially in manganese-doped III-V semiconductors. Both the structure and the electronic properties of these host materials are well known, which makes them ideal systems for studying i.e. the onset and emergence of ferromagnetism in dilute systems. Also, a search for high-T_C materials was sparked, in addition to extensive theoretical work on the occurrence and properties of magnetic ordering.

2.1.1   Origin of magnetic order

The long range magnetic ordering appears at such low concentrations of magnetic dopants that direct exchange interactions can not explain the origins of ferromagnetism. The exact origin of the magnetic ordering in dilute magnetic semiconductors is still under debate.

Generally, this class of systems is viewed as consisting of two interacting subsystems. The first is the dilute and randomly distributed system of localized magnetic moments associated with the magnetic dopants. The second are the delocalized carriers of the host. The general consensus is that for Mn-doped III-V-ferromagnets, while the magnetic moments are provided by the manganese atoms, indirect exchange interaction involving the free carriers allows them to couple. It is the interaction of these two subsystems which is creating the long range ordering phenomena. The crucial role of the free charge carriers became more and more obvious over time. It was conclusively demonstrated by investigating the dependence of the Curie temperature on the carrier concentration[48]. The fact that the presence of free charge carriers mediates the ferromagnetic order creates the novel oppurtunity to modulate or switch the ferromagnetism on and off by applying a bias voltage[90]. Figure 2.1 shows the experimental T_C versus the hole density (left) and its dependence on a gate voltage (right). Both show how the magnetic stability depends strongly on the carrier concentration and how the ferromagnetism is suppressed when the free carriers are removed.

But there is no single universal theory of ferromagnetic ordering, and understanding magnetic order for a given system often remains a challenge. A number of more or less phenomenological theories have been developed over the last decades to describe magnetic ordering phenomena in different systems. Which of these theories are appropriate to describe magnetic order in specific dilute

(a)

(b)
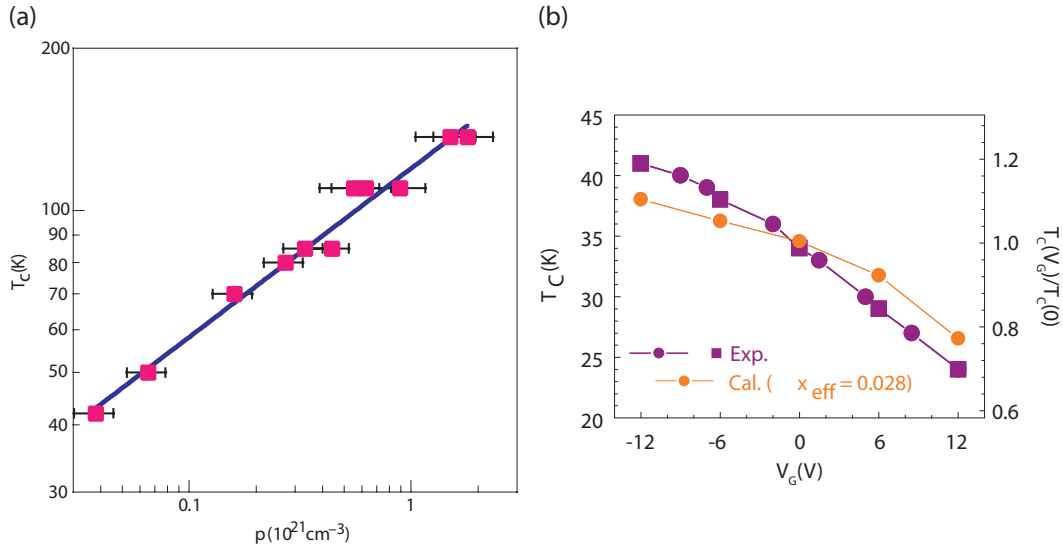
Figure 2.1: **Charge carriers mediate the ferromagnetic order in dilute magnetic semiconductors. (a):** Experimental T_C vs. carrier density (from [59; 65]). **(b):** Modulation of the Curie temperature with gate voltage (from [90]).

magnetic semiconductors remains a topic of debate.

For localized spins in close proximity there is HEISENBERG's *direct exchange*[6], basically describing the energy difference between symmetric and antisymmetric wave functions of two spins. As mentioned earlier, direct exchange between the localized manganese moments is not the dominating interaction in dilute magnetic semiconductors. The dilute nature of the magnetic moments leads to fairly large average Mn-Mn distances (about 2 nm at 1 % Mn concentration) and little wave function overlap. The role of direct exchange is therefore very limited in DMS, and some form of indirect interaction via other states has to provide the coupling. I will briefly describe the most important mechanisms in the following. Figure 2.2 shows schematic depictions of all the mentioned exchange mechanisms.

KRAMER's *super-exchange*[3] describes the interaction of two localized spins with a nonmagnetic atom in between. In this mechanism, an electron is transferred from the middle atom to an empty shell of the magnetic atom, and couples via direct exchange to the electrons of its environment. The middle atom is polarized and is coupled to its magnetic neighbors. Depending on the relative sign of the involved exchange interactions, the resulting super-exchange can be ferromagnetic or anti-ferromagnetic[38; 49]. Since the mediating state is a bound state and the crucial effect of carrier density has already been demonstrated in the III-V materials, this mechanism can be ruled out as the major source of ferromagnetic order.

The *double exchange* mechanism proposed by ZENER[120] also assumes an intermediate nonmagnetic atom. But instead of the transfer of an electron from a magnetic atom to the nonmagnetic one, carrier hopping of magnetic-shell electrons happens between the magnetic atoms through the intermediate nonmag-
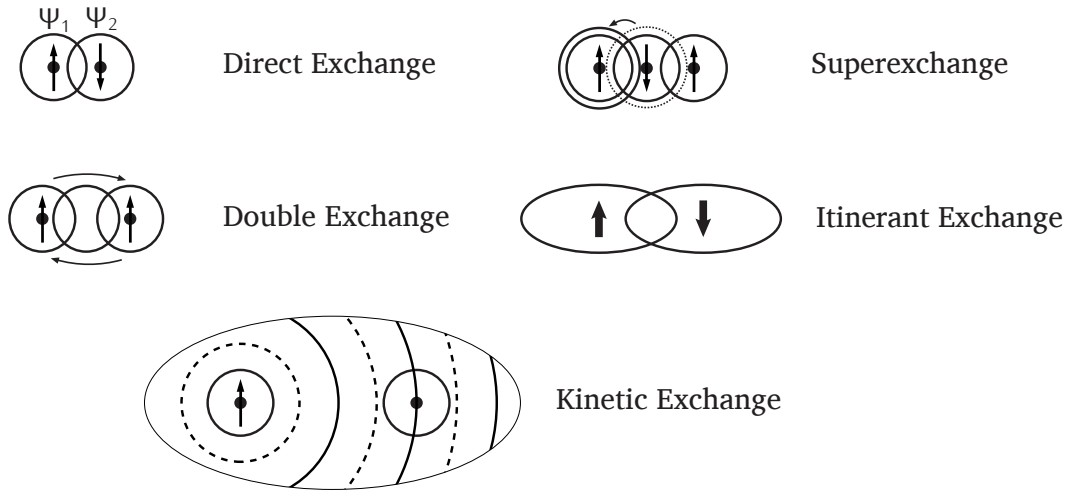
Figure 2.2: Direct and mediated exchange mechanisms. Due to the dilute nature of the manganese-spins, direct coupling via host states is not sufficient to create long range magnetic order. It has been shown to originate from other, indirect interaction mechanisms via states of the host material.

netic atom. This interaction favors parallel spin alignment, i.e. is ferromagnetic. In a picture often used in (III,Mn)V literature, the Mn acceptor states form an impurity band with mixed spd character and exchange coupling as well as electrical conduction are both realized through hopping within the impurity band[47].

STONER's *itinerant exchange*[6] applies to delocalized spins in systems with large density of states at the Fermi energy. In this case, the system can easily lower its total energy by shifting electrons from one spin band to the other with little impact on kinetic energy. According to JUNGWIRTH *et al.* [47], it does play a minor supporting role in DMS but since the manganese spins are localized, it does not drive ferromagnetism in these materials.

ZENER also described *kinetic exchange*[121], sometimes called *indirect exchange*. Here, local moments, usually in d- or f-shells, interact via itinerant carriers in s- or p-bands. Band electrons are polarized through interaction at one site, and this polarization propagates to neighboring sites. The interaction can be of long range. This effect is in principle covered by Ruderman-Kittel-Kasuya-Yoshida theory[51; 87; 119] (RKKY), as long as the coupling and thus the polarization of the band carriers is weak, e.g. at temperatures close to the Curie temperature. Consequently, the interaction oscillates in space on the length scale of the Fermi wavelength of the itinerant carriers. This effect is likely to dominate in the case of strongly metallic (Ga,Mn)As, (In,Mn)As and Mn-doped antimonides[47]. Double exchange can also be regarded as a special case of kinetic exchange, in the limit of strong coupling and a narrow carrier band.

More recently, a study devoted to the onset of ferromagnetism in (Ga,Mn)As[93] successfully predicted the Curie temperature for low-doping densities in good accordance with magnetization, resistivity and Hall effect measurements on low-doped samples ($p = 1 \times 10^{17}$ cm^{-3} to 1×10^{19} cm^{-3}). The results

support that in this doping range *Mott-regime variable range hopping*[4; 75; 104], a mechanism similar in nature to the mentioned double-exchange, is in fact the dominating effect and that the hopping energy primarily determines the Curie temperature T_c which mean field theories have been unable to properly describe.

Charge carriers (holes) undoubtedly mediate the ferromagnetic order in p-type (Ga,Mn)As as well as (In,Mn)As. There is however a notable difference between the two systems as demonstrated in a photoemission spectroscopy study (RPES and ARPES[†])[80]. In p-type (Ga,Mn)As the impurity states form an impurity band which is split off significantly from the valence band maximum. This means that these states are more strongly localized and can be best understood as bound holes rather than free carriers, which is argued to contribute to the higher T_c found in (Ga,Mn)As as compared to (In,Mn)As. The study could not verify the existence of such impurity-band-like states for (In,Mn)As, which is attributed to weaker hybridization between the host valence band and Mn $3d$-states in InAs, leaving the holes less strongly bound and more free-carrier-like. This difference has to be kept in mind when looking for theoretical models for the ferromagnetic order in InAs and comparing to (Ga,Mn)As.

In addition to the interplay with delocalized carriers and mechanisms of long-range interaction, the *local structure* of the hole wave function is of great importance. Since the hole governs the coupling of the local magnetic moment to long range interactions, its properties influence the overall interaction crucially. Significant anisotropies of the interaction between individual dopants as well as anisotropies in the long-range order can arise from asymmetries of the hole wave function. A beautiful demonstration of the importance of the local wave function was provided by KITCHEN *et al.* [54; 55]. In this experiment, manganese atoms were manipulated into the surface layer of GaAs with the STM. By systematically creating pairs of manganese atoms in different configurations, a strong direction dependence of the interaction energy could be demonstrated.

Obviously, a local, atomic-scale investigation is essential to figure out the local shape and extension of the hole wave function, as it crucially influences the magnetic interaction. Therefore, one goal of this study is to identify the exact local shape of the bound hole wave function of Mn in InAs, as an indication for anisotropies of the magnetic interaction.

2.2 STM studies of dopants in semiconductors

Atomic defects and single dopants in (110) surfaces of III-V semiconductors have been studied with STM a number of times over the years. FEENSTRA for example in 1993 described a number of different defects in the GaAs (110) surface[33]. The strongly non-spherical appearance of such defects is already apparent here. A number of studies early on focused on the appearance and the spectroscopic signature of single dopants in semiconductors. For example, DEPUYDT *et al.* studied Te in GaAs(110)[23] and described conductance peaks within the band gap.

[†]Resonant PhotoEmission Spectroscopy / Angle Resolved PhotoEmission Spectroscopy

Dopant/Host	E_acc/E^H	$\begin{smallmatrix}[0\bar{1}0]\\ \uparrow\\ \rightarrow [001]\end{smallmatrix}$	Shape	References
Te/GaAs	6.44	▶◀	symmetric bow-tie	[24],[15]
Mn/GaAs	4.40	▶◀	symmetric bow-tie	[16],[45],[118]
Cd/GaP	1.35	▶◀	asymmetric bow-tie	[16]
Mn/InAs	1.70	▶◀	asymmetric bow-tie	[5],[62]
Cd/GaAs	1.36	▶◀	asymmetric bow-tie	[16],[58]
Zn/InP	1.13	◀	triangle	[58]
Zn/GaAs	1.19	◀	triangle	[58],[63],[67]
Be/GaAs	1.09	◀	triangle	[67]
C/GaAs	1.05	◀	triangle	[63]

Table 2.1: Overview of different dopant/host systems. For each dopant/host combination the table gives the ratio of acceptor energy to hydrogenic binding energy (see Section 2.4), the basic appearance and references to the according STM studies.

Zn and Cd in GaAs(110) and InP(110) were studied by DE KORT *et al.* [58]. They described circular features for filled state images of both dopants in both materials but triangular shapes pointing in [001] direction for energies at the bottom of the conduction band.

A first systematic overview of the STM appearance of single Mn dopants in InAs(110) over a wide energy range was published by ARSEEV *et al.* [5]. The authors conclude that they directly observe *d*-orbitals of the dopant and explain the spectroscopic appearance with a complex theory of non-equilibrium charging effects and many-particle interactions. In 2004, YAKUNIN *et al.* presented a detailed study of the anisotropic topographic appearance of Mn dopants in GaAs(110) alongside with results from tight-binding calculations, and also explicitly distinguished two charge states. The Mn acceptor feature at positive bias was found to appear bow tie shaped, which was reproduced by the tight-binding model and interpreted as the direct image of the hole bound to the manganese acceptor. However, other studies found Zn and Be[67] and C dopants[63] in the same surface to appear as triangles. In another study already mentioned before, manganese atoms were manipulated into the surface[54]. This way, the exchange energies of pairs of Mn atoms depending on relative position could be studied and the pronounced anisotropy was demonstrated. The observed empty-state shapes range from symmetric bow-tie shapes to rather asymmetric ones where one side is stronger than the other to those where one side is practically not visible and the shape resembles a triangle. Table 2.1 shows experimentally observed shapes of several combinations of dopants and host materials.

Combinations where the dopants appear as symmetric bow-ties are tellurium and manganese in gallium arsenide, while e.g. manganese in indium arsenide has an asymmetric appearance. Beryllium and carbon are examples of dopants which appear triangular in gallium arsenide.

The varying empty-state appearances of different dopants started to gain attention and several publications focused on these differences and their origin. After JANCU and VOISIN investigated the role of crystallographic strain and were able to demonstrate its importance[46], YAKUNIN et al. were able to experimentally demonstrate the effect of strain on the appearance of the Mn state using cross-sectional scanning tunneling microscopy[117]. By growing InAs quantum dots in a Mn-doped GaAs host, they created areas with a predictable local strain with manganese dopants embedded. This way they were able to demonstrate how strain in, for example, [111]-direction leads to a distorted wave function (extended along $[\bar{1}11]$ and contracted along $[1\bar{1}2]$). ÇELEBI et al. looked into the origin of the anisotropic shape of the wave function and also investigated the role of spin-orbit interaction by comparing STM data to tight-binding and effective-mass theoretical models[16]. They conclude that spin-orbit interaction only slightly modifies the bound-hole wave function which is otherwise determined by the cubic symmetry of the host. In a recent study JANCU et al. focused especially on the surface related strain and its effect on STM images. They conclude that while the bulk hole wave function of acceptors in III-V semiconductors appears rather symmetric with regard to the (001) mirror plane, the impurity state is split due to the buckling at the (110) surface and that this strain plus hybridization with surface states leads to a strong (001)-asymmetry of the shape observed for manganese in gallium arsenide and cadmium in gallium phosphide[45], just as described above.

Such modifications of the hole wave function caused by the surface or other effects are likely to affect magnetic properties of the system. If strain-induced warping of the wave function produces for example direction dependence of the magnetic interaction, special properties like modified Curie temperature or magnetocrystalline anisotropy might arise. Such effects are especially relevant at interfaces, in thin films and other nanostructures, where strain and reconstruction usually occur. Therefore it will be informative to study surface-related or other modifications of the wave function in our sample system with the STM, as will be done in Chapter 4 and Chapter 6.

2.3 Crystal structure and electronic properties of InAs

InAs belongs to the group of III-V semiconductors, where an element from group-III (B, Al, Ga, In) and a group-V element (N, P, As, Sb) are combined in equal parts. The constituents provide a total of 8 electrons in s- and p-shells, which leads to the formation of four sp-hybrid bonds per atom (see Figure 2.5). In the case of
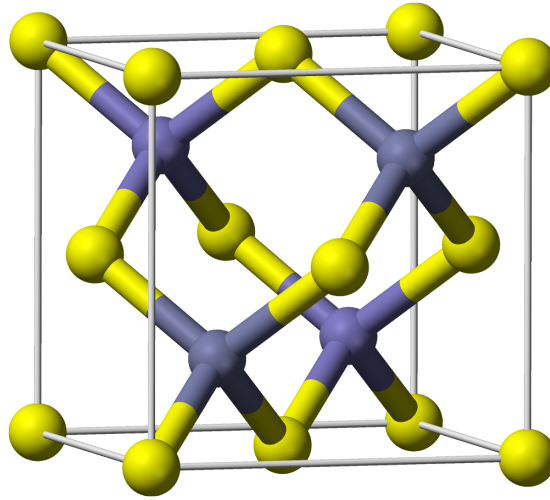
Figure 2.3: **Zinc-blende structure of indium arsenide.** Yellow: indium, Grey: arsenic. Every atom has four sp-hybrid bonds to its neighbors in tetrahedral arrangement. The lattice constant is $a_0 = 0.606\,\mathrm{nm}$.

InAs, indium provides three electrons with a configuration of $[\mathrm{Kr}]\ 4\mathrm{d}^{10}\ 5\mathrm{s}^2\ 5\mathrm{p}^1$ while arsenic provides five electrons and has the configuration $[\mathrm{Ar}]\ 3\mathrm{d}^{10}\ 4\mathrm{s}^2\ 4\mathrm{p}^3$. The sp-hybrid bands split up into a filled and an empty band, leaving a band gap of $E_{\mathrm{gap}} = 415\,\mathrm{meV}$.

The arrangement of the tetrahedral bonds leads to a typical zinc-blende structure, shown in Figure 2.3. This structure can be described as consisting of an fcc-lattice of one element combined with an fcc-lattice of the other element, offset by one quarter of the fcc body diagonal. This leads to every atom having four equally spaced neighbors in tetrahedral arrangement.

The schematic band structure of InAs is shown in Figure 2.4. InAs has a direct band gap at $\vec{k} = 0$ (the Γ-point) of $E_{\mathrm{gap}} = 0.35\,\mathrm{eV}$ at $300\,\mathrm{K}$ ($0.415\,\mathrm{eV}$ at $0\,\mathrm{K}$). Another important parameter of the electron system in a semiconductor is the effective mass m^*, the inverse of the band curvature in k-space, which usually equals a fraction of the electron rest mass m_0. At the Γ-point, electrons in InAs have an effective mass of $m_n^* = 0.023 m_0$. Due to the band structure of InAs, there are three different types of holes. Right at the lower edge of the gap there are heavy holes ($m_{hh}^* = 0.41 m_0$) and light holes ($m_{lh}^* = 0.026 m_0$). Additionally, there is a band of split-off holes with $m_{so}^* = 0.16 m_0$. The g-factor in InAs which determines the magnitude of the magnetic moment μ_S in relation to the spin S, is $g_S = -15.3$. The dielectric constant is $\epsilon_r = 15.15$. All these main material parameters are gathered in Table 2.2.
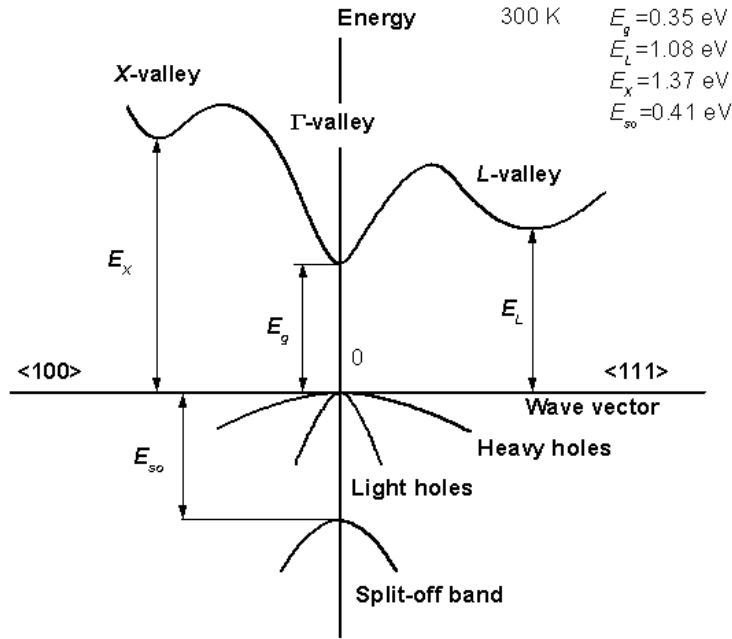
Figure 2.4: Band structure of indium arsenide. InAs has a direct band gap at the Γ-Point ($\vec{k} = 0$). Three types of holes exist at the Γ-point: heavy holes, light holes and a split-off band at lower energies. (Source: Ioffe Physical Technical Institute[1])

Lattice constant	a_0	0.606 nm
Energy gap at room temperature	$E_{\text{gap,RT}}$	0.35 eV
Energy gap at 0 K	$E_{\text{gap,0}}$	0.41 eV
Effective electron mass	m_n^*	$0.023 m_0$
Effective heavy hole mass	m_{hh}^*	$0.41 m_0$
Effective light hole mass	m_{lh}^*	$0.026 m_0$
Effective split-off hole mass	m_{so}^*	$0.16 m_0$
g-factor	g_S	-15.3
Dielectric constant	ϵ_r	15.15
Electron affinity	E_A	4.9 eV

Table 2.2: Material parameters of InAs. (From [66]).

2.4   Dopants in semiconductors

Dopants are foreign atoms incorporated into a semiconductor which contribute charge carriers. Usually, dopants take the lattice position of a regular constituent (substitutional). They provide charge carriers to the material, depending on their concentration and electronic configuration. If the dopant adds electrons to the

material, it is called a *donor*. Typical donors in III-V compounds include magnesium, carbon, selenium, manganese, tellurium, silicon and germanium. Since a donor has an increased nuclear charge, it is able to bind the extra electron, forming a neutral ground state. If ionized, the donated electron occupies states in the conduction band and therefore the ground state is usually referenced to the conduction band minimum and thus lying in the band gap. *Acceptors* on the other hand are dopants that remove electrons from the environment to satisfy their chemical bonds. Common elements used as acceptors include beryllium, zinc, cadmium, silicon and germanium. Some elements like silicon and germanium can act as both donors and acceptors, depending on the host material and concentration. The lack of electrons in an acceptor can still be seen as providing a charge carrier to the material, this time in the form of a "missing" electron, called *hole*. In many aspects, it is valid to treat a hole in the same way as an electron but with an inverted charge, energy scale and a different effective mass. Analogous to dopants, the neutral ground state of an acceptor is referenced to the valence band maximum, since their "free carrier continuum" is the valence band.

A dopant in a semiconductor is sometimes classified as *shallow* or *deep*. This quality relates the dopant's binding energy to the "hydrogenic" binding energy, which is a simple and straightforward way of estimating the binding energy of impurities. "Hydrogenic" makes reference to the basic quantum mechanical problem of the hydrogen atom. Analogous to the binding of an electron to a charged core in vacuum, one now simply substitutes the electron's (hole's) effective mass for the real electron mass and the appropriate dielectric constant for ϵ_0. Any interaction of the free charge with other states is neglected.

The basic formulas for the hydrogenic energy terms and the Bohr radius are:

$$E_n^{\text{H}} = -\frac{e^4 m}{2 \left(4\pi\epsilon_r\epsilon_0\hbar\right)^2} \frac{1}{n^2} \tag{2.1}$$

$$a_1 = \frac{4\pi\epsilon_r\epsilon_0\hbar^2}{e^2 m} \tag{2.2}$$

For $m = m_0$ and $\epsilon_r = 1$ this gives the familiar 13.6 eV and 0.053 nm for the hydrogen ground state ($n = 1$). In the case of a semiconductor, we have to use the effective mass m^* and the dielectric constant ϵ_r. This means that the hydrogen-like binding energies for dopants are usually much smaller than the binding energy of free hydrogen, and their radii are much larger. For the acceptor in InAs we use m_{hh}^* (the effective mass of a hole at the top of the valence band, about one half of m_0) and $\epsilon_{r,\text{InAs}} = 15.15$, which yields $E_{\text{InAs}}^{\text{H}} \approx 24$ meV and $a_1^{\text{InAs}} \approx 2$ nm. There is a more advanced form of this model where the electron's Hamiltonian is separated into a spherical part and a cubic correction and the cubic part is solved perturbatively using the eigenstates of the spherical hamiltonian. The model is described in reference [7] and this is also where the hydrogenic energy terms in Table 2.3 below were taken from. Note that the hydrogenic binding energy is not impurity specific. It is determined only by properties of the host material.

| | E_{gap} @4 K (eV) | E_{H} (meV) | E_{acc} (meV) | | | |
			Mn	Zn	C	Si
InAs	0.42	16.6[a]	28.0[b]	—	—	20.0[c]
GaAs	1.42	25.6[a]	113.1[c]	30.5[c]	26.9[c]	34.5[c]
InSb	0.17	8.6[a]	7.0[d]	9.9[c]	—	—

[a]A. Baldereschi and Nunzio O. Lipari. Spherical model of shallow acceptor states in semiconductors. *Phys. Rev. B*, 8(6):2697–2709, 1973 [7]

[b]E. I. Georgitse, I. T. Postolaki, V. A. Smirnov, and P. G. Untila. Photoluminescence of p-type InAs:Mn. *Soviet Physics–Semiconductors*, 23:469–70, 1989.[36]

[c]Otfried Madelung. *Semiconductors: Data Handbook*. Springer-Verlag, 2004.[66]

[d]A. B. Henriques, N. F. Oliveira Jr., S. A. Obukhov and V. A. Sanina. Giant negative magnetoresistance in a nonmagnetic semiconductor. *JETP Letters*, 69:358–-362, 1999[43]

Table 2.3: Dopant energies and band gap. Band gap and hydrogenic (see text) ground state energies for InAs, GaAs and InSb, as well as experimental values for different dopants.

The dopant energies found in experiments deviate more or less from these hydrogenic energies. The following table gives an overview of different semiconductors with their hydrogenic acceptor energies and some actual acceptor energies found in the literature.

A dopant with a binding energy considerably higher than the hydrogenic one is considered a deep donor (acceptor). Those close to the hydrogenic energy are said to be shallow. The second column of Table 2.1 gives the ratio of the acceptor binding energy to the hydrogenic binding energy. Mn in GaAs, for example, is a deep acceptor, while C in GaAs is a shallow acceptor. Mn in InAs can be considered an intermediate case, neither really a deep acceptor nor actually a shallow one. As can be seen from Table 2.1, an acceptor's tendency to appear symmetric seems to be related to its "deepness", at least to some degree.

2.4.1 Mn in InAs

Manganese can potentially form different electronic configurations, depending on the doping concentration and its position in the host lattice. Under less than optimal growth conditions, other defects like interstitials, atoms between regular atomic sites of the lattice, can occur. Interstitial manganese acts as a double donor which compensates carriers provided by acceptors, effectively reducing the carrier density. More importantly, they have been shown to also compensate the magnetic moments of the substitutional dopants[28; 104]. They do so by coupling anti-ferromagnetically to neighboring substitutional Mn sites which can suppress ferromagnetism[106; 115]. Therefore, growth processes are optimized

to suppress interstitial formation. In low-doped and in high-quality ferromagnetic samples, the vast majority of dopants are incorporated substitutionally into In sites and therefore we will focus on that.

The outer electronic configuration of manganese ([Ar] $3d^5 4s^2$, see Figure 2.5) is similar to that of indium ([Kr] $4d^{10} 5s^2 5p^1$), however, while indium has one electron in its outer $5p$ shell, manganese misses this electron in its $4p$ shell. When a manganese atom substitutes for an indium atom, its $4s$-electrons take part in an sp-hybrid bond very much like indium itself. To fill in for the missing electron, Mn binds an additional electron and thus acts as an acceptor. The type of missing electron (p or d) mainly governs the nature of the created hole state, but interaction/hybridization between p- and d-states can further modify the state.

The simplest case is the negatively charged acceptor, called $A^-(Mn^{2+}3d^5)$. Here all states, the sp-hybrid states as well as all five d-states, are occupied. For the neutral A^0 state, things are more complicated and different models of the hole state exist. Since the manganese atom is incorporated in a crystal with tetrahedral bonds, it is embedded in a crystal field with tetrahedral symmetry. This causes the otherwise five-fold degenerate $3d$-states to split into a pair of states with E-symmetry and a triplet with T_2-symmetry[91]. This splitting between $3d(E)$-states and $3d(T_2)$-states can be large enough to lift the $3d(T_2)$-states above the sp^4-hybrid states. Since a hole will occupy the highest available state (i.e. the state with the highest energy will be depopulated first), the hole would be a $3d(T_2)$-state. If the splitting is smaller, the hole has $4p$-character and the electrons are distributed in the five d-orbitals to satisfy Hund's rule and maximize the net orbital spin. These two variants are depicted in Figure 2.5 as *model 1* (hole in $4p$-state) and *model 2* (hole in $3d$-state). The nature of the hole state strongly influences the magnetic properties of the material.

In model 1 the d-orbitals of the Mn are not strongly affected by the crystal field and stay localized and well below the valence band maximum. If the negative charge weakly binds a valence band hole, a $A^0(Mn^{2+}3d^5 + hole)$-complex is created. In this case, the p-type hole ground state has a hydrogen-like, rather delocalized orbit, while the $3d$-states remain the same as in a free atom.

If model 2 applies, the neutral state is created by having the hole in a much more strongly localized d-state, creating the configuration $A^0(Mn^{2+}3d^4)$. There is no final answer on whether the neutral state conforms to model 1 or model 2. First-principles calculations suggest that the carriers have d-character[2], while electron-spin resonance measurements on Mn acceptors in GaAs[97] and InAs[96] find a $3d^5 + hole$ configuration. In an STM study of manganese acceptors in GaAs[118], YAKUNIN *et al.* come to the same conclusion, based mainly on the large extension of the wave function.

Multiband tight-binding calculations were performed for Mn in GaAs and in InAs for the case of model 1, $A^0(Mn^{2+}3d^5 + hole)$[69; 100]. They revealed that spin-orbit interaction will also induce a splitting of the acceptor level of Mn in InAs and GaAs. The acceptor level is split into three spin-states with energy separations of 28 meV and 50 meV for (In,Mn)As[69]. Chapter 6 will look at the experimental detection of these states.
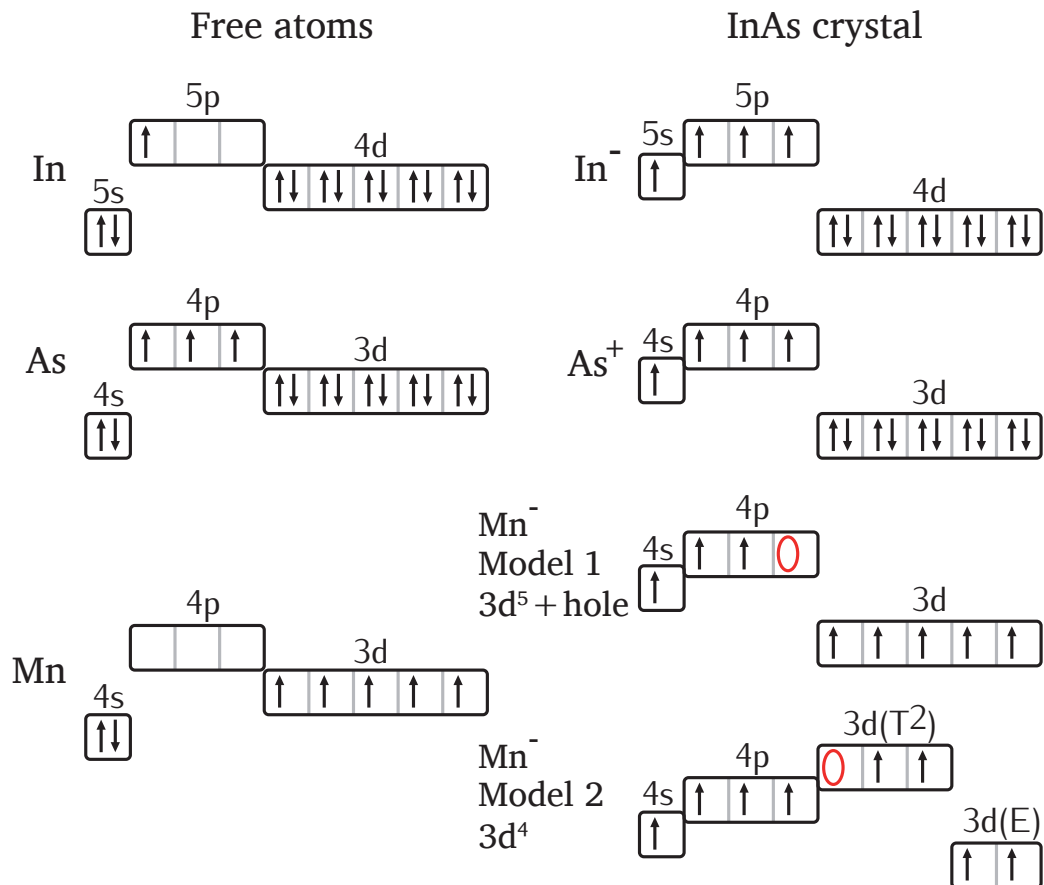
Figure 2.5: Electronic configurations of indium, arsenic and manganese as free atoms and in an (In,Mn)As crystal. Arsenic and either indium or manganese form *sp*-hybrid bonds. Two models exist for the nature of the hole state (red ellipse): Model 1 states that it has *p*-character, while in model 2 the *d*-states are split by the crystal field sufficiently for the hole to enter a *d*-state.

Chapter 3

Scanning tunneling microscopy and spectroscopy

This chapter explains the working principle of the scanning tunneling microscope and describe the facilities used for this study. Vacuum tunneling as the driving mechanism of the STM is introduced and some practical equations for its experimental use are derived from approximations. Tip-induced band-bending, an effect that plays a crucial role when doing STM on semiconductors, is also introduced. The design of the microscopes employed in our measurements is briefly illustrated, as well as the overall design of the UHV systems housing these microscopes.

3.1   Scanning tunneling microscopy

3.1.1   Basic principles of STM

The imaging mechanism of the scanning tunneling microscope is based upon quantum mechanical tunneling. This effect is the quantum mechanical description of the motion of electrons through classically forbidden barriers. They are able to permeate a potential barrier of finite width even though their energy is less than the barrier height. In the classical understanding, particles are reflected at the barrier. In the quantum mechanical description though, due to the dual nature of particles, there is a finite probability for the electron to transcend the barrier, i.e. given by a finite transmission coefficient.

The overall principle of the STM is that a conductive (usually metallic) tip is brought into close enough proximity above a conductive sample that a quantum mechanical tunnel current starts flowing. The current is measured and can be used in a regulation circuit to keep the junction resistance constant, and with it
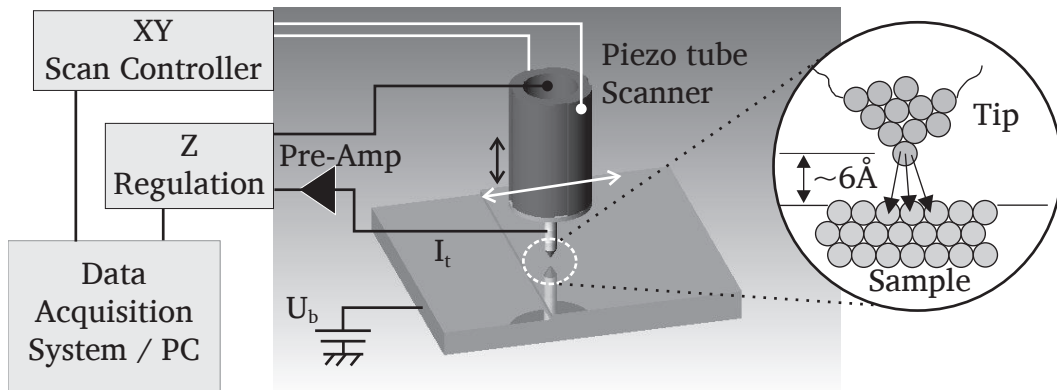
Figure 3.1: Schematic overview of the STM's working principle. The tip is moved across a sample surface by means of a piezo tube. In close proximity, a small current can flow across the vacuum gap between tip and sample. The current is kept constant with a feedback circuit by adjusting the tip height. Data like tip position, current, etc. can be recorded in a measurement. (Source: [107]).

approximately the tip-sample separation. Figure 3.1 gives a schematic overview of this. Several operational modes are possible, but the most frequently used mode is the mentioned constant-current mode, where a feedback circuit keeps the tunnel current equal to a set point by adjusting the tip-sample distance. With this regulation in place the tip is scanned line-by-line across the surface and the vertical displacement of the tip is recorded as a function of the lateral position. This way, a close reproduction of the surface topography is obtained, which is why constant-current images are also called *topographs*.

The vertical as well as the lateral motion of the tip in an STM is provided by piezoelectric motors. Piezoelectric elements which deform in the presence of an electric field are a perfect match for the requirements, since they provide subatomic accuracy with a motion range on the micrometer scale exclusively through deformation, without any "movable" parts in the usual sense. The design implemented in the measurement systems that were used in this study manages to achieve both kinds of displacement, normal and lateral to the sample surface, i.e. full three-dimensional motion, with just a single piece of piezoelectric material in the shape of a tube. This is achieved by a clever scheme of segmenting the electrodes at the surface of the tube, illustrated in Figure 3.2.

Even though the scanning tunneling microscope is a very immediate way of mapping a surface, a qualitative and quantitative interpretation of measurements can be challenging. In order to do so, one must understand the dependence of the tunnel current on the experimental parameters like the applied bias voltage and the tip-sample distance, as well as on the detailed electronic structure of the surface. In the following, we start by looking at the tunneling probability of a single electron.
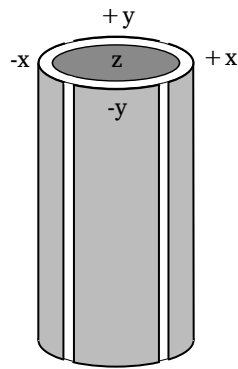
Figure 3.2: Electrode configuration of a piezo tube scanner. A potential difference between the X-electrodes (-X , +X) leads to a bending of the tube in X-direction, and accordingly for the Y-direction. A potential difference between all the outer electrodes and the inner electrode (Z) leads to a contraction or expansion of the tube and thus allows to control the Z-position of the tip.
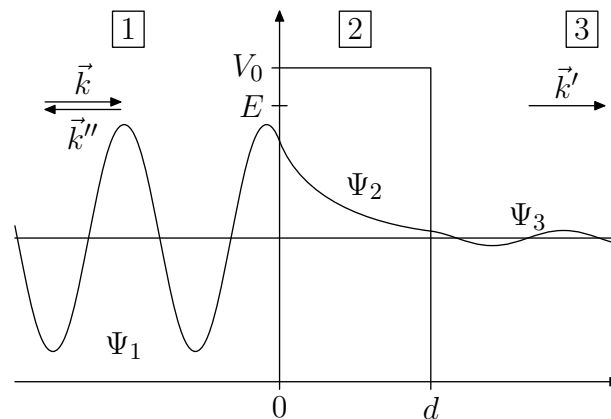
Figure 3.3: One dimensional tunnel effect at a barrier of width d and height V_0. The solution is composed of three partial solutions for a plane wave arriving from the left and being reflected (Ψ_1), a wave function decaying into the barrier and being reflected (Ψ_2) and an outgoing plane wave (Ψ_3). Source: [41]

3.1.2   The tunnel gap

Figure 3.3 gives a one-dimensional model of the vacuum barrier between tip and sample for a plane wave approaching from the left. This case can be solved exactly[50] by assuming a plane wave ψ_1 with incoming (wave vector $\vec{k}$) and reflected outgoing ($\vec{k''}$) component before the barrier, a wave function ψ_2 in the barrier, composed of an exponentially decaying and an exponentially rising part with decay constant κ, and an outgoing plane wave ψ_3 (wave vector $\vec{k'}$) behind it. Furthermore, one regards only elastic tunneling processes, i.e. the energy of incoming and outgoing wave is the same. Since all these components have to

satisfy SCHRÖDINGER's equation, one gets

$$|\vec{k}| = |\vec{k''}| = |\vec{k'}|$$

$$= k = \sqrt{\frac{2mE}{\hbar^2}}$$

and

$$\kappa = \sqrt{\frac{2m(V_0 - E)}{\hbar^2}}$$

where V_0 is the barrier height and m is the particle mass.

With the additional condition that these components connect smoothly at the borders one arrives at an expression for the transmission coefficient (with s: barrier width):

$$T = \frac{1}{1 + (k^2 + \kappa^2)^2/(4k^2\kappa^2)\sinh^2(\kappa d)}$$

T is the probability that an electron impinging on the barrier is transmitted.

Assuming a high and/or wide barrier ($\kappa d \gg 1$) allows the following approximation:

$$T \approx \frac{16k^2\kappa^2}{(k^2 + \kappa^2)^2} e^{-2\kappa d} \tag{3.1}$$

This representation already reveals the exponential dependence of the tunnel current on the distance, which plays an important role for practical matters. In situations typical for STM, $(V_0 - E)$ is usually on the order of several eV. Then, by increasing d by 1 Å, the transmission probability/rate and thus the current will be reduced by a factor of ten. This fact already explains the good vertical resolution of the STM. The high lateral resolution also becomes plausible since the second-lowest atom, if it is e.g. 1 Å higher than the lowest one, only contributes about a tenth of the total current, depending on the value of κ.

3.1.3 Bardeen's perturbation approach

In 1961, long before the invention of the STM, BARDEEN presented an equation for the tunnel current that is not specific to the dimensionality of the problem[8]. In his solution which uses a perturbative approach, he assumed the electronic states of the two electrodes (tip and sample in our case) to be independent of each other. The two systems are decoupled, and there is a potential $U_\mu(\vec{r})$ in the sample and another one $U_\nu(\vec{r})$ belongs to the tip. There is a set of eigenfunctions ψ_μ to energy eigenvalues E_μ in the sample and another set of eigenfunctions χ_ν to eigenvalues E_ν in the tip. He calculated the probability of a transition from a state ψ_μ in one electrode to a state χ_ν in the other electrode. In perturbation theory, the potential belonging to the final state (U_ν in this case) is assumed to be switched off for $t < 0$, and the system is in an eigenstate of the sample: $\Psi(0) = \psi_\mu$. Next, the temporal development of the wave function is considered, if the potential U_ν is switched on at $t = 0$:

$$\Psi(t) = \psi_\mu e^{-i/\hbar E_\mu t} + \sum_v c_v(t) \chi_v e^{-i/\hbar E_v t} \tag{3.2}$$

where $\Psi(t)$ solves the time-dependent Schrödinger equation

$$\left(-\frac{\hbar^2}{2m}\Delta + U_\mu + U_v\right)\Psi = i\hbar\frac{\partial\Psi}{\partial t} \tag{3.3}$$

The square of the absolute value of the expansion coefficients $c_v(t)$ equals the probability of finding the system in state χ_v at time t. Accordingly the rate of transition is equal to the time derivative of $|c_v(t)|^2$.

By applying a bias voltage U, the Fermi levels of tip and sample are shifted against each other by eU, causing a net current to flow.

In order to apply this theory to calculate the total tunnel current from $|M_{\mu v}|^2$, one has to

▶ multiply the expression by the mean occupation $f(E)$ of the initial state and by the probability of the final state being available $(1 - f(E))$, since tunneling happens from an occupied into an unoccupied state

▶ sum $|M_{\mu v}|^2$ over all states on both sides of the barrier with identical energies, since energy is conserved in the elastic tunneling process

▶ subtract the inverse transmission rate, as it cancels out part of the current, and finally

▶ account for the externally applied bias

By considering all possible transitions and using Fermi's Golden Rule one gets the following expression for the current:

$$I = \frac{2\pi}{\hbar}e\sum_{\mu,v}\left\{f(E_v)\left[1-f(E_\mu+eU)\right]-f(E_\mu+eU)\left[1-f(E_v)\right]\right\}|M_{\mu v}|^2\,\delta(E_v-E_\mu-eU) \tag{3.4}$$

Here, $f(E)$ is the temperature dependent Fermi function which gives the occupation levels within tip and sample, and $M_{\mu v}$, sometimes called tunneling matrix element, is the coefficient giving the probability for a transition from a state E_v in the tip to a state E_μ in the sample. The part in curly braces expresses the total net current as the difference between forward (tip-to-sample) and backward current. The Dirac delta function expresses the fact that only elastic tunneling processes are being considered (energy is conserved). The applied bias is accounted for by replacing E_μ with $E_\mu + eU$, which reflects the relative offset between tip and sample energy scales caused by the bias voltage.

For the tunneling matrix element BARDEEN arrived at[8]:

$$M_{\mu v} = -\frac{\hbar^2}{2m}\int_{\text{Interface}}\left(\chi_v^*\vec{\nabla}\psi_\mu - \psi_\mu\vec{\nabla}\chi_v^*\right)\vec{n}_f\,df \tag{3.5}$$
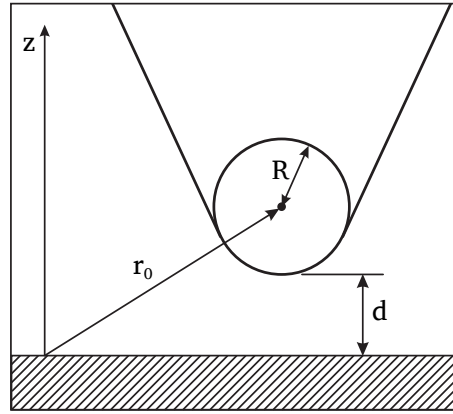
Figure 3.4: Tip and sample geometry in the Tersoff-Hamann model

The integral is evaluated over an arbitrary interface in the space between tip and sample. The vector $\vec{n}$ is the normal vector on this surface.

3.1.4 Tersoff-Hamann model

Building upon this, TERSOFF and HAMANN developed an advanced theory for calculating the tunnel current in scanning tunneling microscopy[102; 103]. This opened the gateway to a solid understanding of the images obtained in STM.

They were able to further simplify BARDEENs expression for the tunneling co-efficient by introducing two assumptions. If one assumes very low temperatures, then $f(E)$ can be approximated by a step function. Under the second assumption that the applied bias potential is small and therefore only states at the Fermi energy need to be considered, one arrives at

$$I = \frac{2\pi e^2 U}{\hbar} \sum_{\mu,\nu} |M_{\mu\nu}|^2 \, \delta(E_\mu - E_{\mathrm{F}}) \delta(E_\nu - E_{\mathrm{F}}) \tag{3.6}$$

In the next step, TERSOFF and HAMANN inserted wave functions on the sample side, which are propagating freely along the surface ($\vec{r}_0^{\parallel}$) but decay exponentially along the surface normal ($\vec{r}_0^{\perp}$):

$$\Psi_\mu = \Omega_s^{-1/2} \sum_{\vec{G}} a_{\vec{G}} \exp\left(-\sqrt{\kappa^2 + \left|\vec{k}_{\parallel} + \vec{G}\right|^2}\,\vec{r}_0^{\perp}\right) \cdot \exp\left(i\left(\vec{k}_{\parallel} + \vec{G}\right) \cdot \vec{r}_0^{\parallel}\right) \tag{3.7}$$

Now, κ denotes the decay constant according to $\kappa = \sqrt{2m\Phi}/\hbar$, and Φ is the sample work function. G is a vector of the reciprocal lattice. The first factor in Eq. 3.7 is for normalization according to the sample volume Ω_s. Furthermore, some assumptions about the geometry were incorporated into the Tersoff-Hamann-model. As illustrated in Figure 3.4, they assumed the tip wave function to be spherical symmetric — essentially s-like — where it faces the sample, and with a radius of R. In the following, d denotes the minimum distance between

tip and sample, and $\vec{r_0}$ points at the center of the tip's curvature. The tip wave function is then:

$$\chi_v = \Omega_t^{-1/2} c_t \frac{\kappa R e^{\kappa R}}{\kappa \left| \vec{r} - \vec{r_0} \right|} \cdot \exp\left(-\kappa \left| \vec{r} - \vec{r_0} \right| \right)$$

Here κ is the same as above, if one assumes equal work functions for tip and sample, and $c_t \approx 1$ is a normalization constant. With these wave functions, one can calculate the coefficient $M_{\mu v}$ according to Eq. 3.5:

$$M_{\mu v} = -\frac{2\pi \hbar^2}{m} \Omega_t^{-1/2} R e^{\kappa R} \sum_\mu \left| \psi_\mu(\vec{r_0}) \right|^2 \delta(E_\mu - E_F) \tag{3.8}$$

Inserting this result into equation 3.6 leads to

$$I = \frac{32 \pi^3 e^2 U \Phi^2 R^2 e^{2\kappa R}}{\hbar \kappa^4} D_t(E_F) \cdot \sum_\mu \left| \psi_\mu(\vec{r_0}) \right|^2 \delta(E_\mu - E_F), \tag{3.9}$$

where $D_t(E_F)$ is the tip's density-of-states per unit volume.

Finally, the sum on the right hand side of the expression is equivalent to the local electron density-of-states (LDOS) of the sample at the location of the tip:

$$\rho_s(\vec{r_0}, E_F) = \sum_\mu \left| \psi_\mu(\vec{r_0}) \right|^2 \delta(E_\mu - E_F) \tag{3.10}$$

Therefore, we can write the simpler expression:

$$I \propto U D_t(E_F) e^{2\kappa R} \rho_s(\vec{r_0}, E_F) \tag{3.11}$$

This demonstrates that contours of constant current measured by the STM are essentially surfaces of constant LDOS of the sample.

Now, the wave function of the sample decays exponentially with distance outside of the sample:

$$\psi_\mu \propto e^{-\kappa z} \qquad \text{with} \qquad z = R + d \tag{3.12}$$

If for simplicity we further assume that the density-of-states in the tip is constant, we arrive at an expression for the tunnel current analogous to Eq. 3.1:

$$I \propto e^{-2\kappa d} \tag{3.13}$$

In summary a number of assumptions and approximations were made to arrive at this equation, which still need to be discussed:

▶ The tip is not necessarily accurately characterized by a single spherical orbital. This will be the topic of the next section.

▶ Interaction between tip states and sample states was not considered. This is however not a problem for the usually large tip-sample distances of ≈ 6 Å.

▶ The electrical field only enters the picture in so far as it determines which states participate in the current. Any influence on tip and sample states or on the potential barrier is ignored. Such effects will be considered in Section 3.2.

▶ Inelastic tunneling processes or many-particle processes were not considered. Due to their low probability their contributions are negligible most of the time, at least for the purposes of this work.

Despite these simplifications the Tersoff-Hamann model successfully reproduced the experimentally observed corrugation of the reconstructed 2×1 and 3×1-Au(110) surface with realistic assumptions for the tip radius (9 Å) and the tip-sample distance (6 Å)[102; 103].

Extension to non-spherical-symmetric orbitals

To overcome the mentioned limitation to s-like sample orbitals as well as the crude approximation of the tip as a macroscopic continuum, CHEN extended the formalism to a microscopic treatment of the tip[17–19]. This was motivated by the fact that large corrugations observed on metal surfaces could not be sufficiently explained, while at the same time mostly metal tips are used where d-states dominate at the Fermi energy [18]. Additionally, it was recognized by DEMUTH that the imaging properties of the STM could vary drastically, even with identical tunneling parameters[22].

CHEN systematically investigated the influence of different types of orbitals on the tunneling matrix element (Figure 3.5) and could obtain the tunneling matrix element for arbitrarily shaped orbitals and was able to explain previously unclear results. He developed the so called *derivative rule* which relates the tunneling matrix element to the local derivative of the wave function[17; 18]:
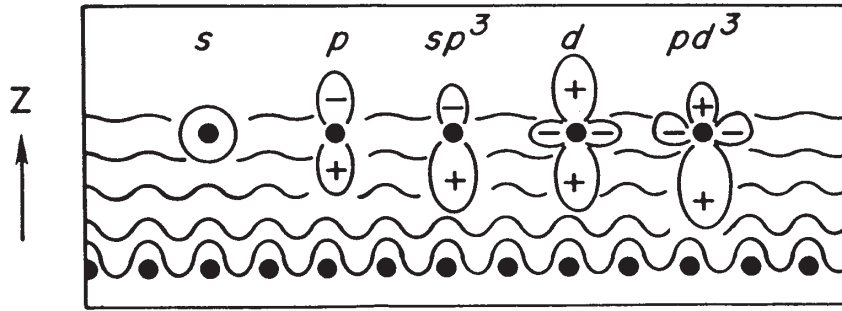
Figure 3.5: Overlap and interaction of different types of orbitals with sample states. (Picture from [110])

Tip state	Matrix element
s	$\frac{2\pi C\hbar^2}{\kappa m}\psi(\vec{r}_0)$
p_z	$\frac{2\pi C\hbar^2}{\kappa m}\frac{\partial\psi}{\partial z}(\vec{r}_0)$
p_x	$\frac{2\pi C\hbar^2}{\kappa m}\frac{\partial\psi}{\partial x}(\vec{r}_0)$
p_y	$\frac{2\pi C\hbar^2}{\kappa m}\frac{\partial\psi}{\partial y}(\vec{r}_0)$
d_{zx}	$\frac{2\pi C\hbar^2}{\kappa m}\frac{\partial^2\psi}{\partial z\partial x}(\vec{r}_0)$
d_{zy}	$\frac{2\pi C\hbar^2}{\kappa m}\frac{\partial^2\psi}{\partial z\partial y}(\vec{r}_0)$
d_{xy}	$\frac{2\pi C\hbar^2}{\kappa m}\frac{\partial^2\psi}{\partial x\partial y}(\vec{r}_0)$
. . .	. . .

Interestingly, his result for an s-like orbital in tip and sample is identical to Tersoff and Hamann's result for a macroscopic tip.

In summary, although it adheres to most of the simplifications made by its predecessors, the extended approach by Chen is able to explain advanced properties of the STM's imaging mechanism.

3.1.5 Scanning tunneling spectroscopy and local density of states

The appearance of the samples' LDOS in constant-current (topographic) mode has already been noted (Eq. 3.9). In addition to that, the STM provides ways to "spectroscopically" measure properties of a sample down to the atomic scale, in contrast to many other spectroscopic methods, which inherently average over several mm^2 or ideally μm^2.

In order to derive the necessary equations from the Tersoff-Hamann model we start by looking at the bias dependency of the tunnel current. Here, we see that the approximation of small bias voltages which led to the basically ohmic behavior, i.e. current proportional to U (Eq. 3.9), no longer holds true[17; 92]. Instead, we resort to a generalization of Eq. 3.9:

$$I \propto \int_0^{eU} \rho_t(\epsilon - eU)\rho_s(\epsilon, \vec{r_0})\mathrm{d}\epsilon$$

Starting with this equation, we reference all energies to the Fermi energy, i.e. $E_F = 0$.

The next step is the so called WKB[*] approximation[110]:

$$\rho_s(E, \vec{r_0}) \propto \rho_s(E, x, y) \cdot \exp\left(-2z\left[\frac{2m}{\hbar^2}\left(\frac{\Phi_t + \Phi_s}{2} + \frac{eU}{2} - \left(E - \frac{\hbar^2 \vec{k}_{\parallel}^2}{2m_e}\right)\right)\right]^{1/2}\right)$$

Here, x and y denote the position of the tip's base point on the sample surface, $z = R + d$ is the distance between tip center and sample surface.

This leads to the following expression for the tunnel current:

$$I \propto \int_0^{eU} \rho_t(\epsilon - eU)\rho_s(\epsilon, x, y)T(\epsilon, eU, z)\mathrm{d}\epsilon \qquad (3.14)$$

with the transmission coefficient T which depends on the energy, the bias voltage and the distance $z = R + d$ between tip center and sample surface:

$$T(E, eU, z) = \exp\left(-2z\left[\frac{2m}{\hbar^2}\left(\frac{\Phi_t + \Phi_s}{2} + \frac{eU}{2} - \left(E - \frac{\hbar^2 \vec{k}_{\parallel}^2}{2m_e}\right)\right)\right]^{1/2}\right) \qquad (3.15)$$

$$= \exp(-2z\kappa)$$

The applied bias determines the direction of the current, into empty states of the sample or out of its occupied states. For any given energy E, κ increases with $\vec{k}_{\parallel}$, which favors states with small $\vec{k}_{\parallel}$ or $\vec{k}_{\parallel} = 0$, i.e. wave vectors perpendicular to the surface. This way, T effectively favors states close to the Γ point.

The most important result here is that by varying the applied bias, the states contributing to the tunnel current can be selected. By this principle, one can probe the local electronic density-of-states experimentally.

From Eq. 3.14 we can derive a particularly useful expression:

$$\frac{\mathrm{d}I}{\mathrm{d}U}(U, x, y) \propto \rho_s(eU, x, y) \cdot T(eU, eU, z) \cdot \rho_s(E_F)$$

$$+ \int_0^{eU} \rho_t(\epsilon - eU)\rho_s(\epsilon, x, y)\frac{\mathrm{d}}{\mathrm{d}U}T(\epsilon, eU, z)\mathrm{d}\epsilon \qquad (3.16)$$

$$+ \int_0^{eU} \left[\frac{\mathrm{d}}{\mathrm{d}U}\rho_t(\epsilon - eU)\right]\rho_s(\epsilon, x, y)T(\epsilon, eU, z)\mathrm{d}\epsilon$$

---

[*]WENZEL, KRAMERS and BRILLOUIN

If we assume a constant (or sufficiently structureless) tip density-of-states and a bias voltage that is small in comparison to the work function:

$$\rho_t \approx \text{const.} \quad \Longleftrightarrow \quad \frac{d}{dU}\rho_t(\epsilon - eU) \approx 0$$

$$\frac{d}{dU}T(\epsilon, eU, z) \approx 0$$

we can simplify this to:

$$\frac{dI}{dU}(U, x, y) \propto \rho_s(eU, x, y) \cdot T(eU, eU, z)$$

This tells us that we can obtain the approximate local density-of-states of the sample by measuring the differential conductance.

The expression for the differential conductance still contains the transmission coefficient which also is energy and bias dependent. To illustrate this, Figure 3.6 shows a schematic energy diagram of the tunnel gap. An important result worth pointing out is that the transmission coefficient depends on the energetic difference to the Fermi energy. Electrons at the Fermi energy of the source electrode experience a lower effective barrier than those which lie at lower energies. In Figure 3.6, this is indicated by the arrows of different length. The states close to the Fermi energy will therefore contribute stronger to the tunnel current.

Note that, as pointed out in 3.1.4, the restriction to s-like tip states used in this derivation is debatable. CHEN has shown that tip states of higher orbital momentum lead to a replacement of ρ_s in Eq. 3.14 and 3.16 by its spatial derivative. Since tunneling into higher orbital tip states requires a strong orientation of the state towards the surface, that is along z, measurements usually will detect a derivative of ρ_s along z. At large enough z, the dependence of ρ_s on the tip-sample separation is mostly described by $e^{-\kappa z}$, and thus the derivative rule only leads to an additional constant in Eq. 3.14 and 3.16, as long as κ is largely independent of x, y, i.e. does not strongly vary laterally.

3.1.6   Normalization of the differential conductance

The influence of the transmission coefficient on the current increases with the applied voltage by mixing in a monotonically increasing background into the obtained spectra, which could obscure peaks coming from states in the sample.

How exactly the transmission coefficient influences spectroscopic measurements has been investigated by, among others, FEENSTRA *et al.* [31]. They suggest a method to normalize dI/dU curves using the total conductance I/U. This cancels out the exponential dependency of the transmission coefficient on the applied bias:

$$\frac{dI/dU}{I/U} = \frac{d(\ln I)}{d(\ln U)}$$
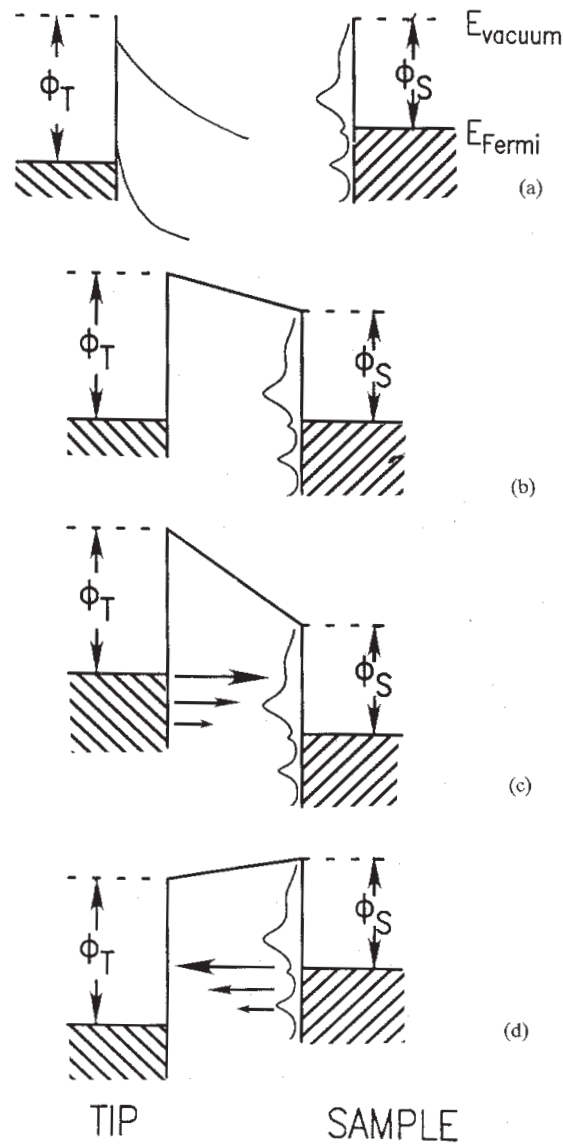
Figure 3.6: Energy scales of tip and sample and bias dependent tunneling. a) At sufficient separation, the work functions of tip and sample determine the relative position of the respective Fermi energies, which are therefore not aligned. **b)** If the tip-sample separation allows electron tunneling (or tip and sample are shorted via their back contacts), their Fermi levels align. **c)** At positive sample bias, electrons tunnel from the tip into the sample. **d)** If negative sample bias is applied, electrons tunnel from the sample into the tip. The differently sized arrows indicate the decaying tunnel probability due to the effective barrier height. (Source: [39])

This can be better understood starting from Equation 3.14 and assuming a constant tip density of states:

$$\frac{\mathrm{d}I}{\mathrm{d}U}(U,x,y) \propto \rho_\mathrm{s}(eU,x,y) \cdot T(eU,eU,z) + \int_0^{eU} \rho_\mathrm{s}(\epsilon,x,y)\frac{\mathrm{d}T(\epsilon,eU,z)}{\mathrm{d}U} \; \mathrm{d}\epsilon$$

This leads to

$$\frac{\mathrm{d}I/\mathrm{d}U}{I/U} = \frac{\rho_\mathrm{s}(eU,x,y) + \int_0^{eU}\rho_\mathrm{s}(\epsilon,x,y)\frac{\frac{\mathrm{d}}{\mathrm{d}(eU)}T(\epsilon,eU,z)}{T(eU,eU,z)}\mathrm{d}\epsilon}{\frac{1}{eU}\int_0^{eU}\rho_\mathrm{s}(\epsilon,x,y)\frac{T(\epsilon,eU,z)}{T(eU,eU,z)}\mathrm{d}\epsilon}$$

The first term in the numerator is the local density-of-states of the sample, while the second term captures the background growing continuously with the voltage. Although the two integral terms in numerator and denominator are different, they only differ by the interior derivative of $T(E,eU,z)$. FEENSTRA *et al.* argue that the exponential dependency on distance and voltage in numerator and denominator effectively cancel each other out. The method has been demonstrated to enhance LDOS features in experimentally obtained $\mathrm{d}I/\mathrm{d}U$ curves[95].

3.1.7 Measurement Modes

In the following I will describe the different methods of conducting measurements in the STM setup which have been used in the course of this work or are otherwise of interest.

Constant current mode

The prevailing mode of STM measurements is the so called *constant-current mode.* There, the tunnel current is kept constant with a feedback loop by making use of the exponential dependence of the current on the tip-sample distance (Eqs. 3.1,3.13). The feedback loop approaches the tip to the surface when the current is below the setpoint and retracts it whenever it is higher than that. With this regulation in place the tip laterally scans an area of the sample surface in a line-by-line fashion. As long as the surface density of states remains homogeneous, a map of the samples' local topography is obtained by recording the current z-position of the tip for every point of the scan area. Figure 3.7(a) illustrates this. Whenever the tip approaches surface features like for example a step edge, the current is affected according to the exponential distance dependence and the z-position is corrected and therefore reflects that topography.

Constant height mode

Another possible mode of an STM is the *constant-height mode,* where the tip is kept in a plane of constant height above the sample surface, scanning in the same way as mentioned above but this time the feedback is turned off and the current signal is recorded. Compared with the constant-current mode, this mode has certain
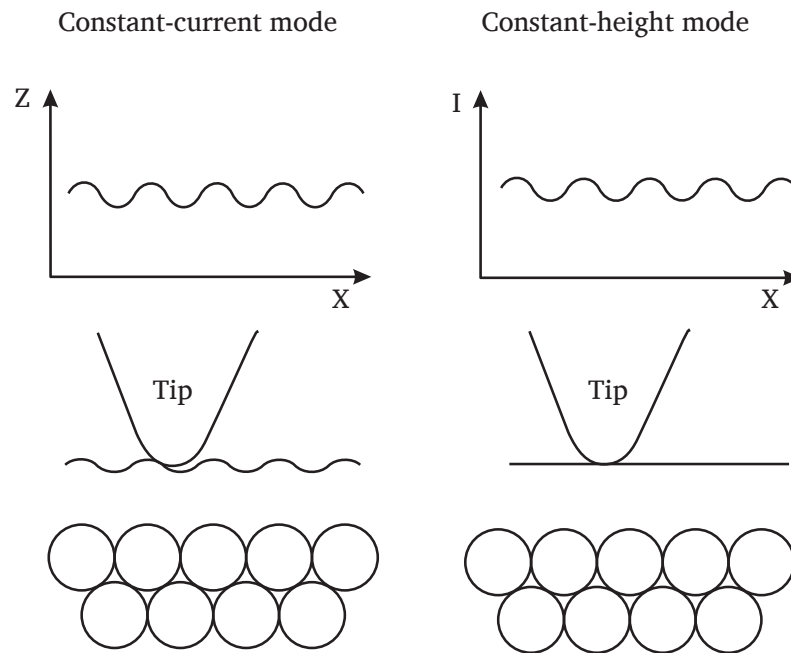
Figure 3.7:   **Constant-current mode and constant-height mode of the STM. (a)**
Recorded height profile (top) and tip movement (bottom) in constant-current mode. Primarily, the tip follows the topography of the surface, more precisely, it follows a surface of constant local density-of-states (LDOS). **(b)** Recorded current profile (top) and tip movement (bottom) in constant-height mode. This mode allows fast and more direct measurements of the LDOS, but it potentially yields a wide range of tunnel currents and is only suitable for very flat surfaces.

advantages and disadvantages. An advantage is that since no feedback is used, the scan speed can be much higher than in constant-current mode because the tip's z-position is not regulated. Also, if the samples' topography in an area is known to be flat, the recorded current map can be interpreted directly in terms of its electronic origin, whereas topographies measured in constant-current mode are potentially influenced by both topographic and electronic effects. On the other hand, this mode is limited to rather low surface corrugations and known surface slope, since without regulation the tip might either touch the sample or the current could fall below a measurable level. This often makes constant-height mode much less feasible in practice, and the constant-current mode is used throughout this work.

Point Spectroscopy

For this basic spectroscopic measurement, the STM tip is kept in a fixed position over the sample surface, usually by first setting certain *stabilization parameters* (bias voltage U_{stab} and current setpoint I_{set}), letting the regulation stabilize and then switching the feedback circuit off and keeping the tip in that position. Then, the current, $\text{d}I/\text{d}U$ and other quantities are recorded while a parameter like, e.g., the bias voltage is swept through a set range. An I-vs.-U curve for a point on

the sample surface can be recorded this way. The stabilization parameters determine the tip-sample distance during the measurement and are therefore always mentioned together with the results. A measurement of $\mathrm{d}I/\mathrm{d}U$ can be done either by numerically differentiating an $I(U)$ curve or by means of lock-in technique, i.e. by applying a small AC modulation voltage $U_{\mathrm{mod}} \approx 1\,\mathrm{mV}$ to $20\,\mathrm{mV}$ ($f \approx 1\,\mathrm{kHz}$ to $5\,\mathrm{kHz}$) to the bias voltage and feeding the current signal into a lock-in amplifier. Measurements with lock-in-technique offer a much improved signal-to-noise ratio compared to numerically derived $I(U)$-curves, at the expense of measurement time. Because of this, all $\mathrm{d}I/\mathrm{d}U$-measurements for this work were done with lock-in-technique.

Spectroscopic Fields

If such a measurement is performed on a rectangular grid, it is called *spectroscopic field*. Since now there is a spectroscopic curve (of length l) for each point in a ($m \times n$) grid, the result has the shape ($m \times n \times l$). Such a spectroscopic field can be very rich in information, since not only does it contain systematically obtained spectra of a sample area with an identical tip, which makes all the single spectra well comparable, but it also allows investigating the spatial extent and energetic development of spectroscopic features. One common and simple way to display such data is in the form of *slices*, all $\mathrm{d}I/\mathrm{d}U$-values on the grid at one voltage, e.g. in Figure 5.2. A downside of these measurements is that they can take significant amounts of time, on the order of hours.

Differential conductance maps

A much faster way to obtain a map of the $\mathrm{d}I/\mathrm{d}U$ intensity is to record the $\mathrm{d}I/\mathrm{d}U$ signal during a regular constant-current mode scan, simultaneously to and in the same way as the topography. If not full spectra are needed but simply the $\mathrm{d}I/\mathrm{d}U$ contrast at a certain voltage (here determined by the bias during scanning), this mode can be much more effective than taking full spectra. Since the $\mathrm{d}I/\mathrm{d}U$ signal is now obtained in constant current mode, cross talk between topography and $\mathrm{d}I/\mathrm{d}U$ signal is possible, because in contrast to the point spectroscopy mode the tip-sample distance is not inherently constant, but regulated by the feedback.

3.2   Tip-induced band bending

Up to now, we have assumed the sample to be metallic in the sense that its interior is fieldless, i.e. the electrical field in the vacuum gap does not enter the sample. Any potential applied at the samples' back contact will propagate up to the surface facing the STM tip, where (ideally unlimited) surface charges accumulate.

Semiconductors on the other hand feature a band gap at the Fermi energy, which means that they do not in general have the ability to accumulate charges with a density sufficient to completely screen the tip potential right at the surface. Instead, the electrical field enters a certain volume of the sample if the Fermi
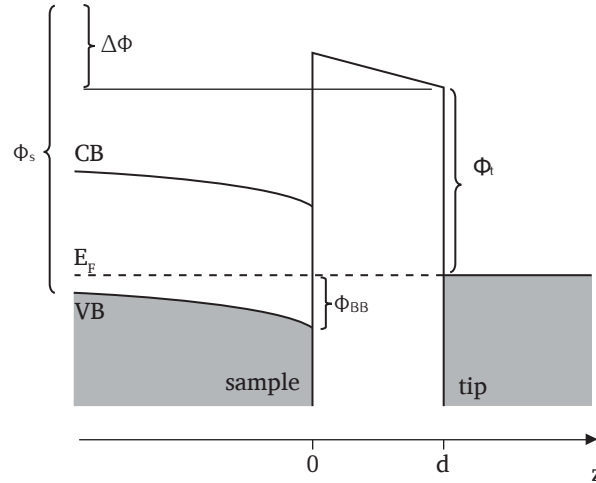
Figure 3.8: Tip induced band bending at zero bias. If no bias is applied, the difference between semiconductor and tip work functions (in our case $\Delta\Phi = \Phi_s - \Phi_t = 0.8\,\text{eV}$) lead to downwards bending of conduction band (CB) and valence band (VB) at the sample surface. Part of $\Delta\Phi$ drops within the sample due to charge accumulation, the rest drops linearly across the vacuum gap.

level is unpinned. That volume is often called space charge region, since the charge needed to screen the tip potential is spread out over it, determined by the materials limited capacity to accumulate charge.

Within this space charge region, the presence of the charges creates a locally varying electrical potential. At every point in the sample, this potential shifts the semiconductor bands accordingly. At the sample surface, the energy bands shift up or down towards the STM tip, depending on differences in tip and sample work functions and on the potential difference across the vacuum gap, which has led to the term *tip-induced band bending*. The bands stay parallel to each other since the width of the band gap is an intrinsic property of the material. Figure 3.8 illustrates this situation.

Since band bending shifts the sample LDOS and is affected by the applied bias, we have a situation where the measurement process and the measurement parameters affect the configuration of the sample. So a reasonably accurate picture of the band bending will be crucial to our understanding of measurement results.

For the following we assume that equilibrium has been reached, meaning the Fermi levels of tip and sample have aligned, either by tunneling electrons or by shorting tip and sample, i.e. applying a bias of $0\,\text{V}$. If we apply an additional bias voltage U to the sample, we can already calculate the surface potential in a very straightforward way. The difference between tip work function and sample work function plus the applied sample bias equals the total potential drop:

$$\Delta\Phi = \Phi_t - (\Phi_s - eU) \tag{3.17}$$

In our case the semiconductor's work function (p-InAs: $5.3\,\text{eV}$) is larger than the tip's work function (W: $4.9\,\text{eV}$). Therefore at zero bias, there will be an accu-
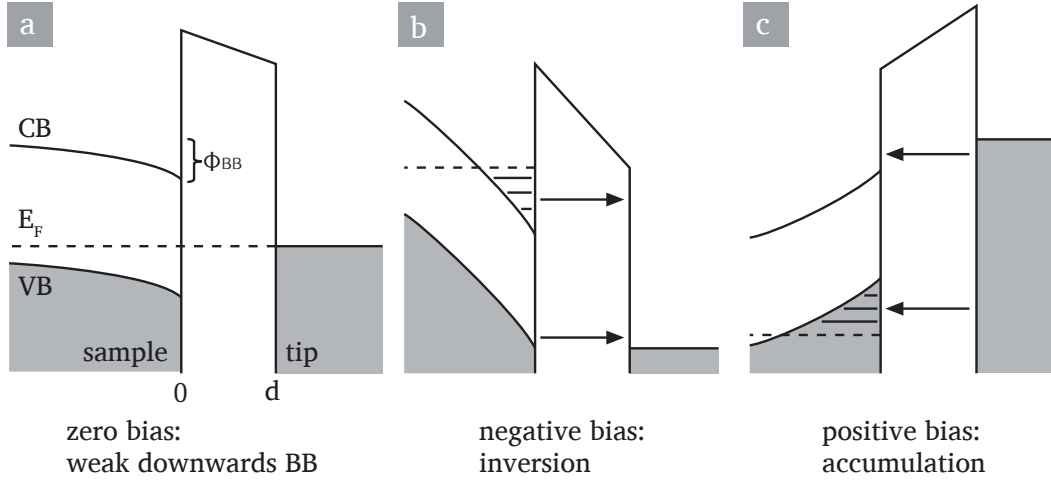
Figure 3.9: Tip induced band bending and states contributing to the tunnel current at zero, negative and positive bias. (a) At zero bias, there is downwards band bending and no juxtaposition of unoccupied and occupied states and therefore no tunneling. **(b)** At negative bias the downwards band bending is increased. Tunneling happens between valence band and unoccupied tip states; if conduction band states are occupied, also from those. If the conduction band edge gets pushed below the bulk Fermi energy a triangular potential well is created, in which quantum dot states can exist. **(c)** At positive bias, the bands are pushed upwards at the surface. Tunneling happens from tip states to conduction band states. Again, a triangular well is formed, in which quantum dot states can exist and participate in tunneling.

mulation of negative charges in the sample and positive charge at the tip surface. As there are now charges on both sides of the vacuum gap, there is an electric field from the tip to the sample.

The above mentioned $\Delta\Phi$ is the total energy shift between the metal and the region of the semiconductor with flat bands. This potential difference drops partly in the vacuum and partly in the semiconductor. If we call the amount of band bending at the semiconductor surface Φ_{bb} and the tip to sample distance d, we get

$$\frac{\Delta\Phi}{e} = d\left(\frac{\partial U}{\partial z}\right)_{z=0} + \frac{\Phi_{bb}}{e}$$

We use a z-scale where the sample surface is $z = 0$ and z increases into the vacuum and towards the tip and is negative inside the sample. Above, $\left(\frac{\partial U}{\partial z}\right)_{z=+0}$ is the potential gradient in the vacuum.

To get a deeper understanding of the spatial structure of the space charge region, we need to calculate the actual charge density which accumulates. A typical procedure of finding the local charge density and electrostatic potential is to first determine the samples' Fermi energy, then calculate the electrostatic potential at the sample surface Φ_{bb}, then use the fact that charge density and curvature of the potential are proportional and integrate the potential gradient

going into the bulk of the sample until zero potential[†] is reached. This is basically a one-dimensional approach, but can be generalized to a two-dimensional or even three-dimensional treatment.

The Fermi energy E_F needed in the first step is temperature dependent, since the width of the Fermi distribution affects the occupation statistics. The correct value can be found by taking the temperature dependent Fermi function and the density-of-states functions of valence band, conduction band, acceptors and donors, and looking for a value of E_F that provides charge neutrality. (see [89] sections 4.4-4.7).

The surface potential is found from the continuity principle for the electrical displacement at the sample surface. At the boundary between sample and vacuum ($z = 0$), the electric field in the semiconductor $\mathcal{E}_{sc}$ and in the vacuum $\mathcal{E}_{vac}$ and the electric potential U must satisfy

$$\mathcal{E}_{vac} = \epsilon_{sc}\mathcal{E}_{sc}$$

$$\mathcal{E}_{vac} = -\epsilon_{sc}\left(\frac{\partial U}{\partial z}\right)_{-0}$$

The local potential and the charge density always satisfy Poisson's equation:

$$\Delta U(\vec{r}) = -\frac{\rho(\vec{r})}{\epsilon_{sc}\epsilon_0} \tag{3.18}$$

So we can find the local potential by integrating the electric field, itself the integral of the charge density. But additionally, the local potential also determines the occupation statistics of the bands and dopants and therefore the charge density according to:

total charge density:
$$\rho(\vec{r}) = e\left(N_A^-(\vec{r}) - N_D^+(\vec{r}) + n(\vec{r}) - p(\vec{r})\right) \tag{3.19}$$

electron density in conduction band:
$$n(\vec{r}, T) = \int_{E_C(\vec{r})}^{\infty} D_C(\epsilon)\, f(\epsilon)\, d\epsilon \tag{3.20}$$

hole density in valence band:
$$p(\vec{r}, T) = \int_{-\infty}^{E_V(\vec{r})} D_V(\epsilon)\left[1 - f(\epsilon)\right] d\epsilon \tag{3.21}$$

Fermi function:
$$f(x) = \frac{1}{1 + e^{(x - E_F)/k_B T}}$$

with N_A^-: density of charged acceptors E_C: conduction band minimum

        N_D^+: density of charged donors E_V: valence band maximum

---

[†]or something close enough
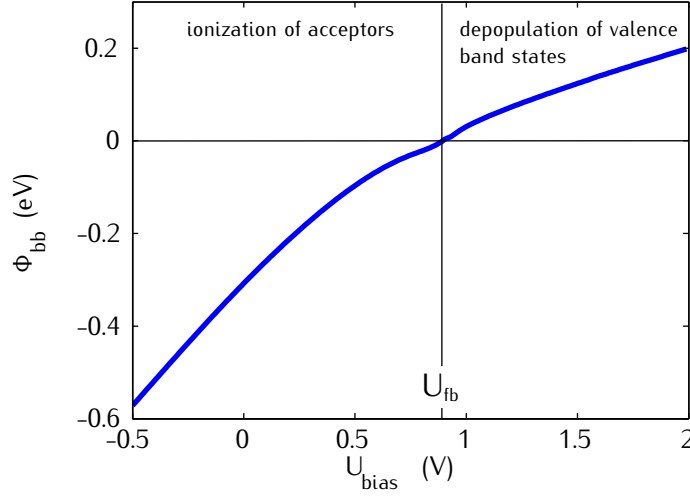
Figure 3.10: Calculated surface band bending versus bias voltage. The curve shows the amount of band bending at the sample surface. Flat bands ($\Phi_{bb} = 0$ eV) occur at about 0.8 V. Below this voltage, negative charge is accumulated throug ionization of acceptors. Above this point, positive charge is accumulated through depopulation of valence band states. The different slopes of Φ_{bb} vs. U_{bias} are caused by the different densities of states of dopants and conduction band.

If there are no quantum dot states in conduction or valence band, one can use the density of states of a three-dimensional electron system, which is

$$D_{C/V}(\epsilon) = g_S g_V \frac{(2m^*_{C/V})^{3/2}}{4\pi^2\hbar^3} \sqrt{|\epsilon - E_{C/V}|} \tag{3.22}$$

where m^*_C: electron effective mass g_S: spin degeneracy

             m^*_V: hole effective mass g_V: valley degeneracy

This determines the band bending at the semiconductor surface ϕ_{bb} and the local energetic position of the band edges, which in turn determines the occupation ratio and therefore the charge density. This can be optimized until a self-consistent solution is found. Figure 3.10 shows a result of such a calculation for our sample system. More examples of calculated charge densities and band bending profiles will appear in Chapter 5 and Chapter 6. Above the flat band voltage, there is upwards band bending and conduction band states become depopulated. Below flat band voltage, there is downwards band bending and acceptors are pushed below the Fermi level and become negatively charged. Due to the higher density of states in the valence band compared to the acceptor states, less band bending is needed to accumulate holes in the valence band than electrons on acceptors. This is reflected in the different slopes of Φ_{bb} vs. U_{bias}, ca. 0.2 eV/V above U_{fb} and about 0.4 eV/V for lower voltages.

3.3   Experimental setup

Two different STM systems were used for this study. The purpose of this section is to describe the two systems, their overall layout, their abilities and properties. Both are multi-chamber UHV-systems with the STM in a cryostat and each with a superconducting magnet to apply high magnetic fields. Both microscopes offer the possibility to exchange STM tips.

Ultra High Vacuum

Semiconductor surfaces like those prepared in this study are chemically rather reactive. But even metal surfaces tend to immediately form an oxide layer when exposed to ambient conditions. Therefore sample and tip preparation as well as STM measurements are performed in steel chambers under ultra high vacuum (UHV) conditions, i.e. at pressures below 1×10^{-10} mbar.

Ultra high vacuum is achieved and maintained by means of a variety of vacuum pumps with different working principles. Turbo-molecular pumps with auxiliary roughing pumps are able to remove most of the air from the system and achieve pressures down to 1×10^{-6} mbar within a short time. Ion getter pumps and titanium sublimation pumps become most effective in the low pressure regime and are able to reach and maintain ultra high vacuum down to 1×10^{-11} mbar.

3.3.1   6 K UHV STM system

This system was designed and built in the group in the course of two PhD theses[25; 112; 114]. It provides the ability to perform all necessary sample and tip preparation procedures *in-situ*. The cryostat consists of a liquid helium dewar with 100 L capacity, surrounded by an isolation vacuum. The cryostat is situated in a pit in the ground below the horizontal transfer axis across the three upper chambers (see Figure 3.11). To improve vibrational decoupling of the boiling helium from the STM, the thermal contact to the inner wall facing the STM is provided by a small intermediate volume filled with helium exchange gas. The system keeps its base temperature of slightly above 6 K for about 70 hours after filling.

The system is also equipped with two superconducting magnets in the helium bath around the STM position. One magnet is able to generate a field of up to 6 T perpendicular to the sample surface, and a split pair magnet can produce a field of up to 2 T parallel to the sample surface. Operating both magnets at the same time, fields of up to 1 T[‡] with arbitrary directions in a plane defined by the two field directions can be generated.

A front and top view of the whole system is given in Figure 3.11 and Figure 3.12. On the left hand side the system features a load lock where samples

---

[‡]due to the critical fields in the coils
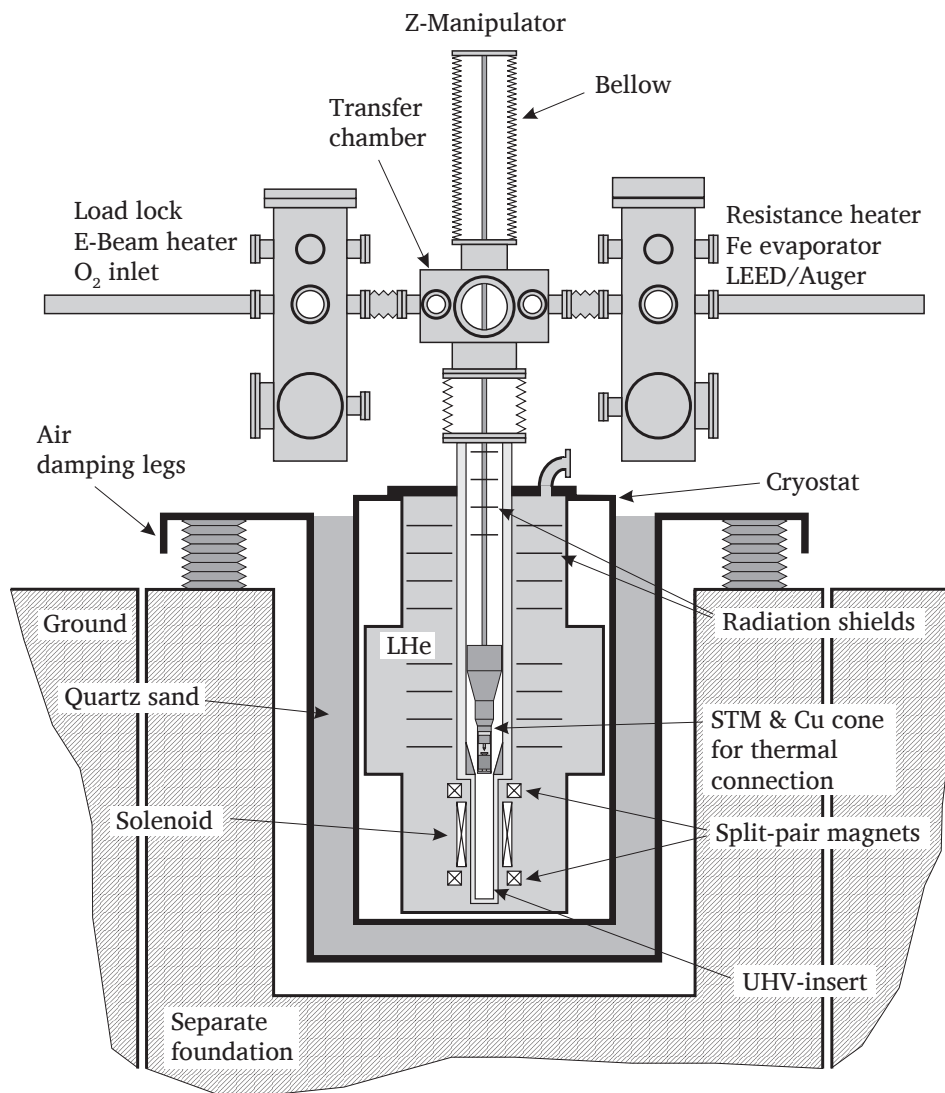
Figure 3.11: **Front view of the 6 K UHV-system with the cryostat at the bottom.** (Source: [112])

and tips can be introduced. The chamber on the left hand side contains an electron beam heater which was used for tip preparation, while all evaporators are situated in the chamber on the right hand side.

The STM is mounted at the bottom of a long insert which is moved up and down from the outside with a large z-manipulator. Measurement position is the bottom position. To exchange samples and tips, the STM is lifted up to the transfer axis.

Several techniques to reduce vibrations are implemented. The whole UHV chamber including the cryostat is mounted on a rigid steel frame which rests on air filled damping legs. These passive damping legs attenuate external noise at frequencies of 1 Hz and above. The isolation-vacuum chamber containing the dewar rests in a bed of sand where vibrational energy can dissipate and which
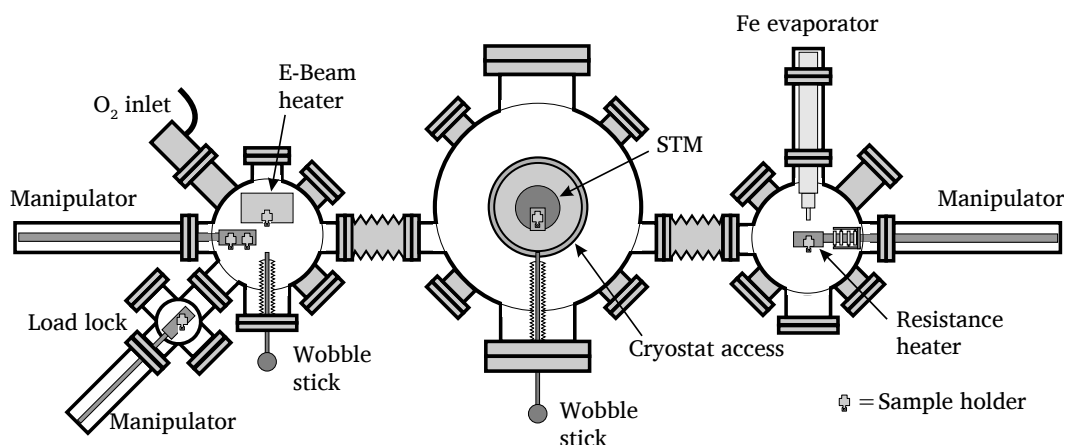
Figure 3.12: **Top view of the 6 K UHV-system.** The central chamber is located on top of the cryostat and is used for sample transfer and storage. The left chamber has an e-beam heater and is connected to the load lock, while the right chamber contains another sample heater and the evaporators. (Source: [112])

provides further damping mass. The room housing the system has special acoustic damping, and the room's foundation rests on sand, separated from the building's foundation.

At the time of the measurements for this study, the STM electronics consisted of a TOPSystem II transputer which implemented basic measurement function and a control PC displaying the user interface. The software of the transputer and the control PC had been developed at this university, especially for this system[25].

3.3.2   4 K/300 mK UHV STM system

The other system used in this study was designed and built by Jens Wiebe[107; 109] and Andre Wachowiak[105]. It features a 14 T magnet and, in addition to a combined liquid nitrogen/liquid helium bath cryostat providing a base temperature of 4 K, has an additional ^{3}He cryostat to reach 300 mK.

Figure 3.13 gives an overview of the UHV system. The appearance is dominated by a large barrel at the center, which contains the bath cryostat in a sand bed. Figure 3.14 shows a cut through the barrel, showing the sand bed and the cryostat. A superconducting magnet is located at the bottom of the helium dewar. In the UHV part the STM is mounted on a bottom loaded insert, which at the bottom is encased in a radiation shield. To perform measurements the STM is moved into the cryostat, in this case the upper position. To access the STM and to exchange tip or sample, the STM is moved down into a chamber below the barrel. Whereas in the other system, the insert movement was realized with a large steel bellow, here the lower part of the insert is moved by a traveling nut on a rotating thread. Only a rotary feed-through is needed to move the insert.

Below the barrel there are three separate UHV chambers. The one right under the cryostat is the place where samples and STM tips are exchanged in the micro-
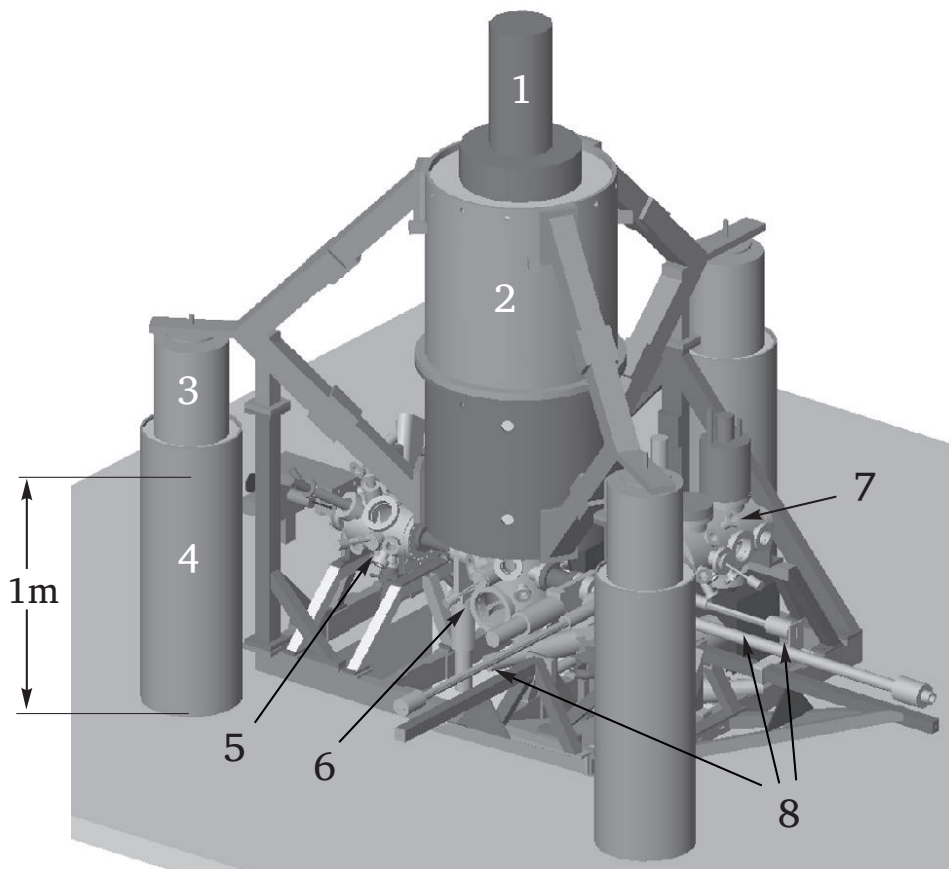
Figure 3.13:   **Overview of the 4 K/300 mK UHV STM system. (1)** Cryostat, **(2)** Barrel, **(3)** Air damping legs, **(4)** Sand barrels, **(5)** Preparation chamber, **(6)** Transfer/STM chamber, **(7)** RT-STM/LEED chamber, **(8)** Manipulators. (Source: [70])

scope, as well as stored. The chamber is further equipped with a triple evaporator to deposit onto a cold sample in the STM.

The chamber on the right in Figure 3.13 contains a room-temperature STM of the exact same design as the low-temperature one, plus a LEED/Auger unit and an evaporator. The chamber on the left contains an x-y-z manipulator equipped with an electron beam heater. Two ion guns are installed in the chamber, one optimized for high sputter rates, the other with a Wien-filter for higher ion beam purity. Furthermore, two metal evaporators are mounted to the chamber, containing iron and chromium.

The cryostat

As was mentioned above, the cryostat on this system is significantly more complex than the one on the 6 K-machine. The bath cryostat has dewars for liquid nitrogen (outer) and liquid helium (inner). This system of combined nitrogen and helium bath cryostats is able to keep the microscope at 4.2 K for about 5 days with one filling.
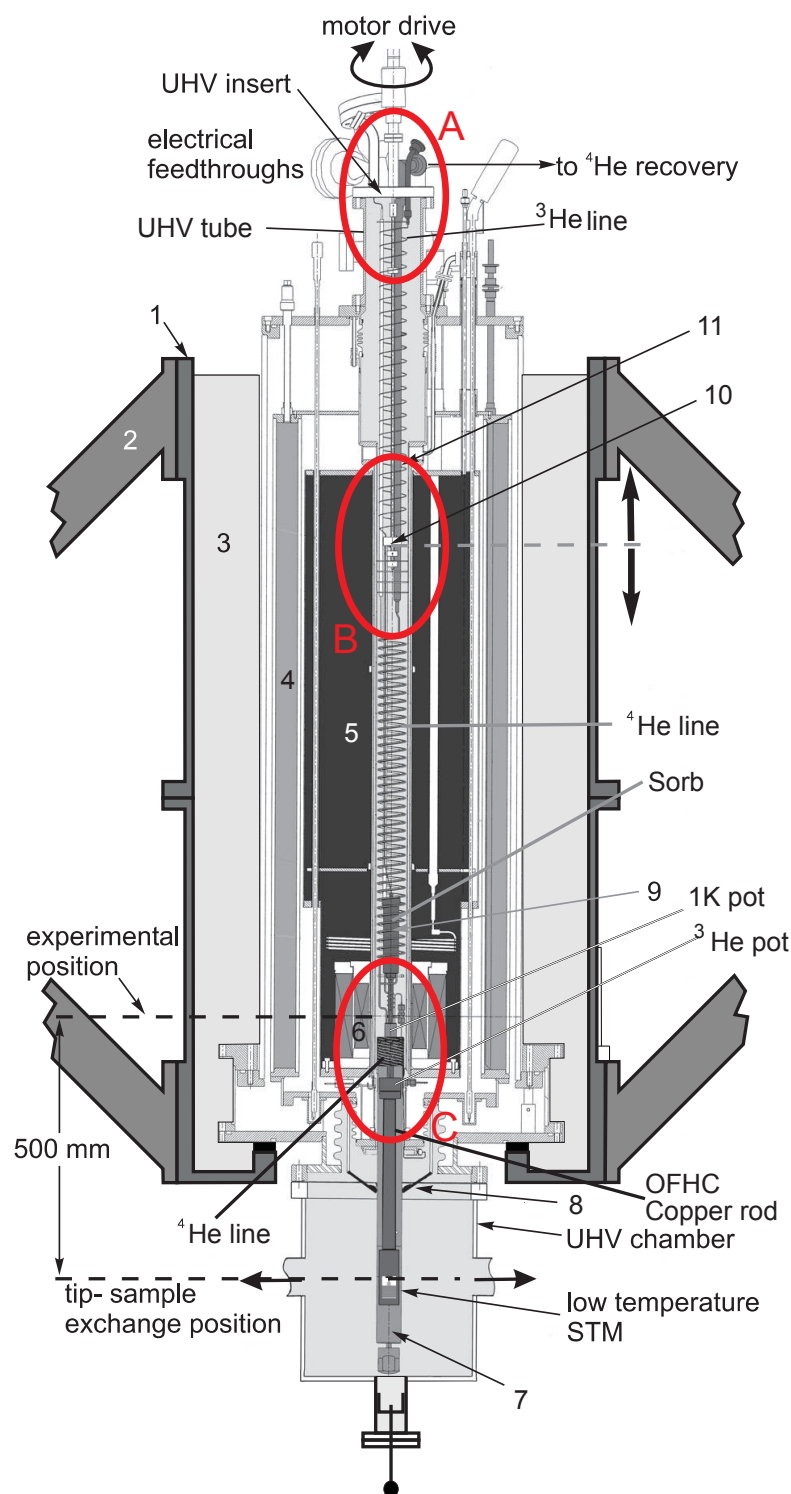
Figure 3.14: Section view of the 4 K/300 mK cryostat. The insert at the center contains the ^{3}He-refrigerator and the STM. It is shown in the bottom position used for sample exchange. The red circles highlight the three areas where improvements had to be made to the system. **(1)** Outer barrel, **(2)** Steel frame, **(3)** Sand, **(4)** Liquid nitrogen dewar, **(5)** Liquid helium dewar, **(6)** Magnet coils, **(7)** Thermal shield around STM, **(8)** Metal flaps for thermal shielding, **(9)** ^{4}He capillary, **(10)** Traveling nut , **(11)** ^{4}He line. (Source: [70])

The central insert features a ^{3}He refrigerator for cooling the STM. It consists of a closed volume with a fixed amount of ^{3}He and an internal sorption pump. This system is able to cool the microscope to about 300 mK for about 30 hours. After that, ^{3}He has to be re-condensed. The base temperature hold time can be extended by further pumping the 1 K pot at the expense of extra ^{4}He.

While not having a large bellow is an advantage, the fact that the insert with its numerous electrical wires and gas capillaries extends and contracts within the UHV creates new technical challenges. During the time of this study three problems appeared and had to be solved. First, several turns of the ^{4}He capillary between the ^{4}He dewar and the insert got stuck at the 1 K pot (marked as area **C** in Figure 3.14). This was fixed by replacing the capillary and fixing its top two turns to the 1 K pot to avoid the capillary slipping above it. Later, a ^{3}He capillary leading from the insert to the top of the cryostat and to an external ^{3}He storage broke from mechanical stress and became leaky (area **B**). The cause of this was found to be a disadvantageous arrangement of the capillary close to the bottom fixation. As a result, a sharp turn of the capillary was bent repeatedly during every movement of the insert, causing the material to weaken and finally develop a leak. The leaky area was visually inconspicuous and could only be found in a thorough search with a helium sniffer. To avoid opening and possibly contaminating the ^{3}He volume, the leak was fixed without cutting the capillary open. In order to seal the leak, silver solder was soldered onto the faulty area. To mechanically fixate the section of the capillary which is exposed to the highest mechanical stress, a fixation structure was added. Apart from fixating the capillary, the structure also acts as a guiding spike for the insert in the UHV tube.

Also, the original rotary feed-through at the top of the cryostat failed and had to be replaced (area **A** in Figure 3.14). The type of feed-through originally built into the system turned out to be inadequate for the normal frequency of insert motions. It was replaced with a magnetically coupled rotary feed-through and an additional gear to support the weight of the insert. Also, after five years of operation, the traveling nut on the insert became worn out, causing the insert to get stuck. The traveling nut was replaced with a new identical part and was equipped with new and improved lubrication.

The STM

A photograph of the STM used in this system is shown in Figure 3.15. It is a home built STM based on the original Pan-design[82; 114]. The design is optimized to be very compact and rigid to make it less susceptible to vibrations. The main body is made from a copper alloy called phosphorus bronze, which is nonmagnetic and UHV-compatible, and is gold-plated. The design combines all electrical connections in a plug at the top to simplify the exchange of the STM in the chamber.

The vertical motion range of the tube scanner is physically limited to several hundred nanometers, enough for tracing the surface in a measurement. But to safely exchange samples and tips, both have to be separated by a few millimeters.
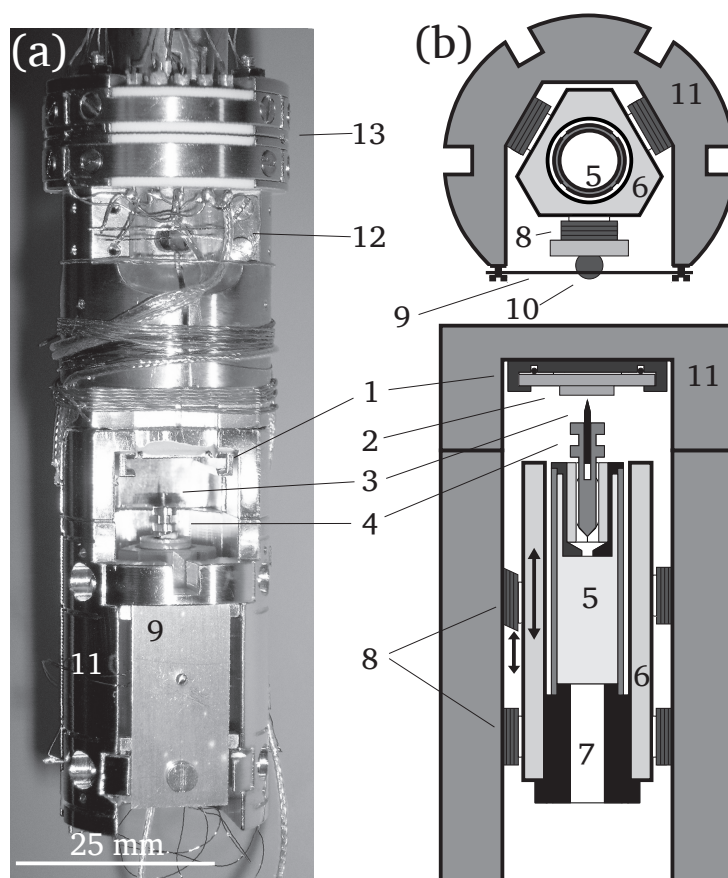
Figure 3.15: **Photograph and schematic view of the low-temperature scanning tunneling microscope.** (1) sample stage, (2) sample, (3) STM tip, (4) tip holder, (5) tube scanner, (6) sapphire prism, (7) macor plug, (8) piezo walker stacks, (9) spring plate, (10) metal ball, (11) gold plated STM body, (12) temperature sensor, (13) electrical plug. (Source: [109].)

Therefore a method of coarsely moving tip and sample towards and away from each other is needed. In the Pan design, this is provided by a so called *walker* motor. The scan tube with the tip is mounted inside a prism made of sapphire. This prism is held within stacks of piezo material sheets pressing at it from each side. Applying a saw tooth high voltage signal to the piezo stacks moves the prism along its center line in a stick-slip fashion. When at rest, this motor does not contain movable parts. The amazing stability of this motor design in addition to a very compact and rigid microscope body lead to an excellent overall mechanical stability of the setup. This has proven valuable over and over again, especially when other means of vibration damping or -isolation are exhausted.

At base temperature the tube scanner provides an x-y-range of about $1 \times 1 \,\mu$m and a z-range of about $200 \,$nm. Due to the high magnetic fields in the experiment of up to $12 \,$T, magnetic materials had to be carefully avoided. The first STM in the setup had to be replaced for this reason, since there turned out to be a nickel wetting layer below the gold plating of the STM body, which had been

added, presumable to facilitate the gold-plating process. At high fields, this created enough force to deflect the whole microscope until it touched the radiation shield. The current microscope without nickel coating allows measurements at full field intensity.

3.3.3 Tip preparation

Tips are electrochemically etched from a tungsten wire[34] and after being brought into UHV they are flashed to about $1200\,^{\circ}$C for a short time. This removes any oxide at the surface and also tends to yield tips which are relatively blunt at the end which is beneficial in terms of stability for spectroscopic measurements.

STM tips are moved within the UHV system in a so called *tip shuttle*, which matches the dimensions of a sample holder and can therefore be moved about and stored just like any sample. Also all preparation facilities like heaters, sputter guns and evaporators can be used with both samples and tips.

Chapter 4

Sample preparation and characterization

This chapter describes the basic properties of the samples used for this study. Their bulk magnetic properties are determined through magnetization measurements and their fundamental appearance in STM and STS are described. A method to determine the embedding depth of manganese acceptors below the InAs(110) surface is presented. Using this method and results of the magnetization measurements, the samples' Mn-related doping density is determined.

4.1   Mn-doped InAs samples

The primary goal of this study was to look for the local electronic properties of manganese acceptors in a III-V semiconductor. Therefore we chose low doped samples to get sufficiently separated manganese impurities and avoid additional interaction effects.

Since the manganese densities are well below the solubility limit the samples are virtually free of unwanted defects such as interstitial Mn, MnAs clusters or Mn antisites which are otherwise found in highly manganese doped samples and which cause self-compensation of carriers and magnetic moments.

Two differently doped samples were studied. Both are commercially available Mn-doped InAs crystals grown using the CZOCHRALSKI process[21]. The first sample has a rather low doping density of about $5 \cdot 10^{16}/\text{cm}^3$, while the second has a doping density of about $5 \cdot 10^{18}/\text{cm}^3$. Additionally, an undoped sample was used as a reference in the magnetization measurements (Section 4.2). This sample had a carrier density similar to the lower-doped samples and allows us to account for magnetic effects of the free carriers. The following table gives the details of these crystals.

	Source	Charge	Carrier Density at 77 K	Cond. Type	Dopant	Mn content
low-doped	CrysTec	S 2278	$3.8 \cdot 10^{16} \mathrm{cm}^{-3}$	p	Mn	$0.000\,21\,\%$
high-doped	MaTecK	—	$5.0 \cdot 10^{18} \mathrm{cm}^{-3}$	p	Mn	$0.028\,\%$
reference	CrysTec	S 4245	$1.8 \cdot 10^{16} \mathrm{cm}^{-3}$	n	intrinsic	$0\,\%$

Table 4.1: **Sources and parameters of the samples.**

The carrier densities reported by the manufacturers are not necessarily identical to the doping density. The charge carrier density is obtained by the manufacturer in van-der-Pauw style[83] transport measurements and is the only indication of the actual doping density given in the data sheet. It is, however, only roughly related to the manganese content.

The intrinsic doping of an InAs crystal (from inevitable contamination) is n-type. As a consequence, a certain amount of Mn doping embedded during growth is not accounted for in the measured carrier density, as it is compensated by the intrinsic doping. Also, a measurement of the carrier density is always temperature-dependent, which is an additional source of discrepancy.

To determine the dopant density from the carrier density, the sample needs to be in the extrinsic saturation regime, i.e. the temperature needs to be high enough so that all dopants are ionized, i.e. activated. This is not necessarily true for the measurement done by the manufacturer at 77 K.

Therefore, this makes an additional means of determining the density of manganese dopants necessary. A simple way of finding the dopant density can be done by counting in STM images. This method will be applied in Section 4.5. Another independent way of determining the number of dopants in the material is through magnetization measurements, which is the focus of the next section.

4.2   Bulk magnetic properties

While magnetic measurements were not the primary goal of this study, they were necessary in order to determine the basic properties of our samples at the experimental temperatures. The samples used for this study had a low manganese content in order to get isolated individual acceptors. Mn-doped InAs with a manganese concentration up to at least $x = 0.14\,\%$ have been found to be paramagnetic even at very low temperature, as known from magnetization measurements with a SQUID[*]-magnetometer[96]. Nevertheless, this needed to be verified experimentally for our samples since at the given dopant concentrations, there may be blocking at 4 K.

---

[*]Superconducting Quantum Interference Device
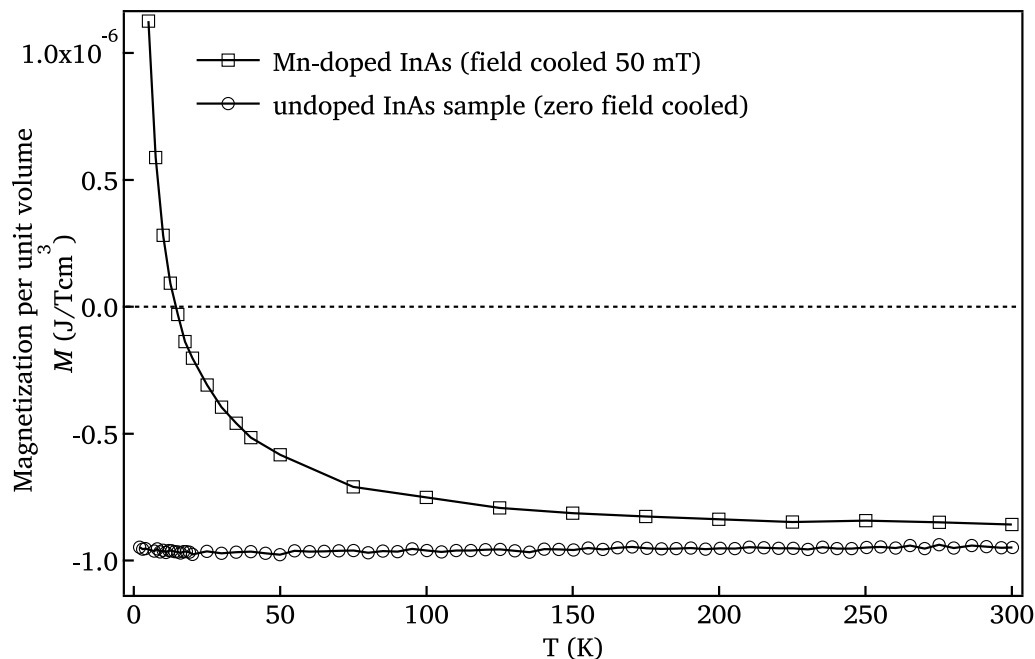
Figure 4.1: **Magnetization measurements of undoped and Mn-doped InAs samples.** The undoped InAs sample shows a purely diamagnetic response (circle markers). The Mn-doped sample (square markers, doping density: $5 \times 10^{18}\,\text{cm}^{-3}$, $x = 0.028\,\%$) shows an additional paramagnetic response, which is strongly temperature dependent.

The magnetization measurements were done with a SQUID-magnetometer in a cryosystem with a base temperature of $2\,\text{K}$ containing a superconducting magnet with a maximum field of $1\,\text{T}$. Two types of measurement were done. In the first, the sample is cooled down to $2\,\text{K}$, either with an external magnetic field applied (*field cooled*) or without (*zero field cooled*). Then the sample's magnetization was recorded while the temperature was increased to room temperature.

The second type of measurement was the typical magnetization curve measurement, where the external field is repeatedly swept to high positive and negative values and the sample's magnetization in response to the external field is recorded.

Figure 4.1 shows the temperature dependent magnetization of the highly doped ($5 \times 10^{18}\,\text{cm}^{-3}$) and the undoped sample. The InAs host material shows its own magnetic response, which is purely diamagnetic, i.e. opposite to the external field and practically temperature independent. The Mn-doped sample shows an additional paramagnetic response, which is superimposed on the diamagnetic background. In order to isolate magnetic effects of the Mn doping from this background, the signal of the undoped reference sample was subtracted from the magnetization curve of the Mn-doped samples. This "relative" signal without the diamagnetic component is shown in Figure 4.2. The figure shows the combined results from a field cooled run ($0.05\,\text{T}$) and a zero field cooled sample. The two curves fully coincide, showing no indication of ferromagnetic behavior or superparamagnetic blocking.
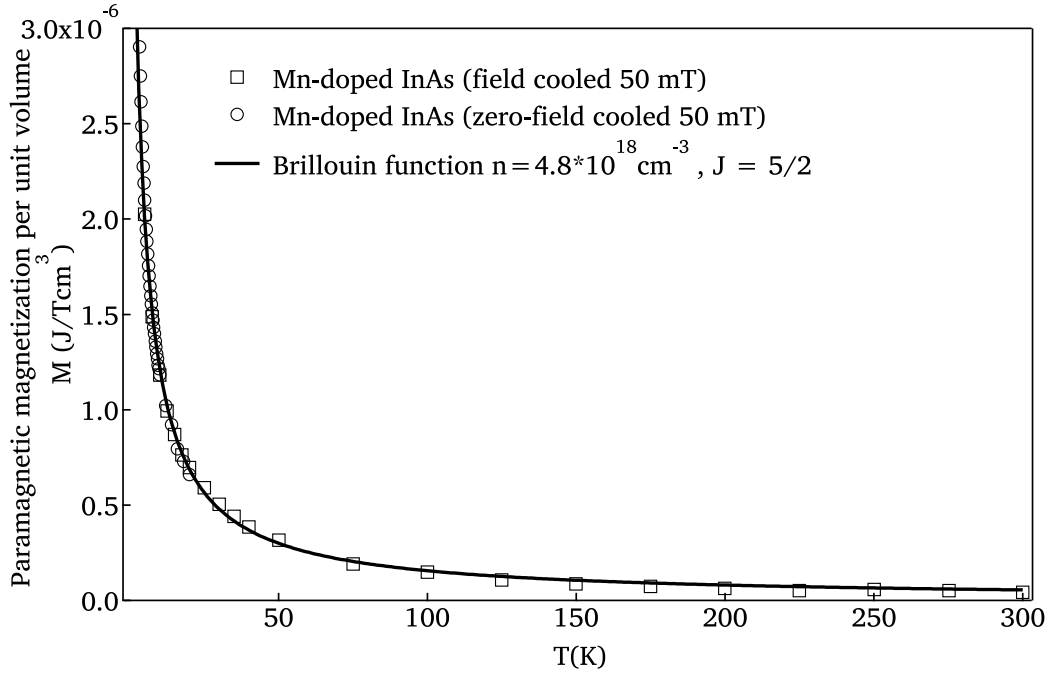
Figure 4.2: Paramagnetic response of the Mn-doped InAs sample (5×10^{18} cm^{-3}). The diamagnetic component as obtained on the undoped sample is subtracted. Results from a field cooled sample and a zero field cooled sample are shown. Both results coincide, indicating that even at very low temperatures, the Mn-doped sample shows no ferromagnetic behavior or superparamagnetic blocking. The line corresponds to a fit of the Brillouin function (see text) to the data with the indicated values of atomic spin and doping density.

The observed behavior matches the quantum mechanical description of paramagnetism. Therefore the data was fitted using the magnetization of an ideal paramagnet:

$$m = n g \mu_B J \cdot B_J(x)$$

where n is the density of magnetic centers, g is the LANDÉ factor and B_J is the Brillouin function:

$$B_J(x) = \frac{2J+1}{2J} \coth\left(\frac{2J+1}{2J}x\right) - \frac{1}{2J}\coth\left(\frac{1}{2J}x\right)$$

and x is the ratio of the Zeeman energy of the magnetic moment in the external field to the thermal energy $k_B T$:

$$x = \frac{g\mu_B J B}{k_B T}$$

J was set to $^5\!/_2$ and only the Mn density was a free parameter for the fit. The assumption of $J = ^5\!/_2$ for the total angular momentum reflects the ionized Mn acceptor in the A$^-$ configuration (see Section 2.4.1). The optimal fit was achieved
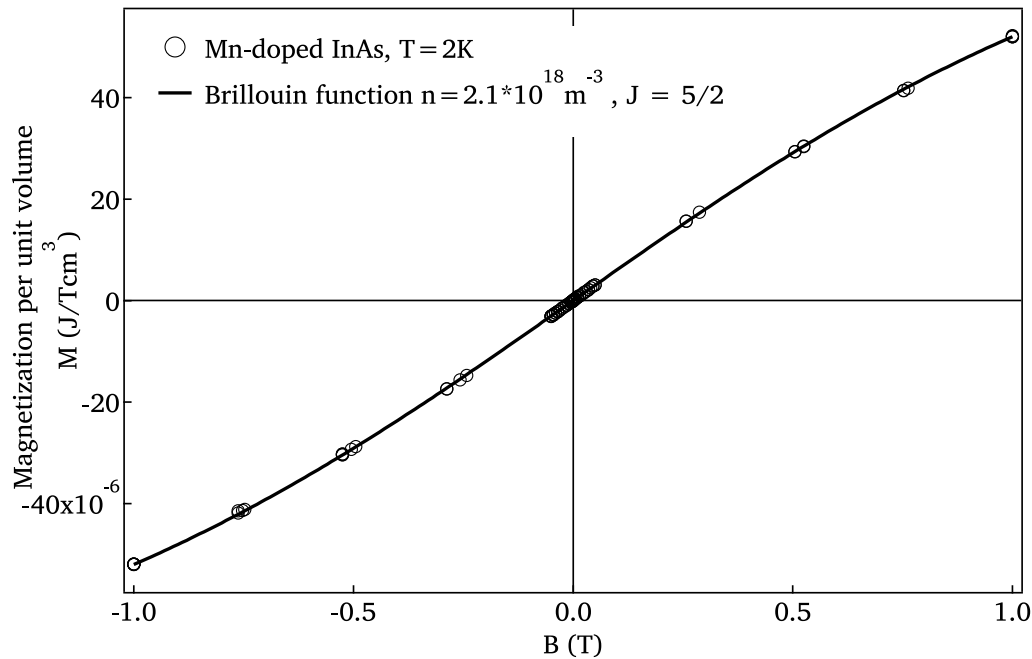
Figure 4.3: Magnetization curve of Mn-doped InAs at 2 K over a range of ± 1 T. The B-field was swept from 0 T to -1 T to 1 T and back to -1 T. No remanence can be found. The line shows a fit of the Brillouin function for the indicated values of spin and doping density.

for $n = 4.84 \times 10^{18}/\mathrm{cm}^3$, which is very close to the carrier density given in the data sheet.

Figure 4.3 shows the field-sweep results obtained from the doped material ($5 \times 10^{18}/\mathrm{cm}^3$). No remanence is found, which again shows that the samples do not exhibit ferromagnetism, even at very low temperatures.

In this case, no reference sample was measured. Therefore the diamagnetic and paramagnetic contributions can not be easily separated in the overall magnetization. Due to the partial compensation of the paramagnetic contribution by the diamagnetic component, the Brillouin fit in Figure 4.3 yields a moment density of only $\approx 2 \times 10^{18}/\mathrm{cm}^3$.

In summary, the SQUID measurements demonstrate that the specified carrier density is close to what was given on the data sheet. Furthermore, there is no ferromagnetic blocking behavior in these systems at the temperatures used in the STM experiments.

4.3   Sample preparation for STM

The samples were obtained in the form of small single-crystal rods with a 3 mm×3 mm base and a length of about 30 mm. The base plane was oriented along (110), which is the natural cleavage plane of InAs as well as of the other zinc-blende semiconductors. Due to the rather high reactivity of semiconductor
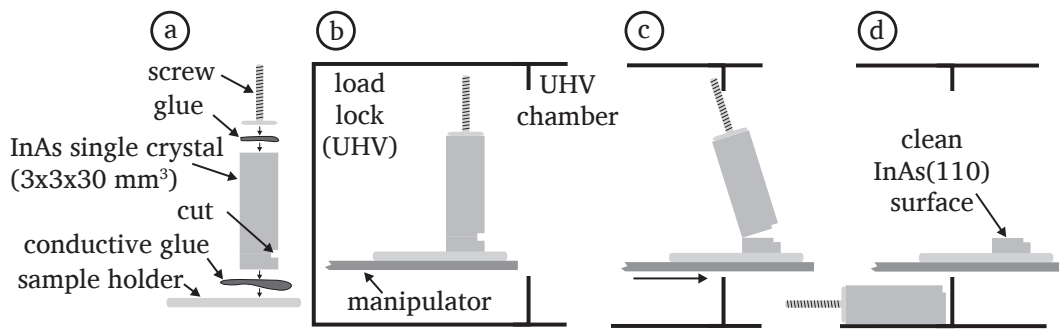
Figure 4.4: **Sample preparation and cleavage.** The semiconductor crystal is cut at the base, then glued to the sample holder and mounted in the load lock. Once a sufficiently low pressure is achieved, the sample is moved forward against an edge of the chamber and is cleaved. The broken-off top of the crystal is recovered and used again. (Source: [56])

surfaces and the — compared to metals — limited means of surface preparation, surfaces are prepared by cleaving *in situ* under UHV conditions.

To achieve this, the following procedure has been developed and refined in our group: First, to make the sample longer and facilitate cleaving, a $\approx 30\,\mathrm{mm}$ long M1.2 stainless steel screw is glued to one end of the crystal rod. Then, using a low speed diamond saw a small cut parallel to the surface is made close to the base of the crystal rod, as shown in Figure 4.4. The crystal is then glued to a tungsten sample holder using conductive epoxy glue (H20). Next, the sample is mounted on the retracted transfer rod in the load lock of the UHV system. The load lock is then baked out for several hours at $\approx 120\,°\mathrm{C}$. After cooling down, the valve between the lock and the UHV system is opened. The main part of the load lock is a 6-end NW35 cross, where the sample, due to its height, only fits in the center area. When the transfer rod is moved forward into the chamber, the upper part of the crystal/screw hits the wall of the lock and causes the crystal to cleave at the prepared notch. The small piece below the notch left on the sample holder is the sample, while the top part falls down in the lock to be recovered and used again in the same manner. This way, virtually defect-free surfaces can be prepared reliably with relatively little effort. If the sample is transferred into the STM in a matter of a few minutes, the adsorbate density remains below one per $10^5\mathrm{nm}^2$ [56]. In a low temperature UHV system with cryogenically improved pressure, such a surface can stay sufficiently clean for months.

InAs, due to its rather narrow band gap, forms highly conductive ohmic contacts when interfacing metals[72; 85; 116]. So, unlike for other III-V semiconductors like GaAs, no special means (e.g. indium interdiffusion etc.) of avoiding or reducing a Schottky barrier on the back contact to the sample holder are necessary.

4.4   The InAs(110) surface

The (110) surface is a non-polar, natural cleavage plane of III-V crystals. Figure 4.5(a,b) give a schematic top view and side view of the surface. The surface features zig-zag lines of alternating In and As atoms in $[1\bar{1}0]$-direction. Regarding the electronic configuration at the (110) surface one can assume the broken hybrid bonds at the surface are half-filled. These states would reside at level with the sp^3 states of the free atoms and create a surface state within the band-gap. The clean InAs (110) surface was found not to exhibit such a state in the band gap. Instead, an indium dangling-bond state about 1 V and an indium surface state 1.5 V above the conduction band minimum have been predicted by DFT-calculations[88] and found in STS measurements[57]. Two separate mechanisms lead to this. First, there is charge transfer from higher-energy states to lower energy states, and as a consequence, the surface relaxes to further reduce the energy level of the filled states while increasing the energy level of the empty states (Jahn-Teller-Effect). This relaxation includes a displacement of the surface As atoms 70 pm outwards into the vacuum. And second, as a consequence of this, the energetically favorable dangling bond state on the arsenic atom is filled completely while the unfavorable state of the indium atom is unoccupied[57; 88]. Hence, the surface does not feature states within the band gap and remains uncharged. As a result, without an externally applied electrical field there is no band bending at the surface.

Figure 4.5(c) shows a constant-current topograph of our sample. During scanning the bias voltage was increased from 1 V to 2.8 V in steps of 0.2 V. Due to tip-induced band-bending, the difference between the Fermi energies of tip and sample are not equivalent to the applied bias voltage (see Figure 3.9).

The actual position of the tip Fermi energy with respect to the valence band maximum was calculated based on the given band bending conditions (Chapter 5). These values are given in parentheses below the applied bias values.

As guide to the eye, thin black lines indicate the positions of the maxima at 1 V. Up until 1.6 V, the red maxima of the protruding rows are aligned with these lines. There are two main indications for the fact that at bias voltages between 1.0 V and 1.6 V, only the As-atoms in the surface are imaged. First, as mentioned above, the rows of arsenic atoms actually protrude from the surface higher than the indium atoms. In addition to that, DFT calculations show that the majority of the density of states is localized on the As atoms for energies below the indium state which is about 1.3 eV —1.6 eV above the valence band maximum[88]. Due to tip-induced band bending, this energy range corresponds to a bias voltage range of 1.4 V to 1.8 V.

Indeed, in the range of the In surface state at bias voltages of 1.4 V to 1.8 V, the contrast in the constant-current images (Figure 4.5) shifts by half a surface unit cell in $[1\bar{1}0]$ direction and is thus aligned with the In rows. For increasing bias voltages the contrast declines, partly due to a more balanced contribution of In and As states, but also due to an increasing tip-sample distance. The details of these contrast changes are investigated thoroughly in [56]. For the purpose of

this work, the observation serves as a confirmation that up to voltages of about 1.4 V, As atoms provide the dominating contrast of the host lattice. This fact will be useful in the following section.

The top graph of Figure 4.6 shows an STS spectrum taken on the Mn-doped InAs sample, but away from any dopants. The bottom curve shows the same spectrum normalized by dividing by I/U. In the normalized representation, the band-gap of 0.42 eV is clearly visible. According to the p-type doping, the Fermi energy is located at the valence band maximum. The indium surface state appears as an increasing signal at about 1.75 V applied bias, corresponding to an energy of 1.6 eV above the valence band maximum. The peak at the conduction band minimum most likely is related to distant Mn dopants, as explained in Chapter 5.
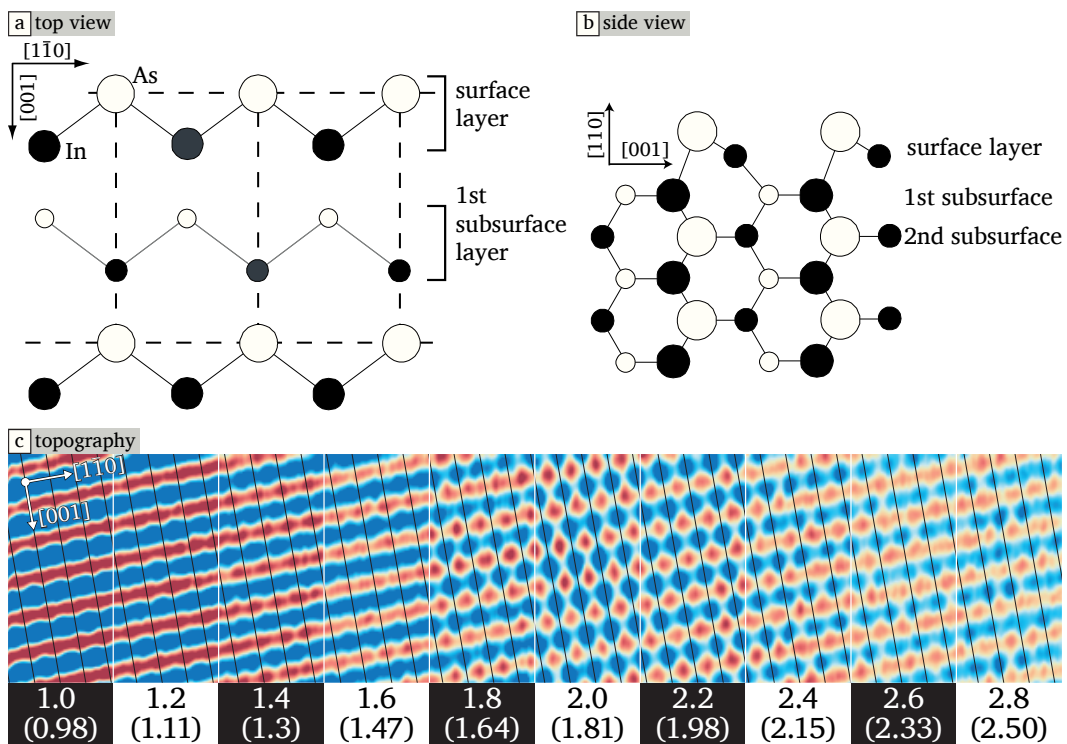
Figure 4.5: **Crystal structure at the** (110) **surface and imaging of each atomic sublattice with the STM. (a), (b):** Crystal structure of the InAs(110) surface ((a): top view, (b) side view). **(c):** Bias voltage dependent contrast in the (110)-surface of p-doped InAs. The top row of values indicate the applied bias. Up to about 1.6 V, only the As-rows are imaged. Their positions are indicated by thin black lines in (001) direction. Starting at about 1.6 V, the contrast shifts towards the indium-rows. At very high voltages, the contrast declines. The values in brackets give the calculated energy with respect to the valence band maximum when tip-induced band bending is taken into account (see Chapter 3.2 and 5). ($U_b = 1$ V —2.8 V, $I_{set} = 10$ nA, $n = 5 \times 10^{18}$ cm^{-3})
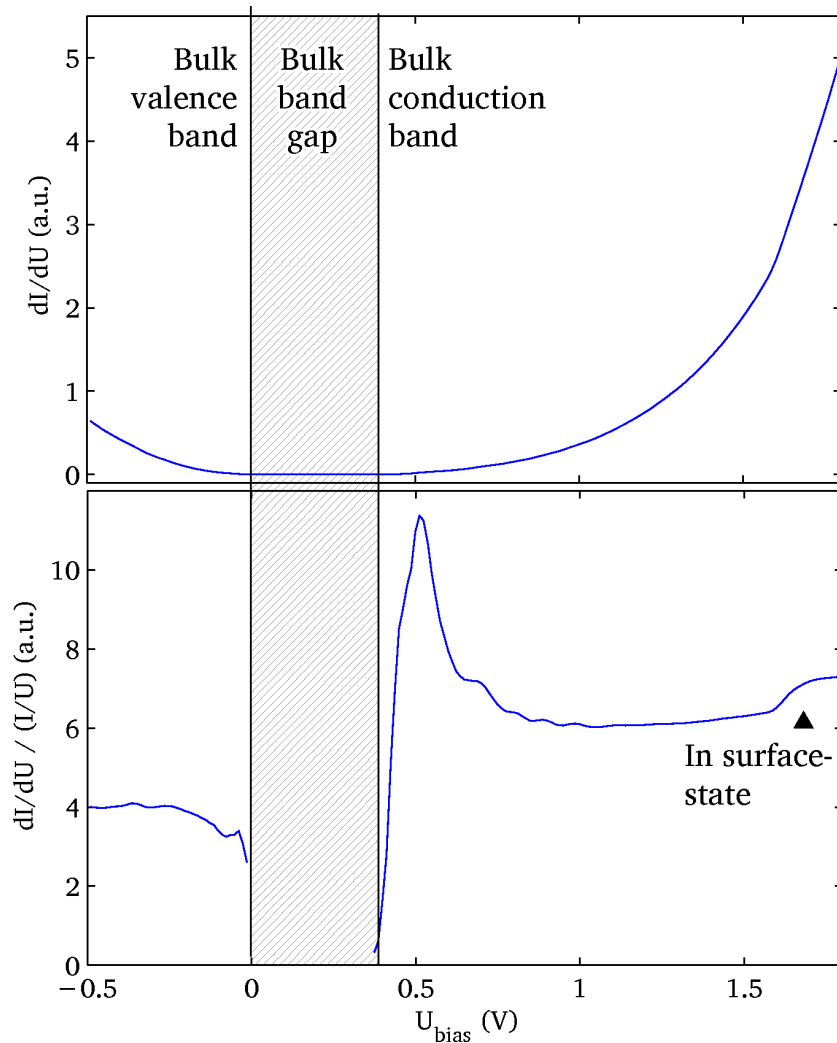
Figure 4.6: **STS spectroscopy curve on Mn-free area of Mn-doped InAs. Top:** Direct dI/dU-spectrum measured with lock-in technique. **Bottom:** Normalized dI/dU-spectrum. Here, the band-gap of $0.42\,\text{eV}$ is very eminent, as well as the fact that the sample bulk Fermi energy ($0\,\text{V}$) is located at the valence band maximum. ($U_{\text{stab}} = 2\,\text{V}$, $I_{\text{stab}} = 2\,\text{nA}$, $U_{\text{mod}} = 20\,\text{mV}$)

4.5 Determining the dopant depth below the (110) surface

While STM can resolve structure at the sample surface with remarkable precision, the depth of defects below a surface on the other hand usually has to be determined through indirect means, if possible. Luckily, with this particular sample system there is solid experimental evidence to infer this information from our measurements.

Typical STM-topographs of both the lower-doped ($3.8 \times 10^{16}\,\text{cm}^{-3}$, taken at negative bias) as well as the highly-doped ($5 \times 10^{18}\,\text{cm}^{-3}$, taken at moderate pos-
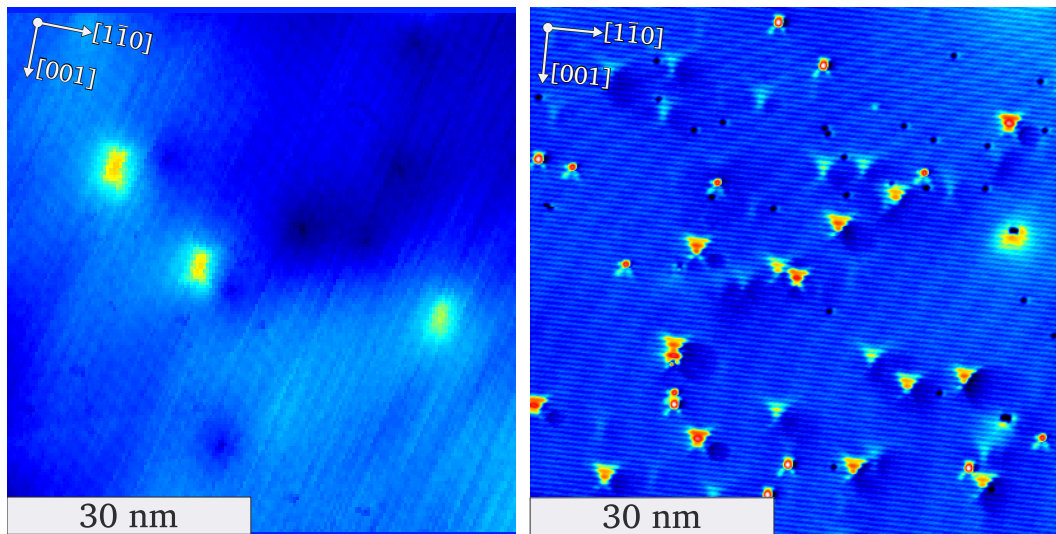
Figure 4.7: STM topograph of the cleaved (110)-surface of Mn-doped InAs. Left: $3.8 \times 10^{16}\,\mathrm{cm}^{-3}$ ($U_\mathrm{b} = -1.1\,\mathrm{V}$, $I_\mathrm{set} = 0.2\,\mathrm{nA}$). Right: $5 \times 10^{18}\,\mathrm{cm}^{-3}$ ($U_\mathrm{b} = 1\,\mathrm{V}$, $I_\mathrm{set} = 0.5\,\mathrm{nA}$). Manganese dopants in the surface are visible as protrusions. The different doping levels are obvious. In the image on the right, the As-atoms of the host lattice are visible as a regular pattern of lines.

itive bias $\sim 1\,\mathrm{V}$) sample are shown in Figure 4.7. In the positive bias image, the atomic lattice of the arsenic atoms in the surface can be seen clearly across the whole image as regular lines along the $[1\bar{1}0]$ direction. In both images, the most prominent localized features are protrusions, box-like in the negative bias image and triangular or bow-tie-shaped in the positive bias image. Both are caused by Mn acceptors below the surface. Other defects show up as small depressions. Chapter 6 is dedicated to the actual shape of the observed anisotropic Mn features at positive voltages and their interpretation as direct images of the highly anisotropic charge density of the bound-hole wave function.

We do not however find a whole range of features but a limited set of shapes that appear repeatedly all over the surface. At this point we can already assume that we are observing manganese acceptors in different depths.

Figure 4.8(a) shows line sections in $[1\bar{1}0]$-direction across a number of different Mn features and also gives their respective height. The diamond shaped markers indicate the positions of the As-protrusions at the surface. This demonstrates another important property of these shapes (also indicated by the diamond markers): they are either centered right on an As-protrusion or between two of them. Figure 4.8(b) shows the apparent heights of the features in decreasing order as found in seven comparable STM topographs at a bias voltage of 1 V. The type of marker indicates the alignment with respect to the As-rows.

If we assume that the apparent height of the Mn feature decreases monotonically with increasing depth, we notice that when looking at the features in this order, their alignment with the host As-rows alternates in a regular fashion. As illustrated in Figure 4.8(c), Mn occupies In sites and so the topographic feature
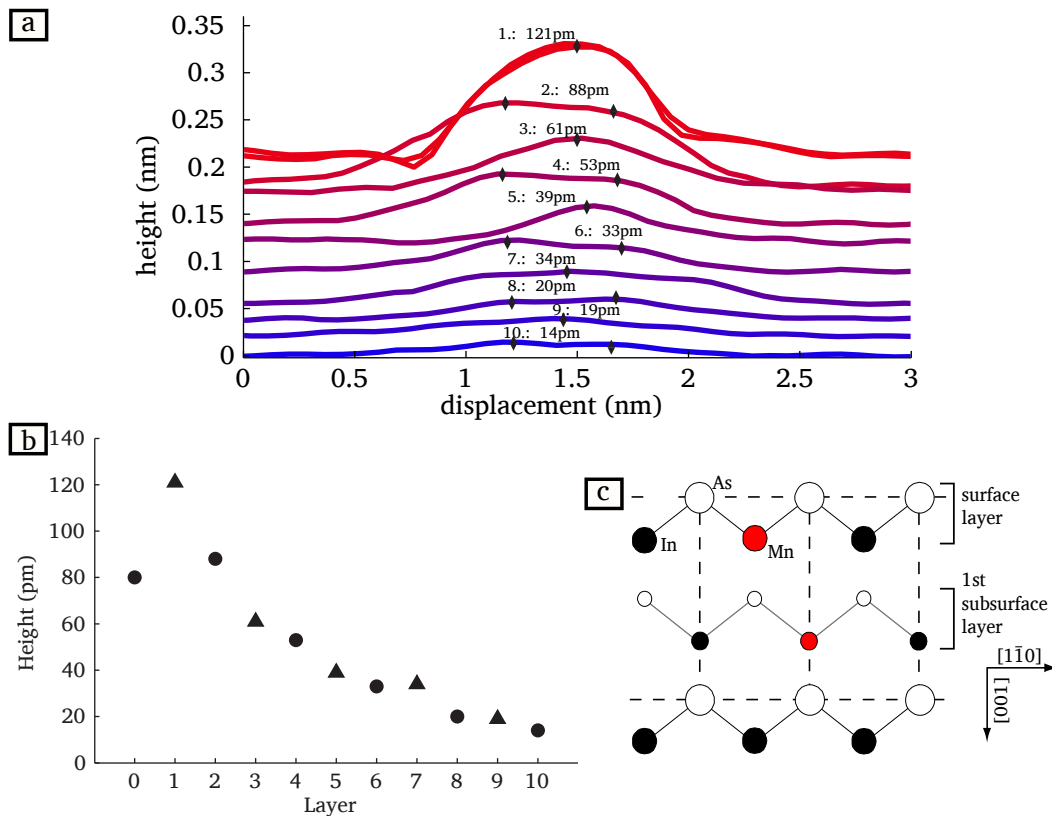
Figure 4.8: **Determining the depth of manganese acceptors using topographic height and symmetry. (a):** Line sections across Mn features in $[1\bar{1}0]$-direction. Markers point out As protrusions of the host lattice. The apparent height relative to the As-lattice is given in picometers. **(b):** Topographic height of Mn features at $U_b = 1\,\mathrm{V}$ and alignment with surface As-rows. The marker type indicates the features alignment with the surface pattern (dot: between two As-rows, triangle: aligned with As-rows). **(c):** Structure of the InAs(110) surface and Mn position. Mn acceptors in even layers (surface, 2nd., 4th. etc.) lie between surface As atoms, while those in odd layers appear aligned.

has to be either centered in between two rows — if the acceptor is in the surface layer, second layer, etc. — or centered on the $[001]$-As-rows if it is in the first, third etc. layer. This is the alternation that we observe. With this resolution of the layer parity, remaining ambiguities in the apparent height can be removed, and the absolute depth of acceptors can be determined[33], as shown in Figure 4.8(b).

Following this procedure we find a small anomaly for the surface layer acceptor. Although it has the right alignment with the As-rows it does not appear higher but instead more shallow than acceptors one layer below. Also, its shape is distinctly different from the deeper ones (see Section 6.1.1). With the combined evidence from the series of deeper acceptors and the correct alignment in the As-rows we can safely assume that it is in fact the surface layer substitutional Mn, even though it does not fit perfectly into the sequence. An almost identical feature was found for manganese atoms manipulated into the surface layer[54; 94].
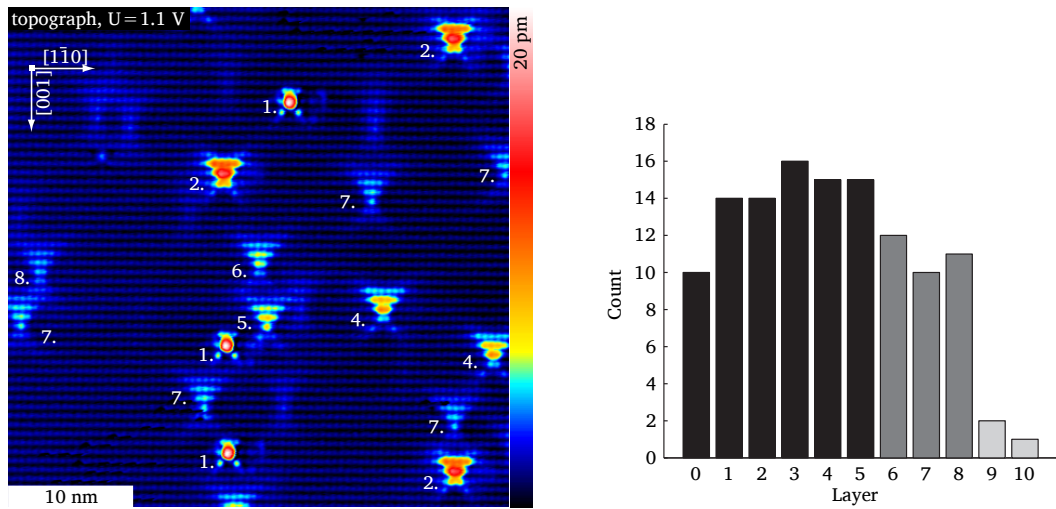
Figure 4.9: **Determination of acceptor depth and depth statistics. Left:** Mn dopants with their depth below the surface marked. The depth was determined from the apparent height and the alignment with surface As-rows (see text). ($U_b = 1.1\,V$, $I_{set} = 0.5\,nA$, $n \approx 5 \times 10^{18}\,cm^{-3}$). **Right:** Frequency of Mn dopants in different depths summed over a set of comparable STM images.

The depth of each dopant determined this way is given in Figure 4.9 (left). Note that the numbering counts sub-surface layers and thus starts at zero for an acceptor in the surface layer. The absolute depth of the dopant below the surface can be determined up to the eighth layer in most cases. Acceptors deeper than eight to ten layers — depending on image quality — are still clearly visible, but their depth cannot be determined without ambiguity, and we therefore omit the numbering in Figure 4.9 for those dopants.

A rough statistical analysis, given in Figure 4.9(right), of the numbers of acceptors in different depths from several images shows that they all appear with almost equal frequencies, as would be expected[†].

Once the depth of dopants can be determined, we can count all the dopants in a certain volume (that is, up to a certain depth) and determine their average volume density in that area. This analysis was performed for a number of images to reduce the statistical error. In all of the images investigated, a total number of 1131 dopants was found within a volume $20.3 \times 10^{-17}\,cm^3$, yielding an average doping density of $5.6 \times 10^{18}\,cm^{-3}$.

This value fits very well with the charge carrier density of $5 \times 10^{18}\,cm^{-3}$ and the value from the Brillouin function fit of $4.84 \times 10^{18}\,cm^{-3}$, as shown in Table 4.2. This close match of the Mn density obtained from magnetic and STM measurements with the carrier density indicates that the vast majority of Mn dopants is incorporated substitutional on indium sites. For the rest of this study we will assume that our samples had a density of substitutional Mn dopants of about $5 \times 10^{18}\,cm^{-3}$.

[†]with the exception of very deep ones (>9 layers), which are increasingly harder to identify.

Method	Mn Density
Transport measurement	5×10^{18} cm^{-3}
Magnetization measurement	4.84×10^{18} cm^{-3}
STM statistics	5.6×10^{18} cm^{-3}

Table 4.2: Manganese doping density, as determined with different methods.

Chapter 5

Switching the charge of single Mn acceptors

This chapter covers our observation of different charge states of manganese acceptors and their switching behavior. In the vicinity of manganese acceptors observed with STM/STS, tip induced charge switching of the manganese acceptor creates ring-like structures in $\mathrm{d}I/\mathrm{d}U$ maps. Using a simple model of the band bending at the semiconductor resulting from the electric field produced by the tunnel junction, we demonstrate that this charging effect can be described by population/depopulation of carriers resulting from pushing the acceptor state below/above the Fermi level[68].

Often, band-bending effects (Chapter 3.2) are an undesirable phenomenon in STM and other electronic measurements. Its occurrence complicates the measurement and interpretation of spectroscopic data, not to mention it affects accurate delineation of semiconductor heterostructure junctions. The fact that band bending effectively shifts energy scales even affects topographic measurements since the applied bias can no longer be directly related to the energy of the contributing states with regard to the sample's Fermi energy. Here we describe how this otherwise undesirable effect can be utilized to gain insight about single dopants buried within the semiconductor host which cannot otherwise be accessed with conventional STM techniques. Namely the binding energy of individual dopants as well as their spatially resolved Coulomb interaction and screening behavior can be measured. We demonstrate that the bow tie shaped topography of the manganese acceptor described in Chapter 4 is in fact a spatial visualization of the charge density of the bound hole. Furthermore, the onset voltage necessary for switching the acceptor provides us with an additional way of determining the exact tip work function, which is a crucial ingredient for interpreting STS spectra of semiconductors.
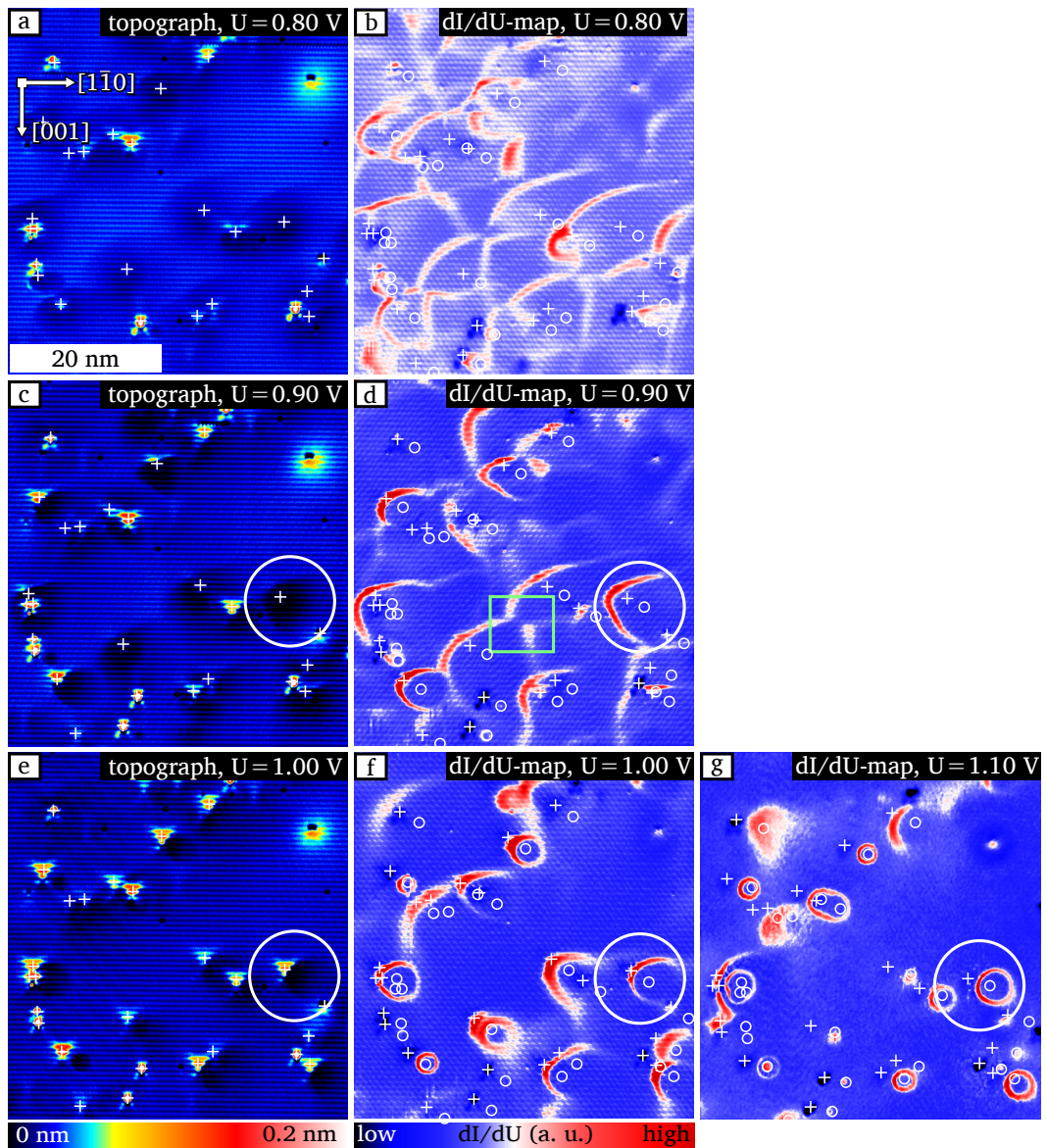
Figure 5.1: Evolution of the ring-like feature in topographs and dI/dU**-maps over voltage. (a,c,e):** STM-topographs obtained at U_b as indicated, $I_{set} = 0.5\,\text{nA}$, $n \approx 5 \times 10^{18}\,\text{cm}^{-3}$. **(b,d,f,g):** dI/dU maps of same area with increasing U_b ($U_{mod} = 10\,\text{mV}$). The center of the evolving feature (small white circles) is slightly shifted away from the dopants' positions (white crosses). This can for example be seen in the evolution of the ring from one dopant, marked by the large white circles in (d,f,g). In (d), note the "anti-crossing" marked by a green square.

5.1 Appearance of Mn acceptors in topography and spectroscopy

## 5.1.1 Rings in topography and dI/dU maps

Figures 5.1(a,c,e) show STM topographs which were all acquired from the same sample area at increasing bias voltages. The positions of the manganese acceptors are marked by white crosses. A comparison of the three images reveals that some of the manganese acceptors are visible (Figure 5.1(e)) between $U_b = 1.0\,\mathrm{V}$ and $1.1\,\mathrm{V}$ but not below $U_b = 0.9\,\mathrm{V}$ (Figure 5.1(a) and (c)). Instead, a faint larger scale depression is observed around or close to those acceptors. This depression becomes smaller at higher bias voltage and the previously invisible bow tie like protrusion described in Chapter 4 appears (also compare white circles in Figures 5.1(c) and (e)). At even higher bias voltages the depression in STM topographs completely vanishes, leaving behind just the bow tie. This bias dependency of such a large scale feature suggests that this effect is purely electronic in origin and not, for example, an actual topographic feature.

Figures 5.1(b,d,f,g) illustrate subsequent constant current dI/dU maps acquired simultaneously during topographic imaging with increasing bias voltage. The images show zones of enhanced differential conductance (in red) on a background of lower signal (blue). Corresponding to the depression in topographs, an arc or ring-like feature of increased differential conductance can be found around each manganese acceptor which coincides with the sharp borders of the topographic depression. The feature appears as a faint extended arc like the one marked by the large white circle in Figure 5.1(d). With increasing voltage, the feature shrinks towards its central point (small white circles in (f,d,f,g)). Exactly when the ring crosses the position of the corresponding Mn acceptor, the bow-tie appears in topography (large circles in (c) and (e)). At even higher voltage, each arc eventually closes and forms a ring as marked by the circle in (g). This ring continues to shrink as the voltage is further increased and finally forms a bright spot slightly aside the location of the acceptor (small circles), before it vanishes completely.

This development of the ring shape is common among all acceptors. Particular rings evolve slightly different but all share a similar energy dependent development. Also there are indications that the acceptors interact when the rings overlap, like for example in the area marked by a square in Fig. 5.1(d).

To summarize the four most important observations:

▶ Each ring is related to a single manganese acceptor located near or at the center of the dopant.

▶ Above the voltage where the ring crosses the position of the corresponding manganese acceptor, the bow tie feature appears in topography.

▶ Each of the described ring-features develop in a similar fashion, although not exactly identical as they overlap and seem to interact.
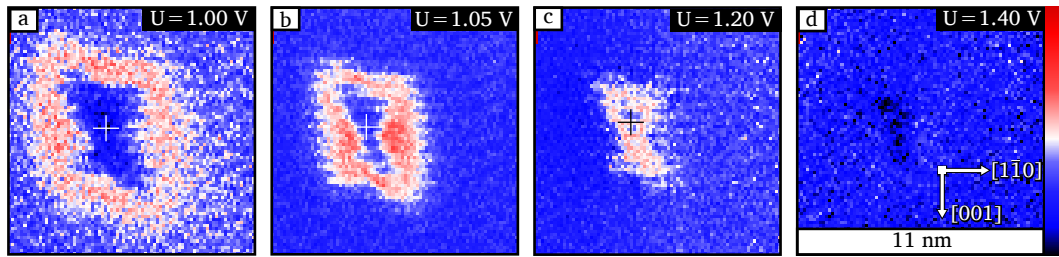
Figure 5.2: **Short range evolution of the ring like feature in a series of** dI/dU **slices** ($U_{\mathrm{stab}} = 1.5\,\mathrm{V}$, $I_{\mathrm{stab}} = 0.6\,\mathrm{nA}$, $U_{\mathrm{mod}} = 10\,\mathrm{mV}$, U_{b} as indicated) measured with a differently shaped tip than in Figure 5.1 on the lower doped sample $n \approx 3.8 \times 10^{16}\,\mathrm{cm}^{-3}$.

> ▶ The bias voltage at which the ring disappears depends on the depth and the local environment of the acceptor. This happens within 0.3 V of $U_{\mathrm{b}} = 1.0\,\mathrm{V}$.

Experiments with differently shaped tips or different tip materials show a variety of ring shapes. As an example, panels (a)-(d) of Figure 5.2 show dI/dU slices (see Section 3.1.7 on page 33) from an STS measurement of a single acceptor in the lower doped sample, using a different tip than in Figure 5.1. Due to the low Mn doping density, no interaction effects between dopants are observed in this case. With this particular tip, the dI/dU-ring appears to be perfectly centered around the position of the manganese acceptor (marked by a cross). The shape of the ring immediately before it collapses, as shown in Figure 5.2(b) and (c) resembles the bow-tie shape as seen in topography for a typical manganese acceptor near the surface (e.g. Figure 4.9). Finally, in (d) the ring has disappeared and only a small-scale depression about the size of the acceptor is left.

Section 5.2 and 5.3 are devoted to the origin of the ring feature, while the rest of this section focuses on the actual spectroscopic signature of the rings in local STS spectra taken in the vicinity of the manganese acceptor.

5.1.2   Local spectroscopy of manganese acceptors

Performing STS on the center of the topographic bow tie feature of an acceptor in the second layer yields a dI/dU spectrum like the red curve in Figure 5.3(a). The pronounced peak at ca. 0.85 V corresponds to the situation shown in Figure 5.2(c) and marked by the circle in Figure 5.1(e) and (f), where the dI/dU ring crosses the Mn position and the bow tie Mn feature emerges in topography. Spectra averaged over the ring at larger distances from the Mn center are also shown in Figure 5.3(a) (in blue, green, orange, etc.). The image on the right illustrates, where the spectra for each of the different curves were taken. For increasing ring diameter, the peak occurs at lower energy and drops in intensity. This peak in dI/dU spectra corresponds to the dI/dU signal forming the ring feature in dI/dU maps. Since the ring was rather asymmetric in these measurements, we can not assign a single radius to each peak but a range, corresponding to the varying radius within each ring, as can be seen in the orientation image.
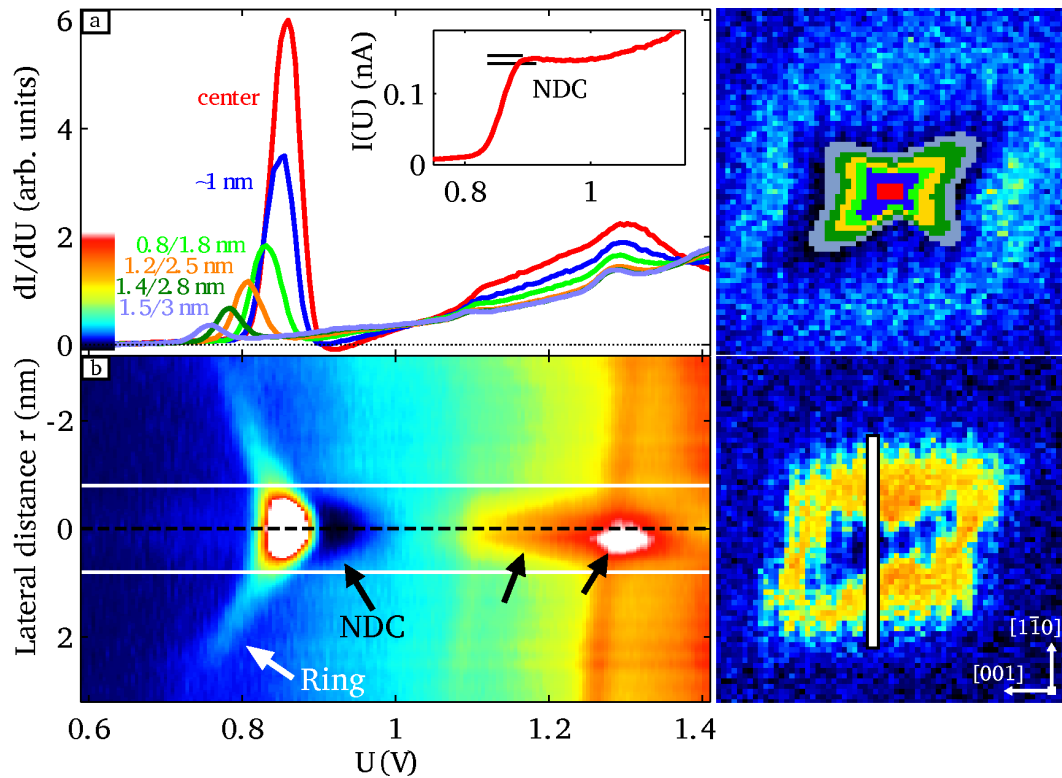
Figure 5.3: **Spectroscopic analysis of ring-feature.** **(a)** dI/dU spectra averaged over the ring feature for different ring diameters, as indicated. The orientation image on the right illustrates which spectra were used for each individual curve. Since the ring is not circular the numbers give the minimum and maximum distances to the manganese center. The small inset graph shows the $I(U)$ curve corresponding to the "center" dI/dU curve (red). **(b)** Color-coded dI/dU spectra measured in different lateral distances from the manganese center as indicated by the y-axis. The image on the right hand side indicates the position of the spatial axis of the plot. The mapping of energy to color is given by the color bar in (a). The two horizontal white lines and the dotted black line indicate the extension of the bow tie shape and its center in the topograph. The arc feature (white arrow) is equivalent to the ring feature in dI/dU maps. The localized nature of the observed negative differential conductance (black area), as well as of the follow-up peaks are visible (black arrows). ($U_{stab} = 2\,\text{V}$, $I_{stab} = 2\,\text{nA}$, $U_{mod} = 20\,\text{mV}$)
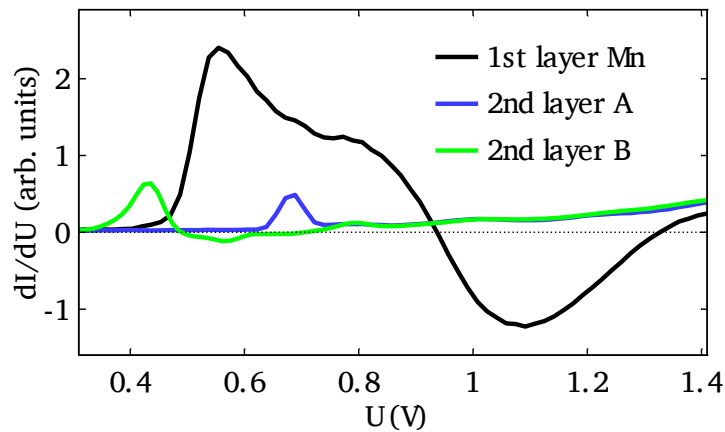
Figure 5.4: **Negative differential conductance in** dI/dU **spectrum of a manganese acceptor.** Shown are spectra taken on an acceptor one layer below the surface (black line) and on two different acceptors two layers below the surface. The first layer acceptor shows a much stronger peak and pronounced negative differential conductance, while the effect is almost not present for the second layer acceptors. ($U_{stab} = 1.8\,V$, $I_{stab} = 1\,nA$, $U_{mod} = 20\,mV$, $n = 5 \times 10^{18}\,cm^{-3}$)

Depending on the tip configuration, we sometimes observe negative differential conductance (NDC) as can be seen for example as the black area in Figure 5.3. This phenomenon can be found on acceptors close to the surface and is strongest on those one layer below the surface. It is much weaker for dopants in the second layer, as shown in Figure 5.4, and only hardly observable for those in the third layer.

We find the NDC at the center of the acceptor at voltages slightly above the main peak. This is visible in the central (red) dI/dU-curve on a second layer acceptor and as negative slope on its corresponding $I(U)$-curve shown in the inset of Figure 5.3(a). The origin of the NDC will be discussed in Section 5.2.

For some measurements we also observe follow-up peaks above the main peak, e.g. in Figure 5.3(a) at $1.1\,V$ and $1.3\,V$, which we relate to higher order states in Chapter 6. Also, the main peak often has a pronounced shoulder, like for example in the black curve in Figure 5.4, taken on a one layer deep dopant. This shoulder will be of significance for the interpretation of the ring features, since it implies that there are actually two peaks at similar energies but of different origin.

Figure 5.3(b) gives a different view of the same spectroscopic data set as in (a). The dI/dU intensity is color-coded, and the y-axis gives the real-space displacement along the line[*] through the center of the manganese acceptor, marked in the image to the right. The dotted horizontal line indicates the spectrum corresponding to the red curve in (a). The ring feature, which in Figure 5.3(a) took the form of a peak, now shows up as two "wings" (indicated by a white arrow) besides the main central peak, extending far out from the acceptor. In strong con-

---

[*]in $[1\bar{1}0]$ direction

trast to the extended ring feature the main peak and the follow-up peaks (black arrows) are strictly confined to a range of less than 1 nm from the center, i.e. few surface unit cells wide. Therefore, these local phenomena can be attributed to effects of the manganese acceptor LDOS which will be the topic of Chapter 6. There, we relate them to the manganese acceptor state and higher order states, as well as to effects of exchange interaction on host states.

While the local phenomena can be explained in terms of mapping local DOS, this can neither explain the negative differential conductance nor the ring features. To explain these features, we need to extend the discussion about the effects of tip induced band bending.

5.2   Charge switching in the band bending picture

As explained in Section 3.2, at least a rough understanding of the extent and amount of the band bending must exist prior to any solid interpretation of the STS spectra. The following sections are intended to establish sufficient understanding of the band bending phenomena, as well as the expected effects on the measurements. In the course of this, a simplified model is being developed, based on our understanding of the system. This model is then used to predict the dI/dU-rings and helps distinguishing separate phenomena we observe in our measurements.

5.2.1   The 1D case: STM tip vertically above the impurity

In a simplified approach the one-dimensional Poisson equation (Eq. 3.18) relating charge density to electrical potential can be solved self-consistently. It is given as Eq. 5.1 in a form that is convenient for semiconductors, where the space charge is composed of the occupation of the valence band (p, holes) and the conduction band (n, electrons), as well as charged donors (N_D^+) and acceptors (N_A^-). Note that to follow convention we use the symbol ϕ for the potential here, whereas otherwise it denotes the work function.

$$\nabla^2 \phi(z) = -\frac{e}{\epsilon \epsilon_0} \left(N_D^+(z) + p(z) - N_A^-(z) - n(z) \right) \tag{5.1}$$

The software that was used to solve the equation self-consistently is called IVCHAR and was developed by P. Koenraad[†] especially for the purpose of calculating charge distributions in semiconductors and tunnel currents in an STS measurement[‡]. The implemented geometry models the semiconductor sample, the vacuum gap and the tip. The semiconductor is characterized by its electron affinity E_A and band gap E_{gap}, the effective masses of the charge carriers, the

---

[†]then with IBM, now TU Eindhoven
[‡]The code was courteously provided by P. Koenraad (COBRA Inter-University Research Institute, Eindhoven University of Technology, The Netherlands), with additions by S. Loth and M. Wenderoth (IV. Physikalisches Institut der Universität Göttingen, Germany)

doping densities and dopant binding energies, surface state energies and densities. For the vacuum the dielectric constant and the gap width z are given. The tip is characterized through its work function Φ_{tip}. After solving Poisson's equation, it computes the total tunnel current incorporating contributions from different types of charge carriers including Γ-, X-, L-point electrons, heavy holes, light holes and 2D states. For our purposes we used the calculation of the charge distribution, the bias-dependent band profiles and the surface potential offset.

Figure 5.5(a) shows the result of the band bending calculation for the following parameters: tip work function $\Phi_{tip} = 4.5\,\mathrm{eV}$, electron affinity of the sample E_A $= 4.9\,\mathrm{eV}$, Mn acceptor energy $E_{acc} = 28\,\mathrm{meV}$ and -concentration $5 \times 10^{18}\,\mathrm{cm}^{-3}$, InAs band gap $E_{gap} = 0.41\,\mathrm{eV}$, and a tip-surface distance of $z = 6\,\text{Å}$. Φ_{bb} denotes the amount of band bending at the surface. At $0.8\,\mathrm{V}$ the offset is zero, since at this voltage the applied bias just compensates the work function difference. The slope of the curve here is about $1/5$. Below that point the curve approaches a slope of about $2/5$, while above it, the slope drops below $1/5$.

The calculated band profiles are shown in the panels of Figure 5.5(b) for three different bias voltages. In the following, A* denotes an acceptor level aligned with the Fermi energy. Note that the energy separation of the acceptor level with regard to the valence band has been slightly exaggerated in the pictures for clarity.

The underlying model implemented in the software for the solution of the Poisson equation assumes a 1D geometry, i.e. the tip is modeled as a half space above the sample and the vacuum gap. Therefore it can not provide the lateral extension of the space-charge region which will also depend crucially on the exact shape of the actual STM tip used in the experiment. This will be dealt with in section 5.2.2. However, already in this simplified model, we can clearly see that it is possible to change the charge state of the acceptor with the potential of the STM tip.

Charge switching

As mentioned before, it is possible to apply the right bias voltage with the STM, so that the bands in the sample become flat, i.e. there is no band bending at the surface. This voltage is referred to as U_{fb} (flat bands). To achieve this, the applied bias has to compensate the difference between the sample work function Φ_{semi} and the tip work function Φ_{tip} (Eq. 3.17 on page 34). If we assume that at low temperatures the sample Fermi energy lies between the valence band edge and the acceptor level E_{acc} and that the sample's electron affinity E_A is referenced to the conduction band edge, we find that

$$\Phi_{semi} = E_{gap} + E_A - E_{acc}/2 \qquad (5.2)$$

and finally

$$U_{fb} = (\Phi_{semi} - \Phi_{tip})/e = \left(E_{gap} + E_A - E_{acc}/2 - \Phi_{tip}\right)/e = 0.8\,\mathrm{V} \qquad (5.3)$$
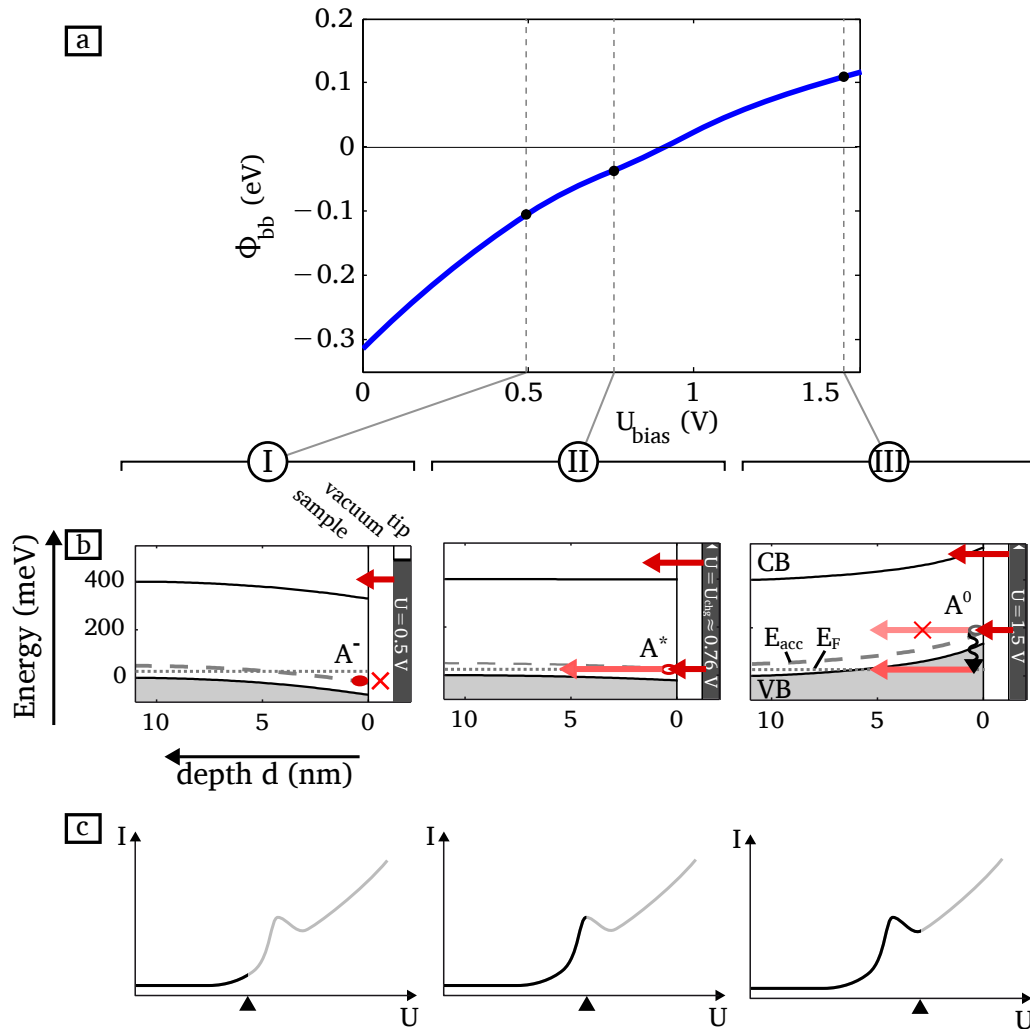
Figure 5.5: **Band bending below the STM tip for different bias voltages.** **(a):** Calculated tip-induced band bending at the sample surface. The curve shows the dependence of the potential offset at the sample surface caused by the work function difference and the applied bias voltage. **(b):** depth-dependent band bending of valence band (VB), conduction band (CB), and acceptor level (E_{acc}) towards the surface below the STM tip position. The energy of the acceptor level with regard to the VB is exaggerated for clarity. Shown are numerical solutions of the one-dimensional Poisson equation. The dotted line indicates the bulk Fermi energy (E_F). **(c):** Development of current signal with bias voltage. When the acceptor level is aligned with the Fermi energy, it becomes available for tunneling and contributes to the current. At higher voltages, the increasing band bending lifts the level into the band gap where its ability to conduct electrons is diminished. The acceptor's contribution to the current is canceled again. Charged (neutral) acceptors are indicated with A^- (A^0). A^* denotes an acceptor that is aligned with the Fermi energy.

At a bias voltage $U_b = U_{chg}$ slightly below U_{fb}, shown in the middle panels of Figure 5.5 (section **II**), an acceptor right below the STM tip (red ellipse, A*) is aligned both with the bulk Fermi level E_F and the DOS provided by the impurity band/valence band edge. This leaves an open tunnel path for electrons from the tip via the acceptor into the bulk of the sample along E_F (see arrows). This will cause a peak in dI/dU-curves at U_{chg} above the acceptors as found in the experiments. At the same time, the occupied tip DOS is already overlapping with the conduction band, which gives its own contribution to the tunnel current (upper arrow).

For $U_b < U_{chg}$ (section **I**), the negatively charged acceptors A$^-$ make up the screening charge density (left panel of Figure 5.5(b)). Their low density leads to an extended and smooth bending of the DOS bands, reaching $\approx 10\,\mathrm{nm}$ into the sample for $U_b = 0.5\,\mathrm{V}$. In this space charge region E_F lies in the band gap above the impurity band, or even in the (bent-down) conduction band if $U_b < -0.3\,\mathrm{V}$. The only conductance is provided by the bulk bands, either from occupied tip states to the conduction band or ($U_b < 0\,\mathrm{V}$) from valence band states to unoccupied tip states.

Negative differential conductance

For $U_b > U_{chg}$ (section **III** of Figure 5.5(b)) the acceptor level is raised out of resonance, above E_F. For an electron/hole to move via a surface acceptor to the back contact of the sample, it needs to lose energy, e.g. to a phonon, to enter the valence band. At low temperatures, this process might be inhibited due a reduced phonon density of states. Consequently, the conductance path created by emptying the acceptor at U_{chg} should be suppressed at higher bias voltages.

The opening of an additional tunnel path via the acceptor, with increasing energy, will result a sudden increase in the tunnel current (peak in dI/dU). The suppression of the same channel immediately following its creation will lead to a steep fall in the current. Therefore we expect a step up immediately followed by a step down, essentially a peak, in $I(U)$, and accordingly the peak in dI/dU corresponding to the current increase is followed by a dip with negative dI/dU due to the current decrease.

This matches the measurements showing a peak and NDC, obtained at the center of surface-near manganese acceptors as shown in Figure 5.3(a) and Figure 5.4. Since the described process involves directly tunneling into the (localized) acceptor state, it will be confined to a small surface area where this state significantly overlaps with tip states. The confinement of the strong peak/NDC structure to roughly $1.5\,\mathrm{nm}$ to $2\,\mathrm{nm}$ matches the size of the acceptor wave-function charge density as obtained from a tight-binding model (see Chapter 6). Since two effects are combined here, tunneling via the (p-like) acceptor state and tunneling into the (s-like) conduction band onset, a preference of the tip for certain states (s-like, p-like) might sufficiently explain why NDC is not observed with all tips.

### 5.2.2 The 2D case: Lateral distance between tip and impurity

In order to explain the rather long-range phenomenon of the dI/dU-rings in Figure 5.1 and Figure 5.3, a more detailed model is needed, which accounts for the lateral characteristics. This model has to include the geometry of the relative positions of tip, sample surface and embedded acceptor. As is obvious from their long range nature the observed ring structure in dI/dU maps cannot be explained by the presence of the localized acceptor wave function. The dI/dU peak forming the ring-feature is observed much further away from the Mn center (up to 20 nm) than the Mn acceptor wave function extends (see Figure 5.3). The source of this distance-dependent peak becomes apparent when the effect of the lateral shape of the tip induced potential on the acceptor's charge switching is taken into account.

The panels of Figure 5.6 show a sketch of the lateral profile of the band bending as a function of the distance r from the base of the center of the tip. With a bias voltage of U_{chg} only acceptors directly below the tip are aligned with E_F. In this situation, shown in the center panel, an acceptor that is laterally some distance apart from the tip will have its acceptor state slightly above E_F and therefore uncharged (grey ellipse in middle right panel, A^0). At $U_b < U_{chg}$ (left panel) the band bending right below the tip moves the ground state of an acceptor below the Fermi energy. However, the downwards band bending will cause the acceptor level to cross E_F in some lateral distance $\vec{r}$ from the tip (A^*), since the screening potential in the sample decays laterally.

As the voltage is lowered, the downwards band bending becomes stronger and the crossing-radius expands. An acceptor outside of this radius is above E_F and uncharged (A^0) while inside the radius it lies below E_F and thus is in the charged configuration (A^-). From the point of view of an isolated acceptor there is a radius inside which the STM tip lowers the local potential sufficiently to switch it into the charged state. If the tip is outside of this radius the acceptor is neutral. If in an STS measurement the voltage ramp causes the switching radius to extend across this acceptor it will become charged resulting in a peak in dI/dU, as will be reflected in a model below. In other words, the rings observed in Figure 5.1 and 5.2 are caused by the switching of a charge a few nanometers away from the tip base point.

5.3 Numerical model

In order to prove that the interpretation presented above can explain the observations within the framework of existing models of the tunnel process, a simplistic model was developed. The model demonstrates that the ring feature can be explained without including the acceptor state and exclusively by the effect of a charge change on the host conduction band DOS. The following section describes this simple model and explores its capability to cover the observed effects of charging on the dI/dU spectra.
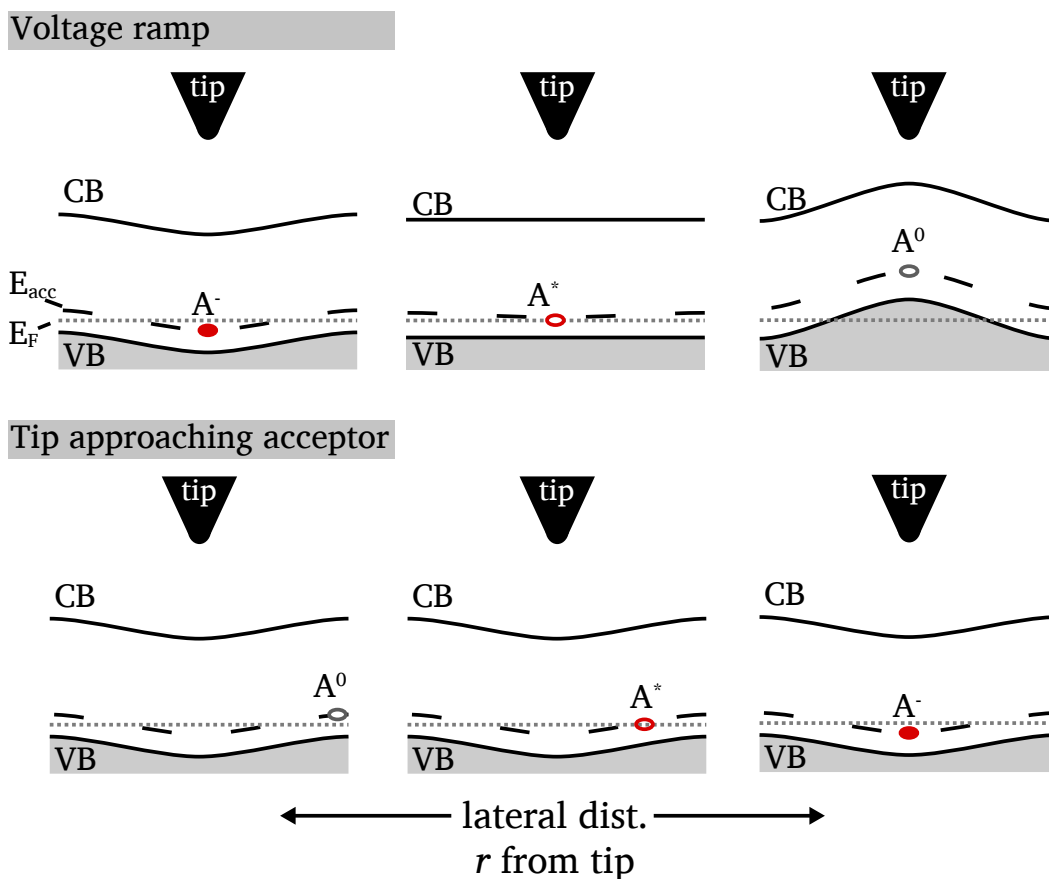
Figure 5.6: Schematic lateral run of the sample energy bands below the STM tip during a voltage ramp and during scanning. Top, Voltage ramp: (from left to right) Below peak voltage an acceptor right below the tip is charged (A$^-$). At peak voltage an acceptor below the tip is depopulated and starts to be conductive (A*). At higher bias voltages the unoccupied acceptor level (A^0) is lifted into the sample's band gap, reducing its conductance. **Bottom, Tip approaching acceptor with U_b below peak voltage:** At this bias voltage the STM tip causes downwards band-bending but due to the decay of the tip-induced potential, distant acceptors still lie above the Fermi energy. At a certain voltage-dependent distance an acceptor can be aligned with the Fermi energy. Right underneath the STM tip the downwards band-bending pushes the acceptor level below the Fermi energy.

5.3.1 Assumptions and approximations

When charging the acceptor, the abrupt change in the local potential has an effect on an extended surrounding of the acceptor that fades with distance due to the decay of its screened Coulomb potential. In other words, the acceptor contributes an additional, spatially varying offset potential $\phi_{\text{charge}}(r, U_b)$ to its environment, corresponding to its charge state and in so far dependent on the bias voltage U_b of the sample with regard to the tip. In the voltage range that is of interest, which is essentially the band gap region and above, a limited set of tunnel paths need to be considered. In this voltage range (about $0.4\,\text{V}$ to $1.5\,\text{V}$), only conduction band states are involved in the tunnel process, as long as tip states are not directly overlapping with an acceptor state. Tunneling into or out of the acceptor state is not included, according to the intention of the model, but will be discussed in detail in Chapter 6.

Going from lower voltages upwards in a spectroscopic measurement with fixed tip, or equivalently, entering the switching radius of an acceptor at a fixed bias voltage, the local potential will abruptly shift downwards as the acceptor goes from A^- to A^0. We interpret the effect of this potential change on the tunnel current with the Tersoff-Hamann model[103] (Section 3.1.5).

Knowing ϕ_{bb} from the calculation (see Section 3.2), we can insert it into Eq. 3.14 and can account for the tip induced band bending in the Tersoff-Hamann model by adding this bias-dependent potential as an additional offset to $\epsilon + \phi_{\text{bb}}(U_b)$ in the argument of the sample LDOS ρ_S (rigid band model):

$$I \propto \int_0^\infty \rho_t(\epsilon - eU)\rho_s\big(\epsilon + \phi_{\text{bb}}(U, x, y)\big)T(\epsilon, eU, z) \quad d\epsilon \tag{5.4}$$

For our model, we assume a constant tip density of states and a spherical parabolic conduction band:

$$\vec{r} = \begin{pmatrix} x \\ y \\ z \end{pmatrix}$$

$$I(U, \vec{r}) = \int_{E_F}^{E_F + eU} \rho_S(\epsilon + \phi_{\text{bb}}(U_b, x, y))T(\epsilon, U, z)\, d\epsilon \tag{5.5}$$

$$\rho_S(E) = \begin{cases} \sqrt{E - E_{\text{CB}}} & \text{for } E > E_{\text{CB}} \\ 0 & \text{for } E <= E_{\text{CB}} \end{cases} \tag{5.6}$$

$$T(\epsilon, eU, z) = \exp\left(-2z \cdot \sqrt{\frac{2m}{\hbar^2}\left(\bar{\Phi} + eU/2 - \epsilon\right)}\right) \tag{5.7}$$

$$\bar{\Phi} = (\Phi_{\text{tip}} + \Phi_{\text{semi}})/2 \tag{5.8}$$
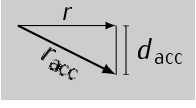
We further assume that the tip causes a bias voltage dependent band bending $\phi_{bb}(U_b, r)$ as simulated by the aforementioned Poisson solver, which decays laterally with r as detailed in[32]. The used decay functions for two different tip diameters are shown in the inset graphs in Fig. 5.7(b) and (c). We then assume the acceptor's localized charge in a given total distance $r_{acc} = \sqrt{r^2 + d_{acc}^2}$ (d_{acc}: acceptor's depth below surface) from the tip base point to switch if $\phi_{bb}(U, r_{acc}) = -E_{acc}/2 = 14\,\text{mV}$, i.e., when the local band-bending aligns the acceptor state with E_F. For numerical stability and as a crude simulation of thermal and other broadening effects, we simulate the switching as a soft transition broadened by $1\,\text{meV}$. We assume the potential of the localized charge to decay like[26]

$$\phi_{charge}(r_{acc}) = \frac{e}{4\pi\epsilon\epsilon_0 r_{acc}} e^{-r_{acc}/r_{screen}} \tag{5.9}$$

with $\epsilon = 14.6$, a screening length r_{screen} which is used as free parameter and a depth of the acceptor of $d_{acc} = 2\,\text{ML} = 0.43\,\text{nm}$.

The implementation of this model in MATLAB can be found in Appendix A.

5.3.2 Simulation results

Using the model we can now calculate $I(U)$ and dI/dU-curves for an acceptor in a certain depth and for different lateral tip-acceptor distances. A resulting $I(U)$ curve, as well as derived dI/dU curves, are given in Fig. 5.7(a). Above the switching point, the sample's LDOS in the current integral gets shifted down in energy, yielding a higher current than below the switching point. This step up in current, or peak in dI/dU, matches observations like in Figure 5.3. Since this is no separate acceptor related tunneling mechanism, but solely an effect of the interaction between the tip potential, the acceptor charge and the LDOS below the tip, the extended range of the effect is plausible.

Using the screening length r_{screen}, the tip work-function Φ_{tip} and the extension of the tip potential D_{FWHM} as the only free parameters the best agreement with the data shown in Figure 5.3 can be achieved for $r_{screen} = 10\,\text{nm}$, $\Phi_{tip} = 4.38\,\text{eV}$ (theoretically $4.5\,\text{eV}$) and $D_{FWHM} = 5\,\text{nm}$ to $10\,\text{nm}$.

The model closely reproduces the observed properties of the dI/dU peaks. The shifting to lower energies and the reduced intensity we find with increasing distance from the acceptor are reproduced (compare Figure 5.3(a) and Figure 5.7(a)), as is the arc-like appearance in the "waterfall" plot (Figure 5.3(b) and Figure 5.7(b,c)).

A notable difference between experimental and simulated results are found around $r = 0\,\text{nm}$: the negative differential conductance, as well as a brighter central peak and the follow up peaks are missing in the simulation. As stated in Section 5.2.1, the localized peak/NDC structure and the follow up peaks are attributed to direct tunneling via the localized acceptor LDOS which is intentionally not included in the model and will be a subject of Chapter 6.
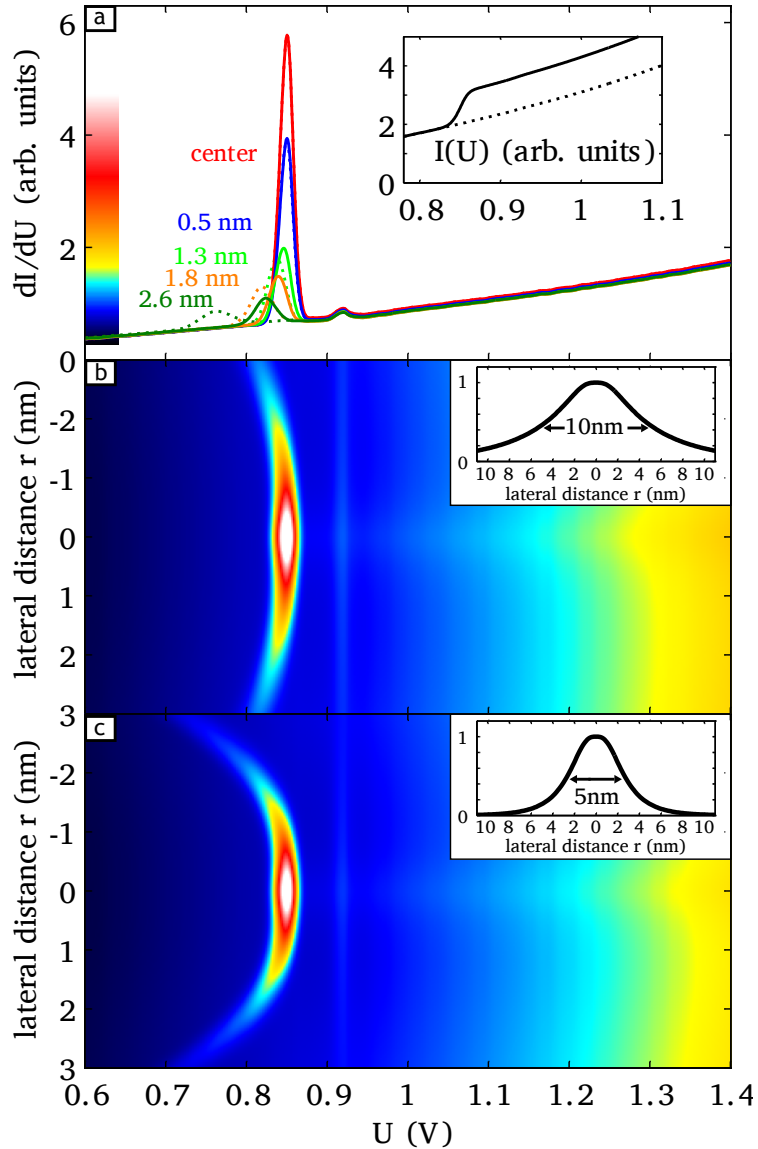
Figure 5.7: **Model of the charge-switching effect in** dI/dU **spectra.** **(a)** Simulated dI/dU spectra in presence of a switchable charge calculated for two different tip-potential diameters ($D_{FWHM} = 10$ nm: solid line; $D_{FWHM} = 5$ nm: dashed line) and tip-acceptor distances as indicated. Inset: Simulated current vs. voltage for central spectrum. Dotted line shows current without influence of a charge. **(b) and (c)** show color coded spectra calculated at different lateral distances r from the charge center for the wider tip (10 nm) and for the narrower tip (5 nm), respectively. The insets show the lateral profile of the tip potential within the sample.

5.4   What do charging rings tell about the tip and the acceptors?

The bias voltage U_{chg} at which the acceptor is charged is theoretically determined from material properties like the acceptor binding energy E_{acc}, the electron affinity E_A and the tip work function Φ_{tip} (see Eq. 5.3).

However, there are several uncertainties:

▶ The geometry and composition of the tip apex can vary the tip work function by up to one electron volt[74].

▶ Local variations of the doping introduce inhomogeneities of the charge density, which will cause lateral fluctuations in the electron affinity E_A. This effect may be on the order of several tens of meV as has been shown for other surface acceptors[108].

▶ The acceptor binding energy E_A might depend on the vicinity to the surface as shown for donors[111]. Additionally, the binding energy can change due to Coulomb interaction with other nearby acceptors. This effect also can be on the order of several tens of meV.

These effects will be addressed in the following sections.

5.4.1   Tip work function and shape of tip induced potential

According to equation 5.3 the voltage U_{chg} at which the ring crosses the acceptor position is directly linked to the tip work function. This quantity introduces the largest uncertainty into the experiment.

Therefore the measured U_{chg} can conversely be used to measure the tip work function within an accuracy of several tens of meV. In the particular measurement of Figure 5.1 the tip work function was determined to be $\Phi_{tip} = (4.38 \pm 0.1)\,\text{eV}$.

Following the model developed in this chapter, the specific shape of the observed ring-features can now be interpreted as the signature of the lateral tip-induced band-bending profile for different bias voltages. The observed rings can be understood as lines of constant tip-induced potential as probed by the acceptor. This shape will only be circular for very regular tips and smooth acceptor potentials. Only such tips will accurately reproduce the local symmetry of the Mn wave function in dI/dU maps like in Figure 5.2. It can be assumed that the apex of this particular tip was very symmetric, leading to the high symmetry of the observed ring feature in relation to the Mn acceptor position. Other tips yield more or less distorted or crooked contours. A schematic view of this idea is illustrated in Figure 5.8.

The observed non-circular asymmetric arcs, as well as profiles having their center aside the Mn position (like in Figure 5.1, and 5.8 left) are due to tips which were irregularly shaped at the very end. The tip used for these images
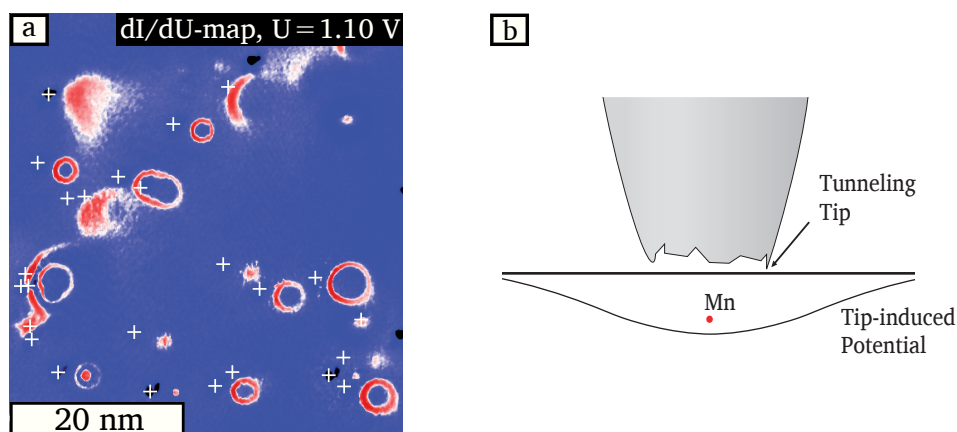
Figure 5.8: **Offset between imaging tip and tip induced potential. (a):** dI/dU-map where the switching rings are not centered on the Mn position. **(b):** Sketch of irregular tip where the imaging part is at the perimeter of the tip apex facing the surface.

presumably had its foremost, imaging tip atom aside from the symmetry center of the tip-induced potential.

We can infer the tip-induced potential if we analyse how the ring shape evolves with increasing bias. The reasoning is as follows: Whenever the tip measures a ring/peak, at whatever bias voltage and position, it means that the acceptor level is aligned with the sample Fermi energy through band bending. Therefore we know the exact bias to apply at a certain location relative to the impurity in order to cause that specific amount of band-bending at the impurity. This amount is simply the position of the acceptor level with regard to the bulk Fermi energy. This requires that the acceptor levels are not significantly changed by surface effects or interaction, and therefore we focus on acceptors which are well separated from others and do not seem to be affected by neighbours.

Figure 5.9 shows an analysis of the ring diameter depending on the applied bias for acceptors in the second, third and eighth layer. There is a variation in the overall energetic position of the feature, due to the effects described in the following section. Apart from that, the lateral run of the curve is smoother for the deeper acceptors and steepest for the highest one. This reflects the fact that the tip-induced potential will be more pointed at the surface and smoother deeper into the sample.

5.4.2 Screening, binding energy and Coulomb interaction

Charge screening

As shown in Section 5.3 the strength[§] of the switching peak in dI/dU indicates the magnitude of the local potential offset caused by a switching acceptor. It is proportional to the step in $I(U)$ which itself directly depends (monotonically) on

---

[§]precisely the integral
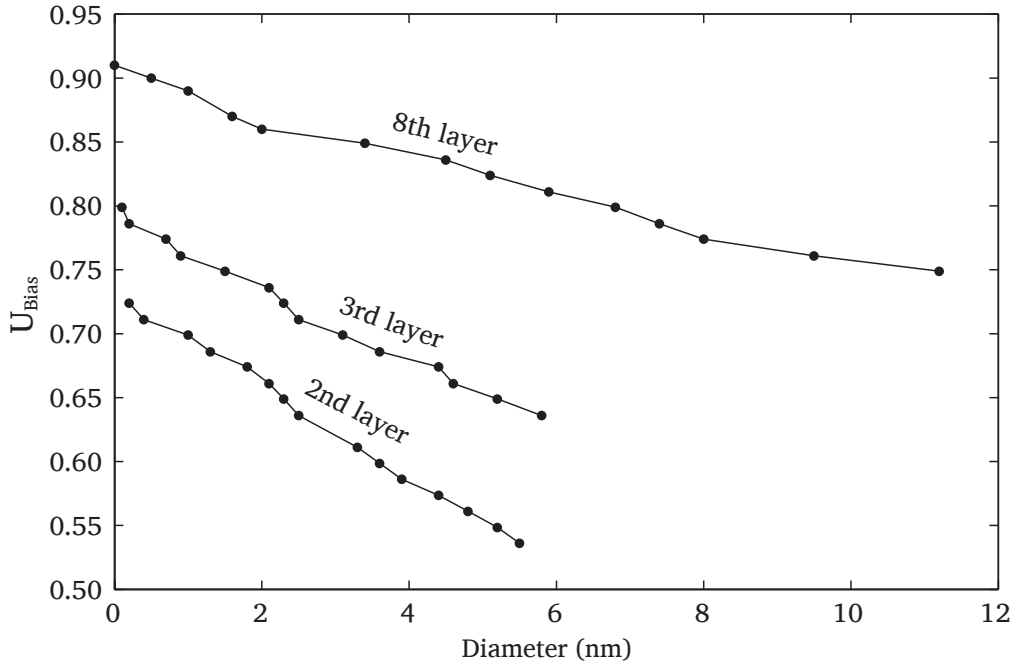
Figure 5.9: Energy-dependent charging radius of Mn acceptors in InAs. Acceptors two, three and eight layers beneath the surface show significantly different curves. Closer to the surface, the tip induced potential falls off faster. For deeper acceptors, an increasingly stronger potential is needed to switch them. All data points were extracted from the same measurement (spectroscopic field; $U_{\mathrm{stab}} = 2\,\mathrm{V}$, $I_{\mathrm{stab}} = 2\,\mathrm{nA}$, $U_{\mathrm{mod}} = 20\,\mathrm{mV}$).

the potential change at the tip base point. As a consequence, the lateral decay of the peak amplitude is a direct measure for the decay behavior of the screened Coulomb potential of the charged acceptor in the sample material. It can therefore be used to locally measure the screened potential for individual acceptors directly and compare to models like Eq. 5.9.

Acceptor binding energy

As stated before, the bias voltage at which the ring crosses the Mn acceptor can be unambiguously assigned to the voltage U_{chg} at which the acceptor is pushed above E_{F}. Note that U_{chg} is close to, but different from the bias voltage U_{FB} (flat band condition) by several tens of meV, since the acceptor level is not exactly at the Fermi level. Furthermore, E_{acc} as measured at the surface can differ from the bulk value due to the confinement effect of the tip induced band bending or other surface-related effects.

Figure 5.10 shows spectra, all taken with the same tip, on several acceptors found within a 20 nm-by-20 nm region of the sample. Obviously there is a large spread of the peak energies, even within the same depth. Peak positions in the range $V_{\mathrm{peak}} = (0.45\text{--}1.0)\,\mathrm{V}$ can be found. According to Section 5.2.1, this amounts to a variation of about $(0.1\text{--}0.2)\,\mathrm{eV}$ of the surface band bending. More peak energies, now gathered from a wide range of measurements with different tips,
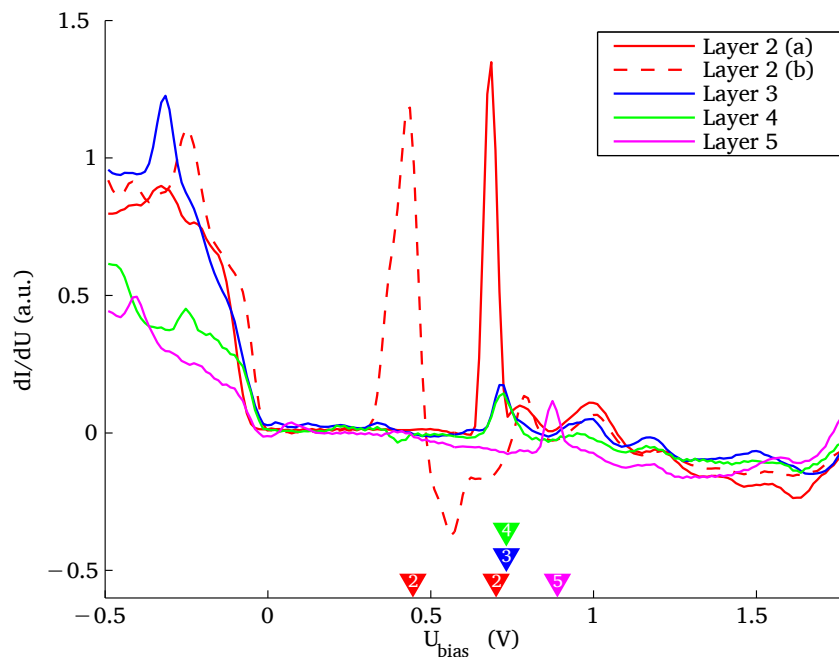
Figure 5.10: Variation in position and strength of the switching peak. The substrate's spectrum has been subtracted from each curve. All spectra were taken with the same STM tip, in the same measurement (spectroscopic field). ($U_{stab} = 2\,V$, $I_{stab} = 2\,nA$, $U_{mod} = 20\,mV$)

are plotted vs. acceptor depth in Figure 5.11. Measurements with the same tip have identical markers.

From this set of measurements, some trends can be found. First-layer acceptors seem to consistently switch around $(0.55\pm0.05)\,V$, i.e. $0.15\,V$ lower than second-layer acceptors. Also, looking at measurements with the same tip, there seems to be a trend towards lower switching voltages for acceptors from the second layer on down.

A similar effect was recently demonstrated for Si-donors in GaAs (ref. [111]) where a number of undisturbed[¶] acceptor levels could be measured. There the conclusion was made that the acceptors' binding energy is increased toward the surface. To actually calculate shifted energy levels from peak voltages, one has to separate a depth dependency of the energy levels from the depth dependent tip induced potential. Both effects would naturally have similar length scales. In the cited work the peak voltage decreased with increasing depth while the decay of the tip induced potential leads to increasing peak energies. Therefore, the increase of the donor's energy level towards the surface could be proven in this case.

In our case, the decay of the tip-induced potential into the surface will lead to lowered peak positions for deeper acceptors. As already stated, such a trend is in fact found in second to sixth layer acceptors among measurements with identical tips (filled squares and discs in Figure 5.11).

[¶]by Coulomb interaction
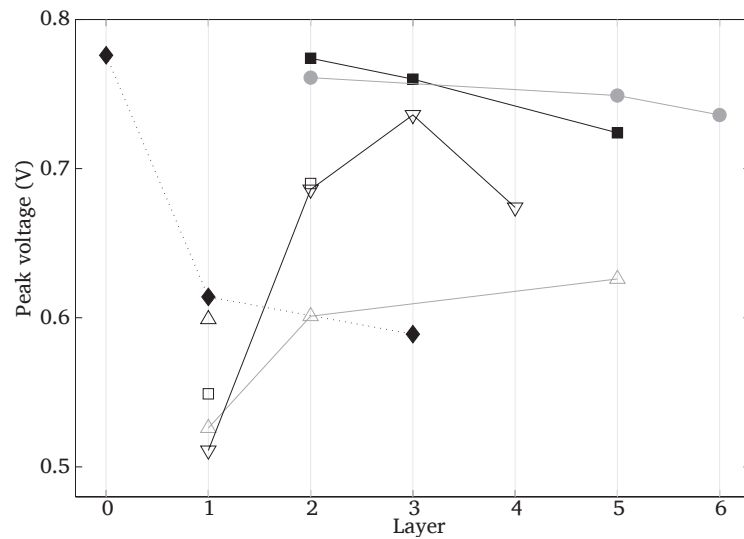
Figure 5.11: **Charging peak position versus embedding depth of Mn acceptors in InAs.** Identical symbols mark measurements with the same microtip.

The fact that first layer manganese acceptors show the inverse trend therefore indicates that its binding energy is significantly enhanced by the proximity to the surface. However, a quantitative conclusion as in [111] can not be made in our case. The variations of the peak positions in one layer due to Coulomb interaction between the manganese acceptors is significant.

Coulomb interaction

According to the considerations up to here, all acceptors in the same depth should share the same ionization energy, as we did not consider Coulomb interactions between the acceptors. According to our model, charging rings in dI/dU-maps should all have the same radius given a certain bias voltage and acceptor depth. This is true for example for a number of fifth layer acceptors in Figure 5.12(a), where acceptor positions are labeled with their respective depth. The three fifth layer acceptors marked with a white ring around the label show charging rings of identical diameter, while the one with a green circumference exhibits a larger ring. We attribute this to modified ionization energies due to Coulomb interaction between multiple acceptors.

An intriguing observation can also be made at those points where two circles or rings intersect, as for example in Figure 5.1(d) and the close up in Figure 5.12(b), where the rings seem to form a kind of anti-crossing. The straightforward interpretation is that once one of the two involved acceptors (A or B) is charged, the potential shift will cause the other acceptor to require a stronger tip induced field to get charged. This will offset the occurrence of the charging related features of this acceptor and creates an area of the sample surface where exactly one of the acceptors is charged and one is uncharged. This leads to the interesting question if the handover between where acceptor A is charged and
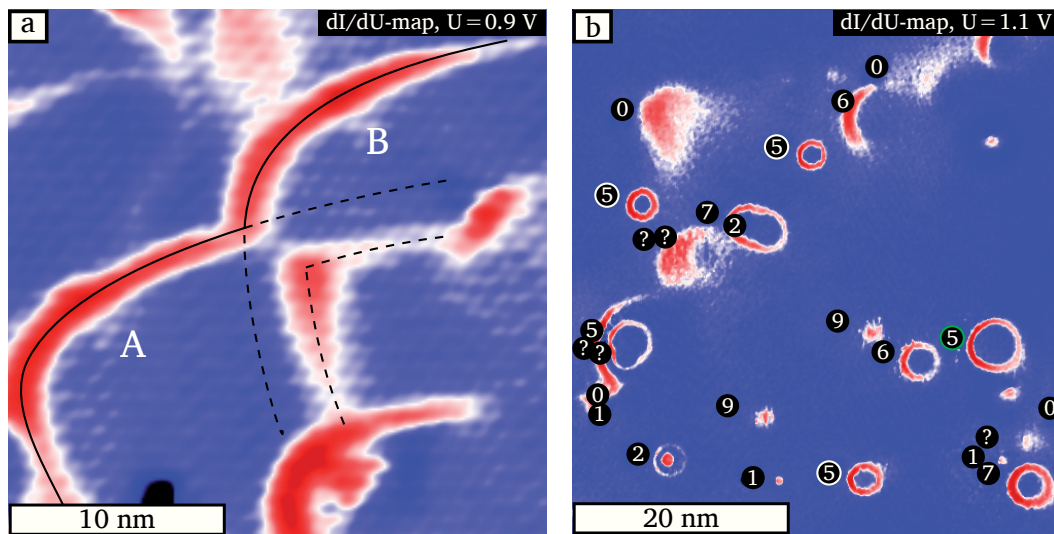
Figure 5.12: Charging rings and their interaction. (a): Two rings form an "anti-crossing". In the overlap region, the presence of the first charge offsets the energy for the second through Coulomb interaction. **(b):** The numbers give the depth of each acceptor (unless ambiguous). Ring sizes are mostly consistent among the same depth (see depth-5 acceptors marked with white ring). One depth-5 acceptor (marked with green ring) differs due to interaction with neighboring impurities. ($I_{stab} = 0.5\,\mathrm{nA}$, $U_{mod} = 10\,\mathrm{mV}$)

acceptor B is neutral and the opposite situation can be experimentally detected and characterized. The detailed analysis of such crossings can be used to study the Coulomb interaction between individual acceptors but is beyond the scope of this work.

5.4.3 Interpretation of bow tie feature as charge density of bound hole

In the course of this chapter we have established the understanding that at U_{chg} and higher bias voltages the acceptor is neutral (A^0 state) while below this point it is negatively charged (A^- state). We have therefore identified two separate contributions to the overall conductance measured with STM/STS: (i) the sudden LDOS shift due to the switching charge and (ii) the tunnel path through the acceptor level which is available at U_{chg} and above. While the first one is by definition of transient nature and can only be observed at the switching voltage, the tunnel path through the acceptor is available over a certain range. It is limited at the lower end by the acceptor turning negative at U_{chg} and above by the tunnel path being suppressed by other effects.

This differentiation now allows us to interpret the bow tie feature which shows up after the charging ring has passed over the acceptor location as the LDOS of the acceptor state A^0. We now have clear indication for each individual acceptor, at which bias voltage we are mapping the bound-hole wave function of the acceptor state.

Summary

A complex spectroscopic feature set can be found on Mn acceptors in InAs: (i) conduction band related rings with increased dI/dU and peak energies shifting coherently with the lateral distance between tip and acceptor, as well as the acceptor's depth, (ii) a combination of peak and NDC localized on the Mn acceptor.

Comparison with a simple model in a Tersoff-Hamann picture, taking into account the tip induced band bending, reveals that (i) can be fully explained by the tip-induced quantum dot which discharges individual acceptors with increasing bias voltage and thereby influences the conduction band LDOS at the tip position.

The model additionally shows that the strength of the peak in the dI/dU signal belonging to the ring can be taken as a quantitative measure for the strength of the acceptor potential at the tip base point. The distance-dependent decay of the peak thus allows to gauge the screening behavior for acceptor charges.

Knowing each acceptor's charge state in each of our measurements, we can assume that the bow-tie shaped feature that is observed on a neutral acceptor is directly related to the actual charge density of the wave function of a hole bound to the acceptor. This assumption will be substantiated in the following chapter.

This interpretation differs from the conclusions of LOTH et al. on Zn and C impurities in GaAs, where a similar anisotropic feature and NDC was explained by resonant tunneling through evanescent gap states[64].

Chapter 6

The manganese acceptor state

This chapter addresses the manganese acceptor state itself. A key result of the previous chapter was that the charge density of the hole bound to the acceptor (in the following called *acceptor charge density*) can be imaged directly at voltages right above the charging point. This chapter builds upon this finding and investigates this shape systematically[69]. The first part will focus on the observed shape of the charge density which still is the subject of an ongoing debate about different acceptors in semiconductors. After that, the dependence of the shape on the embedding depth will be investigated and compared to bulk tight binding model calculations. This is followed by a spectroscopic study of the excited spin states of acceptors close to the surface. Finally, effects of the acceptor on the host bands are investigated.

6.1   Surface induced asymmetry of the bound hole

As shown in Chapter 5 the bow tie shaped appearance of the manganese impurity as it occurs in topographs can be directly related to the charge density of the hole bound to the manganese acceptor. In this section we analyze the shape and asymmetry of the charge density as a function of the depth below the (110)-surface.

As reference, an STM topograph taken slightly above U_{fb} is shown in Figure 6.1. The manganese acceptors seem to appear in a broad variety of geometries, depending on their depth below the surface. Most notably acceptors in the surface layer and first subsurface layer differ significantly from the deeper ones.
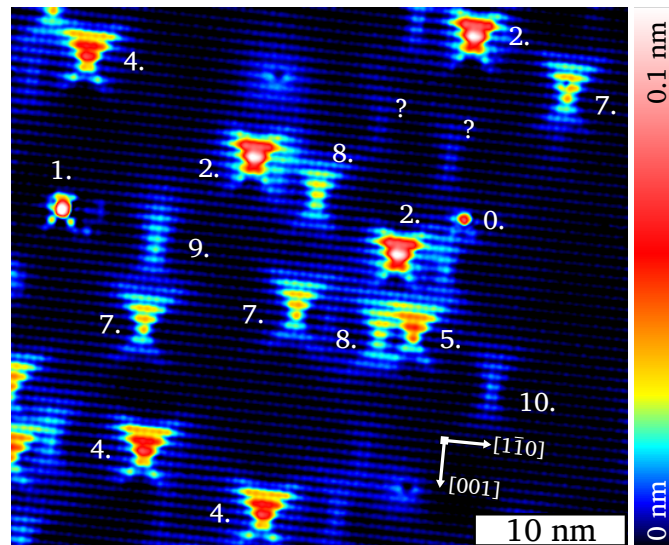
Figure 6.1: **Variety of depth related appearances of manganese acceptors in a 35 nm-by-30 nm STM topographic image of the InAs(110) surface.** Numbers indicate the depth of each dopant, where it can be determined with sufficient certainty. ($U_b = 1.1\,\text{V}$, $I_{set} = 0.5\,\text{nA}$)
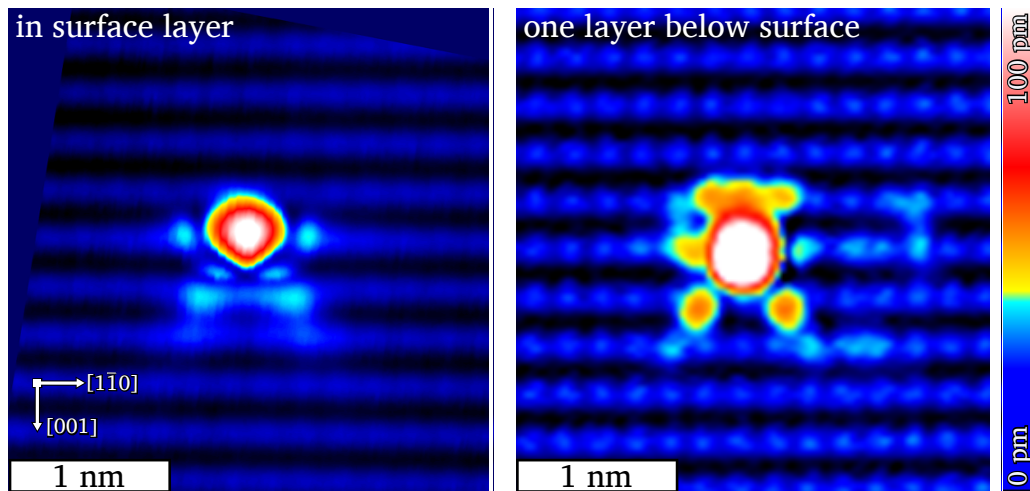
Figure 6.2: **Topographic STM images of (left) surface layer and (right) first subsurface layer manganese acceptors in InAs.** ($U_b = 1\,\text{V}$, $I_{set} = 1\,\text{nA}$)

6.1.1   Acceptors in the first two layers

Figure 6.2 shows topographic images of a manganese atom in the surface and first subsurface layer. Since conduction band tunneling is still weak, the charge density of the bound hole is prominently visible. The surface layer manganese atom appears mainly as a 80 pm high and 1.4 nm wide protrusion, centered between two As-dangling bonds on a $[1\bar{1}0]$ As-row. The main protrusion has a round shape tapered on one side forming a well-defined corner pointing in $[001]$ direction. The protrusion features satellite spots 0.7 nm in $[1\bar{1}0]$ direction on each side,

as well as a series of smaller protrusions extending about 1.5 nm diagonally in the $[1\bar{1}2]$ and $[\bar{1}12]$ directions within the surface plane. An almost identically looking shape was found for manganese atoms manipulated vertically into the GaAs (110) surface[54].

The manganese acceptor in the first subsurface layer shows up as a 120 pm high circular protrusion. It appears centered on the As-grid of the surface and features the same satellite spots like the surface layer manganese, but now the three As atoms right next to it in $[00\bar{1}]$ direction protrude from the background corrugation as well. Interestingly, within the voltage range where the acceptor charge density is imaged, the overall topographic height for the surface acceptor appears to be 30 %–40 % lower than for one in the first subsurface layer.

6.1.2 Acceptors in deeper layers

Figure 6.3 shows topographic images of manganese acceptors from two layers down to nine layers below the surface. All images were taken at $U_b = 1$ V. The color scales are adapted individually for maximum contrast and are not comparable between images.

At every observed embedding depth, the manganese feature is constricted in the $[1\bar{1}0]$-directions to less than four surface unit cells, about 1.2 nm, while in $[001]$-direction it extends about 4 nm, corresponding to about seven surface unit cells.

One can nicely see the alternating alignment of the center of the hole charge density with the As surface lattice, in $[001]$ direction as well as in $[1\bar{1}0]$ direction. The structure of the crystal (including the (110) surface) is mirror symmetric with regard to the $(1\bar{1}0)$ plane. This symmetry with regard to a plane through the acceptor's center (vertical in Figure 6.3) is obviously conserved by the bound hole charge density. The general shapes of the acceptor states are rather similar to the ones observed for Mn in GaAs[118].

There is however a strong asymmetry with regard to the (001) plane (horizontal in Figure 6.3).

This asymmetry is strongest for acceptors closer to the surface. States in the second layer, for example, appear brighter in the $[00\bar{1}]$ half[*] compared to the $[001]$ half, leading to the triangle shape. For second and third layer acceptors, the feature even seems to lie completely on one side of the acceptor.

The asymmetry is reduced for deeper acceptors (e.g. 7th to 9th layer), and for very deep ones (like for example those marked by question marks in Figure 6.1, where the depth could not be determined without ambiguities) the shape becomes symmetric, resembling a bow tie.

Although the (001) plane is a symmetry axis of the fcc structure, even with a $\{(0, 0, 0), (1/4, 1/4, 1/4)\}$ base, as long as it consists of just one species, a comparison to the crystal structure given in Figure 4.5 shows that the (001) plane is in

---

[*]the upper half in Figure 6.1 and Figure 6.3
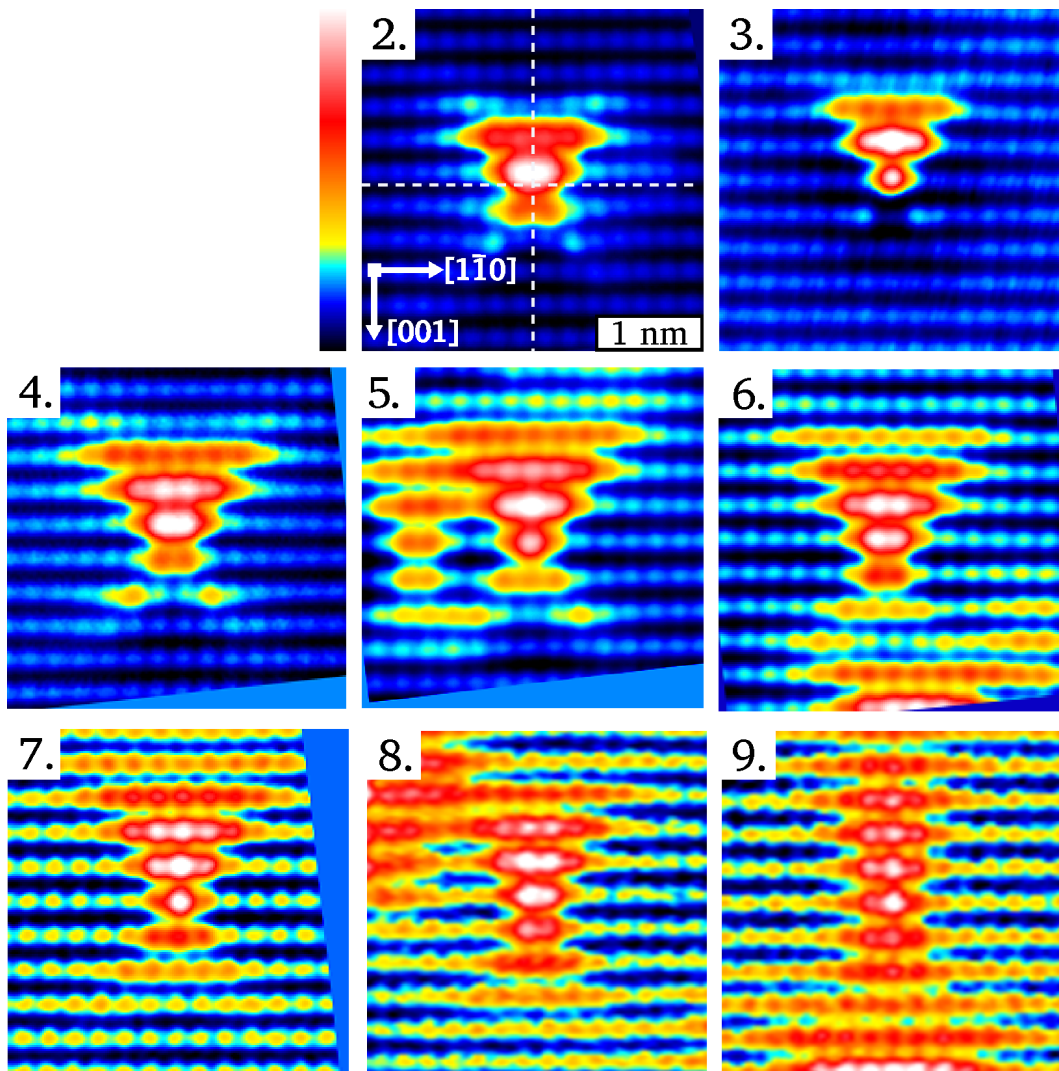
Figure 6.3: Shape asymmetry of the bound hole charge density in topographic measurements. Topographic appearance of manganese acceptors in the second to ninth layer, as indicated by the numbers. Close to the surface the features show a much increased asymmetry with regard to the $[001]$ direction, resulting in a triangular shape. The asymmetry declines with increasing depth, approaching an almost perfectly symmetric bow tie shape at the ninth or tenth layer. Color scales are individually adjusted for maximum contrast and are not identical. ($U_b = 1\,\text{V}$, $I_{set} = 1\,\text{nA}$)

fact not a mirror plane of the (110) surface of a zinc-blende crystal. Thus a small asymmetry of the bound hole charge density can be expected.

6.1.3 Tight-binding model calculations

In order to find out whether this effect is strong enough to explain the observed asymmetry, tight-binding model (TBM) calculations were performed in collabo-

ration with Jian-Ming Tang[†] and Michael E. Flatté[‡]. The calculations were made for a single acceptor in a bulk surrounding. This highly symmetric geometry (without a surface) greatly reduces the computational effort, making the treatment of single impurities with TBM possible[69]. As an approximation for the LDOS of an acceptor in the nth subsurface layer as measured by the STM tip 6 Å above the surface, we calculated [110]-plane cuts through the logarithm of the TBM-calculated LDOS of a single manganese acceptor in a bulk environment at distances of n (110)-planes. The resulting images are shown in Figure 6.4.

They show an LDOS with overall box-like contours increasing towards the manganese center. The TBM images show the As lattice as well, since there is some As-related DOS at the energy of the acceptor level. This again makes the alternating alignment of the center of the bound hole with the surface lattice nicely visible.

The TBM data largely reproduce the extension and the general shape of the experimentally observed LDOS of the bound hole. For the surface and first subsurface acceptor, even though there are differences between STM images and calculated LDOS, some small details of the feature (like for example the protrusions in $[1\bar{1}2]$- and $[\bar{1}12]$-direction on the surface layer acceptor in Figure 6.2 and Figure 6.4) are observed in both experiment and calculation.

There are however obvious discrepancies, the most obvious being that the TBM features, unlike in our measurements, are much more symmetric with regard to the (001) plane.

With increasing depth of the acceptor the agreement between the theoretical and experimental results improves as the deeper features in STM approach more symmetric shapes. At depths of eight and nine layers the shapes are nearly identical. This depth corresponds to about half the lateral extension of the acceptor in terms of an $1/e$ decay of the acceptor state LDOS and is also the limit for our method of determining the depth in STM images.

Another difference between STM and TBM results is that while the acceptor state LDOS in the tight-binding model seems to have an almost box-like appearance, the experimentally observed features have a bow tie shaped envelope.

6.1.4   Reasons for enhanced asymmetry

The large agreement between bulk TBM calculated acceptor LDOS and experimental STM topographs for acceptors deep below the surface gives further evidence that STM indeed images the charge density of the bound hole.

However, for acceptors close to the surface the charge density appears deformed in comparison to its bulk shape. Most notably we observe a strong (001) mirror asymmetry. This asymmetry is of course not reproduced by the bulk TBM, since by design it does not model the surface at all.

[†]University of New Hampshire
[‡]University of Iowa
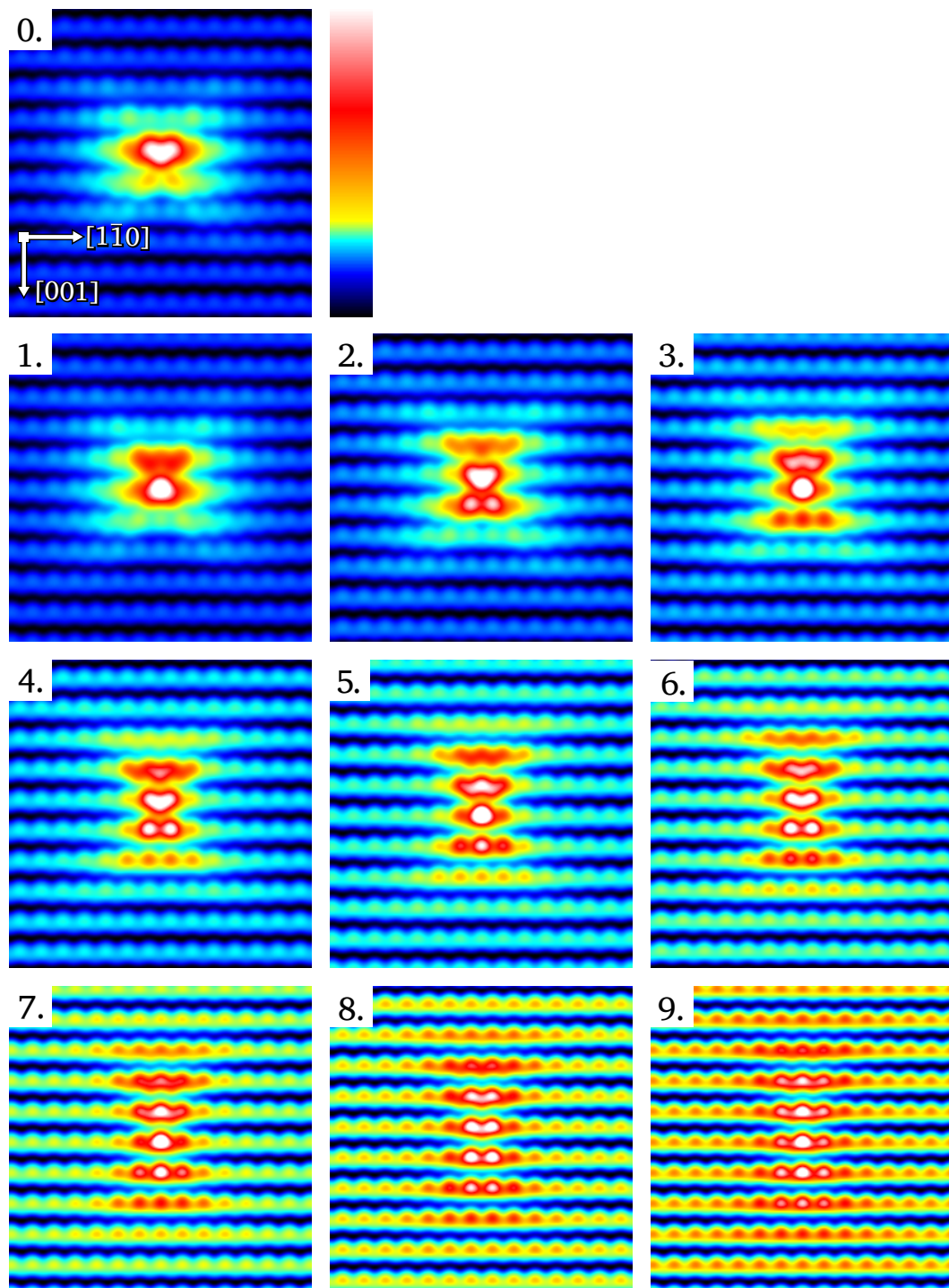
Figure 6.4: **TBM calculated LDOS maps of a manganese acceptor in InAs.** The calculation was made for a bulk configuration without a vacuum interface. The images show the logarithm of the LDOS in several cuts in (110) planes with increasing distances from the manganese center. Each cut's offset in number of lattice planes is given in each image.

Asymmetries of shallow and deep acceptor-related states close to (110) surfaces have been discussed before for Zn, C and Be impurities [58; 63; 64; 67], and only recently a number of explanations have been investigated systematically and with convincing conclusions[16; 45; 61; 62; 73; 117].

Several effects can occur at the surface which would therefore not be reproduced by the bulk model. **[i]** The acceptor state can be modified by the potential step and a reduced dielectric constant at the surface[86], creating confinement effects[9; 84]. **[ii]** The surface reconstruction/relaxation modifies the lattice geometry close to the surface, thus creating a chemically modified, strained environment for the impurity[30; 62; 73; 111]. **[iii]** Surface states can hybridize with impurity states[45]. **[iv]** There can be surface related charge accumulation that creates a potential gradient which might affect the acceptor wave function[62].

The last explanation (iv) can be ruled out in this case, because the asymmetry is present even in the flat band case, i.e. $U_{fb} \approx 0.8\,\mathrm{V}$ where the applied bias compensates any band bending and there is no field gradient at the sample surface. Confinement effects (i) due to the presence of the surface will most likely not play a major role except for the top one to three layers, because a sufficient state density needs to be affected by the vacuum potential. This leaves the lattice geometry as the major cause of the asymmetry.

It is well known from density functional theory (DFT) calculations and experimentally[27; 29; 30; 57] that the InAs (110)-surface is strongly strained due to surface relaxation. Moreover, it was shown in experiments that uniaxial strain in [110]-direction leads to a large anisotropy in the electron propagation properties in GaAs[20]. There is in fact a strong relaxation (Figure 4.5(b)) leading to a 30° buckling of the In-As zig-zag lines which moves the As atoms up and the In atoms down. The DFT calculations suggest that the strain from this relaxation permeates several atomic layers into the surface. Loth et al.[61; 62] performed band structure calculations for a bulk InAs crystal with a modified crystal structure to emulate the strain at the (110)-surface. Their results strongly suggest that the surface-related strain is in fact the cause of the warped acceptor hole wave function. It was also demonstrated experimentally in a recent STM study that strain (induced by embedded quantum dots) distorts the manganese acceptor wave function in GaAs, lowering the spatial symmetry of the acceptor state [117]. Therefore it seems reasonable to conclude that the surface relaxation at the InAs(110) surface indeed causes the observed strong asymmetry by modifying the acceptor wave function.

However, an additional effect on the anisotropy can result from the hybridization of the bound hole with surface states as shown in [45].

6.2   Higher energy spin states

Figure 6.5 shows the LDOS produced by the TBM, at several locations in the lattice (manganese impurity, its next As neighbors, host In and host As). At the manganese impurity and even on its next As-neighbors there is a close standing

series of three pronounced peaks. These peaks correspond to the hole ground state (0:$p_x - ip_y$) at $E_0 = 28$ meV, and two spin-excited states (1:p_z and 2:$p_x + ip_y$) at $E_1 = 0$ meV and $E_2 = -50$ meV. These energy differences are too large to be splittings of just the $J = 1$ acceptor ground state by reasonable strains or local electric fields [100]. Similar to the case for Mn in GaAs, the TBM calculations predict that spin-orbit interaction leads to higher-energy spin states of the bound hole above the $J = 1$ ground state.
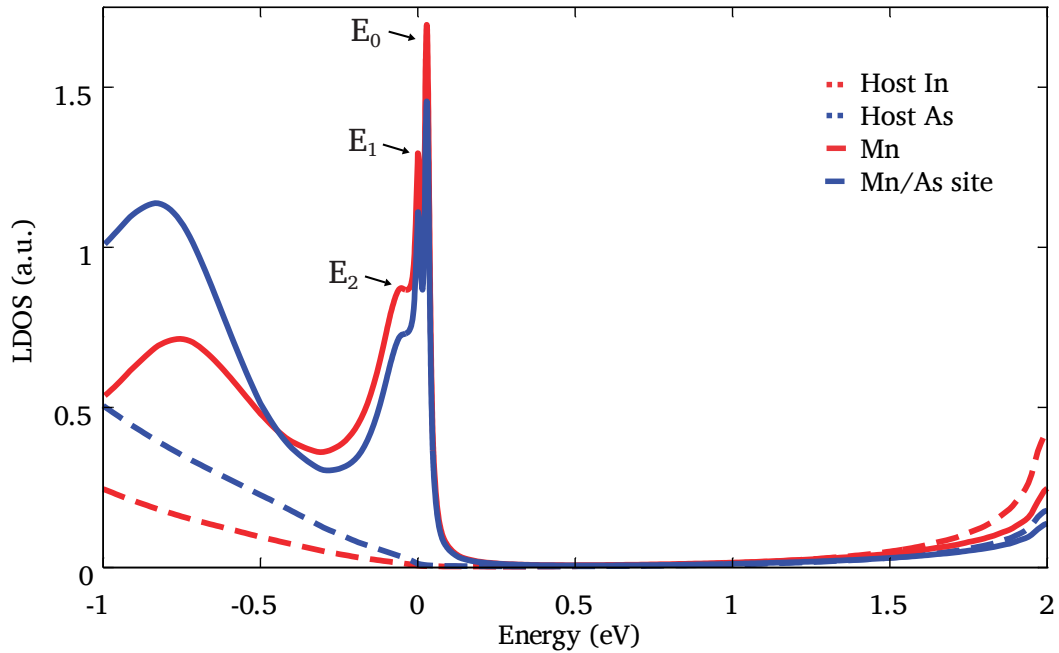
Figure 6.5: **TBM calculated LDOS of manganese acceptor and InAs.** — **Solid red:** LDOS at manganese center; **Solid blue:** LDOS at Mn's next As-neighbor; **Dashed curves:** LDOS at host In and As sites. The hole ground state and two excited states form a peak triplet around the Fermi energy. The valence band LDOS is enhanced on the manganese impurity, while its conduction band LDOS is reduced.

Additionally, the LDOS is strongly enhanced in the range of the bulk valence band, especially below -0.5 eV. In the conduction band voltage range at the upper end of the energy scale in the figure, there is a significant reduction of the LDOS in the vicinity of the acceptor.

Figure 6.6 shows calculated LDOS maps at the energies of each of the three hole states identified in the calculations. Just like before in Figure 6.4, the images show cuts along (110) planes through the logarithm of the LDOS in increasing mono-layer distances from the impurity center. The two lower states E_0 and E_1 appear almost indistinguishable. The p_z state E_2, though, turns out to be slightly more localized, as it shows a smaller extension of the LDOS throughout the whole series of LDOS maps, while also showing less overall intensity compared to the host lattice background LDOS or the other two states.
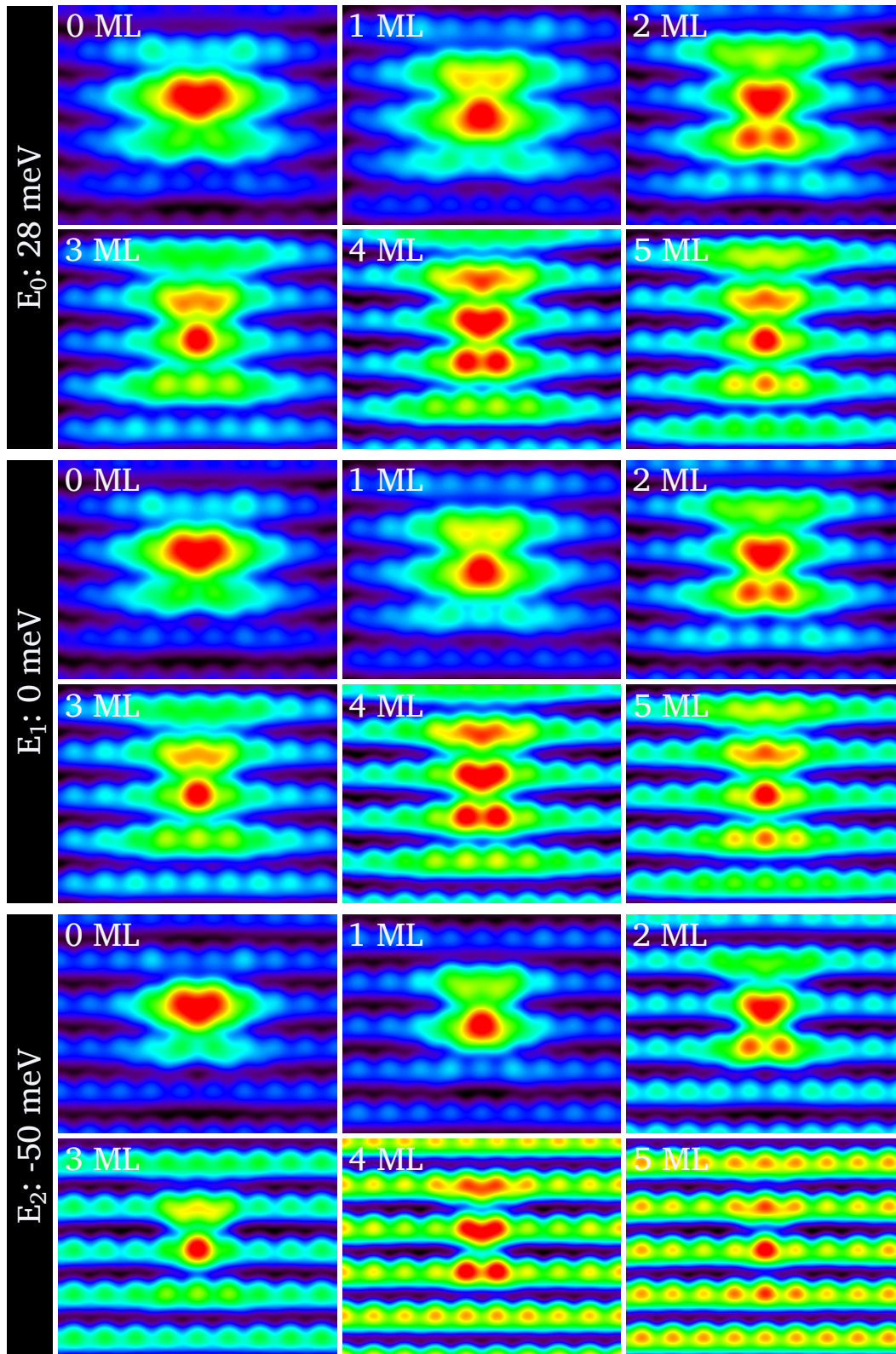
Figure 6.6: TBM calculated LDOS maps of the hole ground state and two excited states. Six maps are shown for each state, showing cuts through the LDOS in a (110) plane in increasing lattice plane distance from the center, as indicated in each image. The colorscale is the same as in Figure 6.4.

6.2.1   Detection of higher states by STS

In the following, we would like to answer the question if and how the excited states appear in scanning tunneling spectroscopy measurements. What complicates the interpretation of STS-spectra is the fact that at positive voltages, as mentioned in Section 5.2, the state spectrum is not obtained by sweeping the tip DOS across the sample energy scale as is the usual understanding of STS. As explained there, our experiment exhibits an additional way of probing the acceptor states, apart from the one usually considered in STS, which is by shifting sample energy levels through the sample Fermi energy and detecting a current increase due to the state becoming conductive. Figure 6.7 illustrates how this affects our measurements of the hole states.
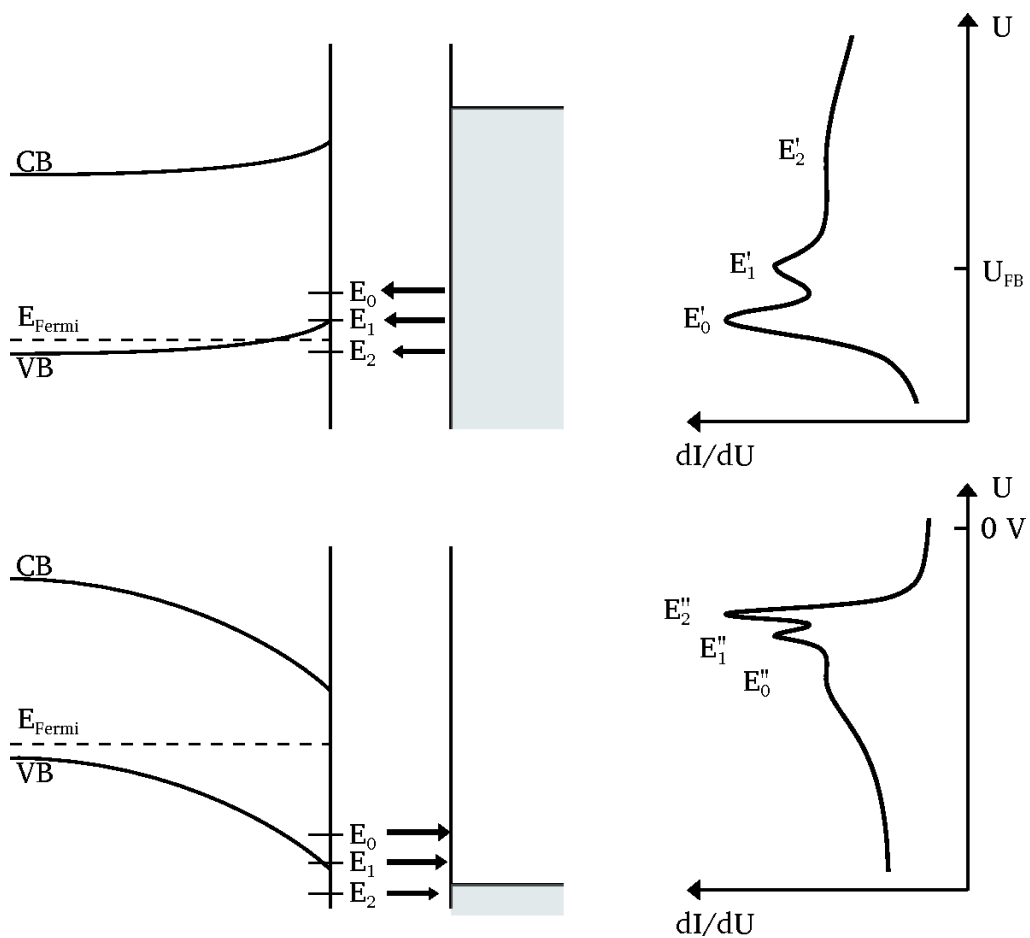
Figure 6.7: **Illustration of regular spectroscopy and band offset spectroscopy of hole states.** — **Bottom left:** Voltage condition when measuring states directly. **Bottom right:** resulting dI/dU curve. **Top left:** Situation around flat band voltage, when the hole states are aligned with the sample's Fermi energy by the tip-induced band bending. **Top right:** resulting stretched spectrum (see text).

As usual, there is the direct way of detecting states in STS (depicted in the bottom sketches of Figure 6.7) by ramping the tip's Fermi energy across the ac-

ceptor levels. In our case due to band-bending this can be observed at negative voltages below the bulk values. The main effect of the band bending here is that the states appear shifted down on the energy scale.

The other mechanism of detecting the hole states is depicted in the upper sketches in Figure 6.7. There, the situation is the following: The applied bias roughly compensates the work function difference leading to flat bands in the semiconductor. Therefore the tip's Fermi edge actually is about 0.8 eV *above the probed state*. As explained in detail in Chapter 5, by shifting the surface potential by means of tip-induced band bending, the acceptor levels are consecutively lifted across the bulk Fermi level, activating them one after the other which leads to individual peaks in the dI/dU measurement (see also Figure 5.5).

This has a number of consequences for the interpretation of our spectra. The most important one is that instead of the applied bias, the amount of band bending at the location of the acceptor will be a more appropriate energy scale to look at. If for example the band bending at the surface amounts to $+100\,\mathrm{meV}$ for a certain bias voltage, states which in bulk terms are $100\,\mathrm{meV}$ *below* the Fermi energy now coincide with the Fermi energy. Their DOS is emptied and becomes available for tunneling, which in turn generates an according dI/dU-intensity. This means the sample energy scale is probed "backwards", i.e. from higher to lower energies in the density-of-states. So the first level that crosses E_F is E_0 followed by E_1 and E_2. The rate at which the states are lifted is determined solely by the dependency of the tip-induced band bending on U_b.

As can be seen in the graph in Figure 5.5, $d\phi_\mathrm{bb}/dU_\mathrm{b} \approx 1/5$ in this voltage range. Therefore when we ramp the bias voltage by $100\,\mathrm{mV}$, we lift the band bending by $\approx 20\,\mathrm{meV}$. In other words, due to the gentle slope of $\phi_\mathrm{bb}(U_\mathrm{b})$ of $\approx 0.20\,\mathrm{eV/V}$, the sample energy scale appears widened by a factor of about 5 in STS measurements. We therefore expect our peak series around $0\,\mathrm{meV}$ in the sample energy scale to show up in STS spectra aligned with U_fb and expanded by a factor of about five (see Figure 6.7 upper right panel).

Figure 6.8 shows experimentally obtained dI/dU spectra. They were recorded in one continuous measurement within a $17\,\mathrm{nm} \times 17\,\mathrm{nm}$ spectroscopic field consisting of 100×100 dI/dU curves. The top graph shows a spectrum taken on an acceptor and for comparison a spectrum taken far away from any acceptor. One can already see a main peak at about $0.7\,\mathrm{V}$ and two smaller follow-up peaks, as well as an increased signal at negative energies and a slight reduction of the signal with regard to the background above ca. $1.1\,\mathrm{V}$. The follow-up peaks can only be observed with a minor fraction of STM tips. The peaks appear exclusively around acceptors, but never on the bare InAs and thus can be attributed to the Mn.

The next graph, in the middle, shows the Mn spectrum with the InAs spectrum subtracted, which makes the mentioned features even more obvious. For the acceptor state the considerations made above about band-bending mean that its features will appear expanded to about five times their actual width. To really compare theoretical and experimental results, we can determine at which voltage separation the level splittings of $28\,\mathrm{meV}$ (E_0-E_1) and $50\,\mathrm{meV}$ (E_1-E_2) would be
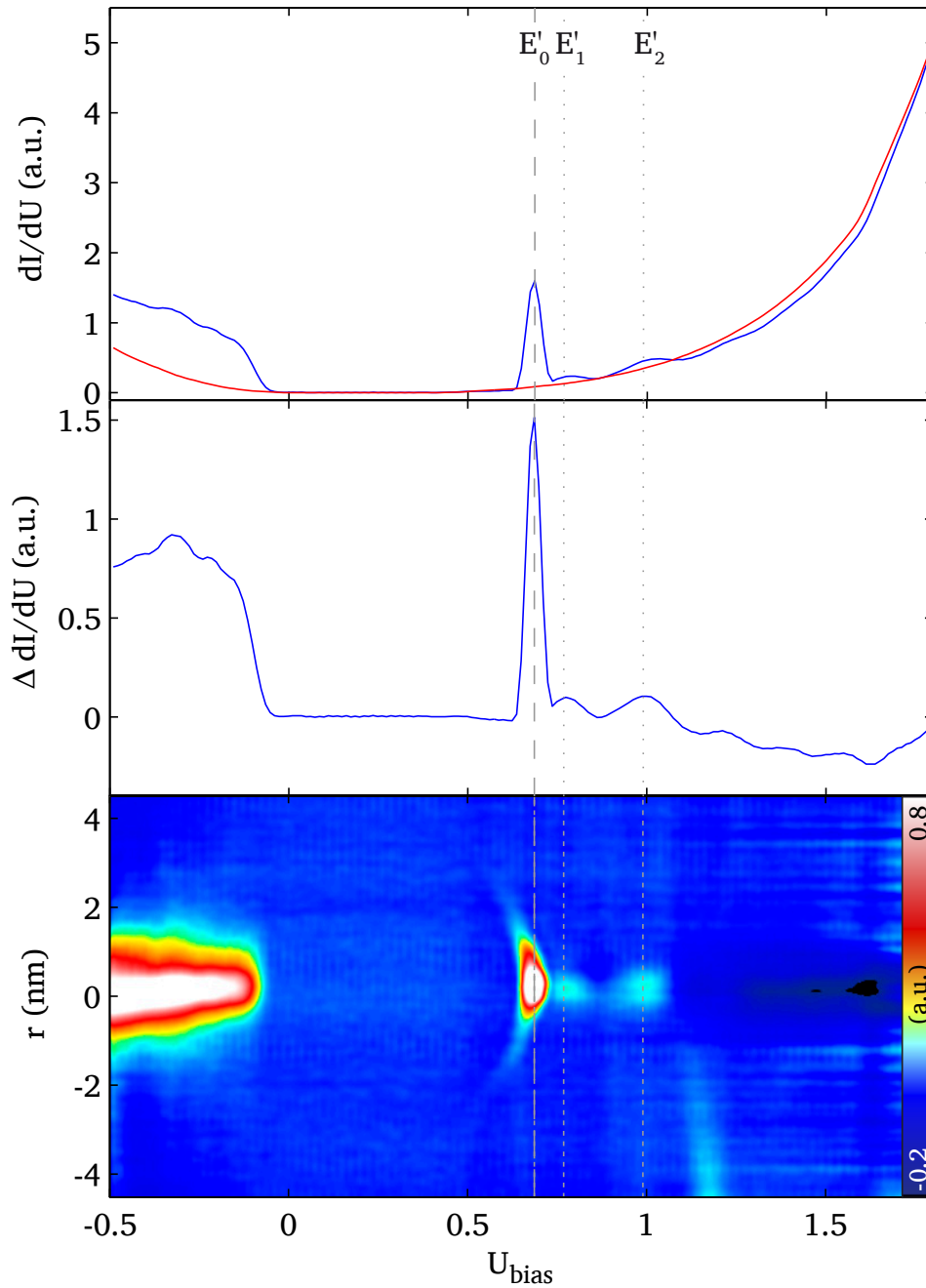
Figure 6.8: Ground state and higher states in STS spectra of a single manganese acceptor. All data in this figure are from the same spectroscopy field. The acceptor is two atomic layers below the surface. **Top:** Point spectra at the center of the acceptor feature (blue) and on a dopant free area (red). **Center:** Mn-spectrum with InAs background subtracted. A series of smaller peaks is visible above the main peak as well as below E_F in the valence band. **Bottom:** Color coded spectral intensity extracted from spectroscopy field along a line going across the manganese dopant (y-axis). ($U_{stab} = 2\,\text{V}$, $I_{stab} = 2\,\text{nA}$, $U_{mod} = 20\,\text{mV}$)

measured, taking into account the expansion by a factor of five due to tip induced band bending.

Due to the variation in the local potential, the resulting values are more or less offset from the peak in a measurement. So after determining the bias voltages as described, the values were offset to align the lowest voltage (E_0) with the main peak in Figure 6.8, leaving the energy separation unchanged. The resulting voltages are marked in the figure by the vertical dashed and dotted lines. There is a striking agreement with the experimental data, considering that the alignment with the ground state is the only free parameter for this match.

The bottom graph of Figure 6.8 shows the difference spectrum again, in the same manner as in Figure 5.3(b). Here, the dI/dU intensity is color coded according to the color bar at the right. The y-axis indicates how far away from the manganese center the spectrum was taken. In this presentation it is clear that the E_1 and E_2 peaks are localized to a $\varnothing \approx 2\,\text{nm}$ wide area around the manganese center. This is in good agreement with the TBM calculated LDOS maps of Figure 6.6 where the states also have dimensions of $1.5\,\text{nm}$ to $2\,\text{nm}$.

The calculated spectra show all peaks at roughly similar intensities, the intensity of the E_0 peak ca. 30 % higher than the E_1 peak, while in the experimental spectra the E_0 peak can be as much as 15 times as strong as the next follow-up peak. But we already know from Chapter 5 that this peak is mainly originating from a compression of the conduction band conductivity caused by the charge switching. So we must, as was already indicated in Chapter 5, look for the hole state as an additional peak at basically the same position as the switching peak. In fact, we make the observation that the two peaks are more or less overlapping in most measurements, to the point of being (almost) indistinguishable. Most of the time, if discernible, the acceptor state appears as a shoulder on the switching peak. The shoulder is more or less pronounced, depending on the spectral resolution provided by the tip and possibly other factors. Since the switching peak originates from tunneling into s-like states at the conduction band edge while the acceptor state peak originates from tunneling into the rather p-like hole state, a preference of the tip's imaging state for s-like or p-like states affects their relative magnitudes.

The excited spin states of neutral manganese acceptors have previously been measured optically[60], but are seen here for the first time for an individual manganese impurity on the local scale.

6.3 Manganese acceptor coupling to host states

There were two other features in Figure 6.8 apart from the peaks just discussed. There is also an increased valence band LDOS and reduced conduction band LDOS localized around the acceptor, which we find in our experimental spectra as well as in TBM calculated density-of-states (Figure 6.5). This section investigates these two phenomena further by analyzing the TBM calculated LDOS and additional experimental results.

6.3.1 Valence band

At negative bias voltages where tunneling out of the valence band dominates, dI/dU-curves show an increased signal on acceptors near the surface. Figure 6.9 shows a series of topographic STM images from strong negative bias almost up to zero bias, featuring three acceptors in different depths, plus a positive bias image for reference. All images are adjusted to show the same mapping of height to color so they can be directly compared.

At small negative bias ($-0.2\,\mathrm{eV}$) the acceptors show a strong elevation (bottom right acceptor: $\approx 70\,\mathrm{pm}$, almost twice as high as on the positive voltage side) over the regular As background lattice. The As lattice also appears very pronounced, which is typical for voltages close to the band gap in semiconductors. Proceeding to higher negative bias, the acceptor related contrast flattens more and more until at $-3\,\mathrm{V}$ it becomes hardly discernible ($\approx 8\,\mathrm{pm}$, same acceptor as above). Generally, the features closely resembles their appearance at positive bias.
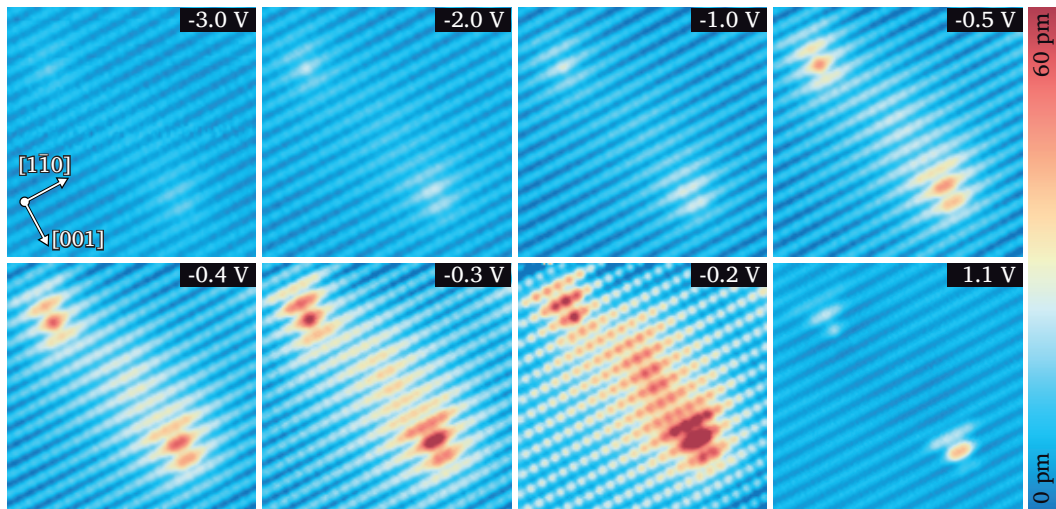
Figure 6.9: **Topographic appearance of manganese acceptors in InAs at negative bias.** (all images 10 nm-by-10 nm, U_b as indicated, $I_\mathrm{set} = 1\,\mathrm{nA}$)

However, the appearance is more symmetric for large negative voltages ($-3\,\mathrm{V}$).

For the corrugation found in the valence band, three causes are possible. First, there might be tunneling out of the hole states into the tip. Due to the notable downwards band bending at zero bias, we expect this to start at significantly lower bias, ca. below $-0.45\,\mathrm{V}$. Second, it can be caused by the fact that the acceptor is negatively charged at these voltages. This additional local potential shifts additional valence band density-of-states upwards, leading to locally increased conductance and therefore to a protrusion in a topographic image. Since this effect is caused by the additional charge, one would expect the observed feature in Figure 6.9 to more closely resemble the distribution of a screened Coulomb potential.

The third effect that can lead to the observed increased LDOS is *p-d* exchange interaction. This will have the effect of locally increasing the LDOS at the manganese impurities[100].

It is likely we are seeing a combination of all three effects.

6.3.2 Conduction band

At very high positive bias much larger than U_{fb}, when tunneling into conduction band states is dominant, as shown in a topographic image and two dI/dU-maps in Figure 6.10, we observe a reduced LDOS. Interestingly, this is not only apparent in dI/dU-maps but can even be seen clearly in topography. The reduction of the conduction band LDOS in this voltage range therefore is strong enough to overcompensate the conductance gain at U_{chg} due to tunneling into the acceptor state.

Another interesting observation can be made in the dI/dU-maps of Figure 6.10. The depressions at the acceptor positions are surrounded by rings of increased differential conductance. These rings change their diameter from ≈ 2.2 nm (first layer acceptor) at 1.5 V to ≈ 1.8 nm at 1.7 V. This is the kind of behavior expected for conduction band scattering states in InAs[113].
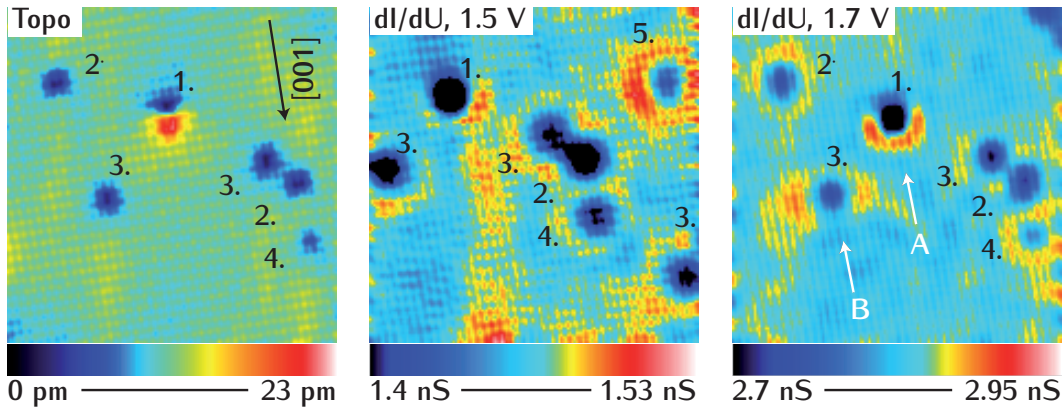
Figure 6.10: Anisotropic conduction band modulation around manganese dopants in dI/dU-maps. Left: 18 nm-by-18 nm STM topography at positive bias (2 V). Manganese acceptors appear as circular depressions. **Center & Right:** dI/dU-maps at $U_b = 1.5$ V and 1.7 V. Manganese acceptors feature a reduced dI/dU-signal in a ≈ 1 nm radius around the center. Additionally, rings of increased dI/dU surround the acceptors. Manganese dopants in the first and third layer show the anisotropic LDOS enhancement predicted by TBM theory. The images were obtained in the same sample area but with slight offsets.

Also, well visible at 1.7 V, a depth dependent anisotropy of the rings is found. In the right image of Figure 6.10 an acceptor in the first layer exhibits the "ring" mostly on the [001]-side (A), while a third layer acceptor has it only on both $\{1\bar{1}0\}$ sides (B).

We can better understand our observations at high bias voltages by looking at TBM calculated maps of the conduction band LDOS in Figure 6.11. Like the TBM

LDOS maps shown earlier, they show (110)-plane cuts through the logarithm of the LDOS at the indicated distances. As already pointed out on the basis of LDOS curves (Figure 6.5), the LDOS maps, just like the experimental ones, show a locally reduced conductance in the area covered by the impurity wave function.

In this voltage range the acceptor is neutral, so there is no net charge that could shift the local potential up. Since the negative excess charge of the acceptor and the hole wave function are not perfectly congruent due to their different nature (nucleus, Bloch states), there is in principle a local charge inhomogeneity. Apart from the extremely low magnitude of such an inhomogeneity, it also is balanced, i.e. for every local positive charge density there has to be a corresponding negative charge close to it. But the effect observed in the conduction band is chiefly a suppression. For this, a net negative charge would be necessary, which we know is not there.
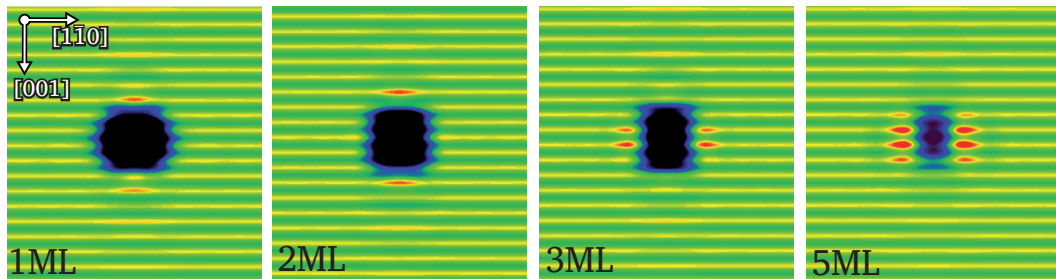
Figure 6.11: Effect of manganese impurity on conduction band density of states in a tight-binding model calculation. LDOS maps of a single manganese acceptor from tight-binding calculations at $E = 1.4\,\text{eV}$ (corresponding to $U_\text{b} = 1.5\,\text{V}$). The LDOS suppression is clearly visible. Around it, small LDOS enhancements can be found in $[001]$ direction for one and two layers distance and in $[1\bar{1}0]$ direction for three and four layers distance.

The tight binding calculations hint at a likely explanation, though. The strong suppression of the conduction band density-of-states is only reproduced by the TBM results if p-d exchange interaction is included in the calculation. The p-d exchange results in a notable suppression of the CB DOS in the calculation, which matches that observed in the experiment in scale and shape[100].

The calculated LDOS maps also reproduce the regions of enhanced LDOS surrounding the impurity that were found in the experiment. Moreover, the distance-dependent anisotropy is also reproduced by the model. The two left hand side images in Figure 6.11 in one and two layers distance show slight maxima in $[001]$-direction, while at three and five layers distance they can be found only in $[1\bar{1}0]$-direction.

The calculated anisotropy of the scattering states depends in detail on the layer as well as on the energy and the strength of the p-d interaction. The best agreement between experimental and calculated results was achieved for a value of $V_\text{pd} = 2.19\,\text{eV}$ for the interaction strength[69].

6.4 Summary

In summary, it was shown that the asymmetry of the manganese bound hole charge density in InAs with regard to the (001) mirror plane is affected by the (110) surface down to at least 7 layers (about the effective Bohr radius). We conclude that the relaxation of the cleaved InAs (110) surface is the most likely origin of this modification. Tight-binding model calculations for bulk dopants reproduce most features found with STM, with the exception of the surface-induced asymmetry, which was subsequently reproduced by calculating a strained crystal[62]. This implies that the acceptor-acceptor interaction can be significantly altered by surfaces and interfaces. This modification will affect the strength as well as the anisotropy of the interaction. As a consequence, results obtained at the surface, e.g. by vertical manipulation[54], are not necessarily representative of bulk characteristics. Higher-spin states of single manganese dopants were directly observed by a novel and unconventional approach in the interpretation of STS spectra. An enhancement of VB LDOS and a suppression of CB LDOS was determined in a region of 2 nm around the acceptor, and indications of anisotropic scattering of CB states by the acceptor were found. Our observations allowed us to determine the strength of the p-d exchange interaction.

Chapter 7

Conclusion and Outlook

This dissertation describes measurements performed on manganese-doped indium arsenide using scanning tunneling microscopy (STM). The focus of the work lies on the investigation of individual manganese acceptors and their interaction with the electrical potential of the STM tip and the electronic states of the host. From observations of charge-switching behavior of individual acceptors, a theoretical model was developed which accurately describes the experimental observations. Apart from new insight into the nature of the acceptor state and its interaction with the host, the model can be used in new measurements to determine sample properties and characterize STM tips. Some highlights of the dissertation are presented below, followed by a short outlook on possible further experimental work.

7.1   Main results

A characterization of the acceptor's bound-hole wave function is presented. We analyze its surface-related asymmetry and demonstrate that it is the result of strain caused by surface relaxation. We show that this strain affects the acceptor wave function as deep as seven layers below the surface.

We present a picture of the band-bending at the sample surface caused by the potential of the STM tip and how it can be utilized to reproducibly switch the charge state of individual acceptors.

A model was developed which incorporates tip-induced band-bending, its effect on the acceptor charge state and which reproduces our spectroscopic measurements. The model can be used to extract the local screening strength in the sample, as well as determine the profile of the tip-induced band-bending, and learn about the effect of the surface proximity on the acceptors' binding energy.

The carrier density of our samples was determined by magnetization mea-

surements and STM observation and was found to be equivalent to the specified manufacturer carrier density. A technique to determine the embedding depth of defects in a semiconductor surface is described. To this end, we relate the shape, the location with respect to the host lattice and the apparent height to determine the absolute depth of acceptors with respect to the surface.

A strong local suppression of conduction band density-of-states at the location of the manganese acceptors is described. Based on tight-binding model (TBM) calculations we conclude that the suppression is caused by $p - d$ exchange interaction with the hole state.

We describe electron scattering in the conduction band around acceptors. The scattering patterns show a notable depth-dependent shape anisotropy. In combination with TBM calculations, this allows us to determine the strength of the $p - d$ exchange interaction.

We experimentally observed the spin-orbit induced splitting of the acceptor ground state into three spin-states, as predicted by tight-binding calculations. This required developing an interpretation of tunneling spectra contrary to the conventional understanding of scanning tunneling spectroscopy.

7.2 Prospects

The method to determine screening behavior and tip-potential shapes described in Chapter 5 can be used on similar systems for the characterization of tip and sample. In a very simple implementation of the method, it can be used to simply classify STM tips as microscopically sharp or blunt.

Calculations by Jian-Ming Tang and Michael Flatté[101] suggest that hole states with different spin orientation have notably differing density-of-states. Therefore the spin-state could be manipulated with an external magnetic field and be detected with scanning tunneling microscopy even without using spin-sensitive STM techniques.

Inelastic tunneling spectroscopy, the acquisition of $\mathrm{d}^2I/\mathrm{d}U^2$, could be used to study elementary excitations like spin-excitations. Such measurements have been successfully carried out for example on manganese adatoms on Al_2O_3 [42; 44], but until recently, were not done on a semiconductor substrate. The first inelastic tunneling spectroscopy measurements of magnetic atoms embedded in a semiconductor were performed very recently on iron adatoms on an indium antimonide surface[53].

Maybe the most interesting and groundbreaking experimental leap would be spin-sensitive STM measurements on magnetic dopants in a semiconductor, similar to what has been achieved on magnetic adatoms on metallic substrates[71; 122]. Ideally, this would be done with spin-polarized STM tip, which are directly sensitive to the spin-polarization of the sample's electronic density-of-states.

A major challenge here is obtaining unambiguous proof about the tip's spin-sensitivity, usually by measuring a reference with well known magnetic properties. A common way to achieve this, the preparation of metal films or islands

with a well-known magnetic domain pattern like iron stripes on a tungsten (110)-surface, can not be used on dilute magnetic semiconductors, since the annealing temperatures needed to create the nanostructure at the surface would destroy the magnetic properties of the DMS. In (In,Mn)As for example, MnAs clusters are formed at temperatures above 450 °C.

The ability to apply a magnetic field perpendicular to the surface opens up another way to study spin-polarization when there is a two-dimensional electron system (2DES) at the surface. Such a 2DES can occur naturally due to surface band-bending or can be induced by adsorbates or the tip potential. In a 2DES, a B-field parallel to the confinement direction will cause the sample's density-of-states to condense to Landau levels, a strong enough field will lift the spin degeneracy of the Landau levels (ZEEMANN-splitting) and create separate fully spin-polarized levels which can be distinguished by STS. This has been done on indium antimonide (110) in this research group to directly image the Quantum-Hall-transition in real space[40]. In such a measurement, spin-polarization should lead to asymmetric peak heights. Spin-sensitive STM/STS has been held back by the lack of a sufficient magnetic reference. The described measurements are a very promising next step in the course of our investigations on an atomic-scale understanding of magnetic coupling in dilute magnetic semiconductors.

Appendix A

MATLAB Code

General

This is the implementation of the model described in Chapter 5 in MATLAB (http://www.mathworks.com/). The user provides the parameters of the host material, the impurity and the tip. The function `ccalc` is then called with these parameters, the lateral tip-sample distance and the bias range for which the calculation should be done. The function returns the simulated current in arbitrary units.

Wherever possible, the code is written to work on vectors of input values, to make use of the optimizations MATLAB provides for vectorized operations.

ccalc

This is the only function that is called by the user. It is given the parameters of the problem and calculates the tunneling current for the given bias values. This function first calls `uBandbending` to calculate the amount of band-bending at the impurity position, caused by the tip potential. Then, `uImpurity` is called with these values, which returns the potential offset at the tip base point, caused by the switching charge. Both potentials are added up and used in a call to `currentModel`, which calculates the tunneling current.
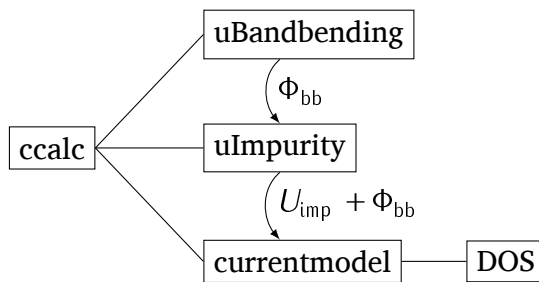
```matlab
1  function isim = ccalc(tip,semi,imp,dist,ubias)
2      % calculate current
3
4      % calculate local tip-induced potential and effective potential:
5      phibb = uBandbending(ubias,semi,imp,tip,dist);
6
7      % use calculated band-bending to determine impurity charge state and
8      % potential:
9      uimpattip = uImpurity(phibb,imp,semi,dist);
10     ueff = phibb-uimpattip;
11
12     % calculate tunneling current:
13     isim = currentModel(ubias,ueff,semi,tip);
14 end
```

uBandbending

This function is given the semiconductor-, impurity- and tip parameters, the lateral tip-sample distance and a vector of bias voltages for which to do the calculation. It first loads the pre-computed bias-dependent surface band-bending and depth of the depletion layer, e.g. from IVCHAR. Then it calculates the decay factor for the lateral decay, an approximation of the kind of decay described in [32]. Next, it uses the depth of the depletion layer to calculate the z-decay of the band-bending. The pre-calculated surface band-bending is multiplied by the two decay factors and returned.

```matlab
1  %% Tip-induced band-bending
2  % Returns the potential offset due to charge accumulation.
3  %
4  % Parameters are:
5  %
6  % * *ubias* - the applied bias
7  % * *semi* - semiconductor parameters of which we use
8  %         scrlen: screening length
9  % * *imp* - impurity parameters of which we use
10 %         depth: the depth of the impurity and
11 % * *tip* - tip parameters of which we use
12 %           td1,td2: shape parameters for tip-induced potential
13 % * *dist* - lateral tip-sample distance
```

```
14  %
15  % Output:
16  % * *out* - band-bending potential for each value in ubias
17  %
18  function out = uBandbending(ubias,semi,imp,tip,dist)
19      % Load simulated phism curve
20      load('ivchar.mat');
21
22      dist = abs(dist);
23      % approximate lateral run of tip-induced potential, in the spirit of
24      % Feenstra-paper: http://link.aip.org/link/?JVB/21/2080/1
25      latdecay = exp(-(5./semi.scrlen).*...
26          (dist.^2./(1./(dist./tip.td1)+tip.td2.*dist)));
27
28      % resample for our bias values
29      ddep = interp1(xiv_u',xiv_ddepl',ubias,'spline');
30      depdecay = exp(-imp.depth*6.9078./(ddep/10));
31
32      % resample surface band-bending (phism) for bias values
33      % result is product of surface potential, lateral- and depth-decay
34      out = latdecay*depdecay.*interp1(xiv_u',xiv_phism',ubias,'spline');
35  end
```

uImpurity

This function calculates the potential at the tip base point at the sample surface, caused by the impurity charge, depending on the external potential. The switching of the charge is emulated with `normcdf`, the normal cumulative distribution function which is part of MATLAB.

```
1   %% Impurity potential
2   % Returns the impurity potential.
3   % This models the impurity charge which switches depending on the local
4   % potential.
5   %
6   % Parameters are:
7   %
8   % * *ulocal* - the local potential, may be a vector
9   % * *imp* - impurity parameters of which we use
10  %        switch: the energy at which the impurity gets decharged
11  %         depth: the depth of the impurity and
12  %          soft: the broadening width for the transition
13  %       strength: the impurity potential
14  % * *semi* - semiconductor parameters of which we use
15  %           eps: dielectric constant
16  %        scrlen: screening length
17  %        Efermi: Fermi level
```

```
18  % * *latdist* - lateral distance between tip and impurity, may be a vector
19  %
20  % Output:
21  % * *out* = impurity-induced potential for each value of ulocal
22  %
23  function out = uImpurity(ulocal,imp,semi,latdist)
24      % calculate distance between tip and impurity:
25      dist = sqrt(imp.depth^2+latdist.^2);
26      % calculate screening: (1440mV=q/(4*pi*eps0*1nm))
27      impscreen = (1.440./(dist.*semi.eps)).*exp(-dist./semi.scrlen);
28      % output potential, broadened by imp.soft
29      out = impscreen*imp.strength*normcdf(ulocal,semi.Efermi-imp.switch,imp.soft);
30  end
```

currentModel

This function implements the current model. The current is calculated (line 37) according to Eq. 3.14 (page 28), with $\rho_t = \text{const}$. The integral is calculated as a sum going from the bottom of the conduction band (line 31) to the tip's Fermi level. The transmission coefficient (line 33) is calculated according to Eq. 3.15 (page 28).

```
1   %% Model of integrated density-of-states
2   % Returns the calculated current.
3   %
4   % Parameters are:
5   %
6   % * *ubias* - bias voltage, may be a vector
7   % * *phibb* - pre-calculated tip-induced band-bending vs. ubias
8   %              phibb(n): surface band-bending for ubias(n)
9   % * *semi* - semiconductor parameters of which we use
10  %              phi: work function
11  %           Efermi: Fermi level
12  %             EnCB: conduction band minimum
13  % * *tip* - tip parameters of which we use
14  %              phi: work function
15  %                z: z-distance between tip and sample
16  %
17  % Output:
18  % * *cur* - calculated current for each value in ubias
19  %
20  function cur = currentModel(ubias,phibb,semi,tip)
21      cur = zeros(size(ubias)); % preallocate array
22      du = ubias(2)-ubias(1);   %      -- ” --
23      phiavg = (semi.phi+tip.phi)/2; % mean barrier height
24      for i = 1:length(ubias)        % for each bias value
25          u = ubias(i)+semi.Efermi;
```

```
26          bb = phibb(i);              % obtain surface band-bending
27        if u > (semi.EnCB+bb)         % if bias is above conduction band minimum
28            % find a delta-u that fits an integer number of times in our interval:
29            duint = (u-(semi.EnCB+bb))/ceil((u-(semi.EnCB+bb))/du);
30            % create range vector from bottom of CB (modified by phibb) to u
31            uint = semi.EnCB+bb:duint:u;
32            % approximate T (0.324 ~ 2nm*sqrt(2me/(hbar^2)*1meV))
33            tmat = exp(-tip.z*0.324*sqrt(phiavg+u/2-uint));
34            % obtain density-of-states for our range:
35            dos = DOS(uint-bb,semi);
36            % numerically integrate:
37            cur(i) = sum(tmat.*dos)*duint;
38        else
39            cur(i) = 0;                % bias is below CB minimum, no current
40        end
41    end
42 end
```

DOS

This function calculates the unitless density-of-states of the parabolic conduction band. The density-of-states of a free three-dimensional electron gas is

$$D(E) = \frac{(2m)^{3/2}}{2\pi^2\hbar^3}\sqrt{E}$$

Since this is not a quantitative model, we can drop the constant factor and use

$$\rho_{\text{approx.}}(E) = \sqrt{(E)}$$

```
1  %% Model of integrated density-of-states
2  % Returns the density-of-states for the given energies in parabolic
3  % approximation
4  %
5  % Parameters are:
6  %
7  % * *energy* - energies to calculate for, may be a vector
8  % * *semi* - semiconductor parameters of which we use
9  %          EnCB: conduction band minimum
10 %
11 % Output:
12 % * *dos* - density-of-states for each value of ubias
13 function dos = DOS(energy,semi)
14     cb_offset = energy-semi.EnCB; % get offset from conduction band minimum
15     cb_offset = cb_offset.*(cb_offset > 0); % discard energies below min
16     dos = sqrt(cb_offset);
17 end
```

mkmodel

This function serves as an example for how the functions above can be used. It generates Figure 5.7 (page 75).

```matlab
%%  mkmodel -- calculate and graph I(U)-curves and dI/dU-curves for a single
%                 switching charge
%
% Parameters:
% * *final* - produce "final" high-quality output, takes more time

function mkmodel(final)
anno = 1; % produce annotations yes/no

%% Parameter definition

% potential diameters [nm]
widetip = 7.5;
narrowtip = 3;

semi.EnCB = 415;          % conduction band minimum [meV]
semi.phi = 5300;          % sample work function [meV]
semi.scrlen = 10;     % screening length [nm]
semi.eps = 14.6;          % dielectric constant
semi.Efermi = 14;         % Fermi level [meV]

tip.z = 1;                % tip-sample distance [nm]
tip.phi = 4380;           % tip work function [mV]
tip.td1 = 20;             % parameters for tip potential
tip.td2 = 3.5;

imp.switch = 28;          % impurity switching level [meV]
imp.strength = 1000;      % impurity potential [meV]
imp.depth = 0.43;         % impurity depth (0.215 nm per atomic layer)
imp.soft = 1.5;           % broadening of switching edge [meV]

load('colormaps');

% resolution parameters for the calculation:
if final    % high-resolution for final output
   du = 1;                   % resolution of ubias for curves
   imures = 2;               % resolution of ubias for images
   imuosres = 2;             % resolution of ubias for images, interpolated
   radres = 0.025;           % radial resolution for images (y-axis)
   radosres = 0.025;         % radial resolution for images (y-axis), interpolated
else         % lower resolution for drafts
   du = 4;
   imures = 20;
```

```
44      imuosres = 10;
45      radres = 0.5;
46      radosres = 0.1;
47  end
48
49  % calculate dI/dU(V)-curves for first panel:
50  di = []; i = [];
51
52  % lateral distances:
53  distances = [0 0.5 1.3 1.8 2.6];
54
55  % vector of bias values for current calculation
56  ubias=600:du:1400;
57
58  for dist = distances;                          % for each distance...
59      semi.tipscreen = widetip;                  % ... assume a wide tip
60      isim = ccalc(tip,semi,imp,dist,ubias);  % ... do calculation
61      di(:,end+1,1) = diff(isim)'/du;            % ... differentiate I
62      i(:,end+1,1) = isim';
    % ... shorten I vector by one
63      semi.tipscreen = narrowtip;
    % same as above for narrow tip
64      isim = ccalc(tip,semi,imp,dist,ubias);
65      di(:,end,2) = diff(isim)'/du;
66      i(:,end,2) = isim';
67      semi.tipscreen = widetip;
    % for comparison, calculate...
68      oldstrength = imp.strength;                % ... I(U) curve ...
69      imp.strength = 0;
    % ... without impurity effect
70      isim = ccalc(tip,semi,imp,dist,ubias);
71      i(:,end,3) = isim';
72      imp.strength = oldstrength;
73  end
74
75  % calculate ubias values for differentiated curves
76  ubiasd = (ubias(1)+du/2):du:ubias(end);
77
78  % create figure and position window on screen
79  f1 = findobj('type','figure','tag','fig:model');
80  if isempty(f1)
81      f1 = figure('units','centimeters','PaperSize',[8.487 14.7],'tag','fig:model');
82  else
83      clf(f1);
84      figure(f1);
85  end
86
```

```matlab
87  set(gcf,'units','centimeters','position',[0 0 8.5 13.7]);
88
89  % move window to top left corner:
90  set(gcf,'units','pixels');
91  winpos = get(gcf,'position');
92  screensize = get(0,'screensize');
93  winpos(2) = screensize(4)-winpos(4)-68;
94  winpos(1) = 2;
95  set(gcf,'position',winpos);
96  set(gcf,'units','centimeters');
97
98  % draw first panel:
99  ax1 = axes('units','centimeters','position',[0.8 9.34 7.5 4.12]);
100 set(gca,'fontname','charis sil','fontsize',10);
101 set(0,'DefaultAxesColorOrder',[1 0 0;0 0 1;0 1 0;1 0.5 0;0 0.5 0]);
102
103 % plot wide-tip dI/dU curve:
104 dplot = plot(ubiasd/1000,100000000*di(:,:,2),'linestyle',':');
105
106 % prepare annotation strings
107 distnames = {};
108 for n = 1:length(distances)
109     distnames{n} = sprintf('%.1f nm',distances(n));
110 end
111 distnames{1} = 'center';
112
113 setappdata(dplot(1),'anno',struct('text',distnames{1},'pos',[2.8 11.8],...
114     'fontname','charis sil'));
115 setappdata(dplot(2),'anno',struct('text',distnames{2},'pos',[2.75 11.0],...
116     'fontname','charis sil'));
117 setappdata(dplot(3),'anno',struct('text',distnames{3},'pos',[2.7 10.6],...
118     'fontname','charis sil'));
119 setappdata(dplot(4),'anno',struct('text',distnames{4},'pos',[2.6 10.35],...
120     'fontname','charis sil'));
121 setappdata(dplot(5),'anno',struct('text',distnames{5},'pos',[2.3 10.1],...
122     'fontname','charis sil'));
123 hold on;
124
125 % add narrow-tip dI/dU curve
126 plot(ubiasd/1000,100000000*di(:,:,1),'linestyle','-');
127 hold off;
128 set(gca,'ylim',[0 6.3]);
129
130 % tune dI/dU diagram:
131 for lin = get(gca,'children')
132     set(lin, 'linewidth', 1.0);
133 end
```

```
134  set(gca,'xtick',0.6:0.1:1.4,'xticklabel',[]);
135
136  if anno
137      ylabel('dI/dU (arb. units)');
138      pos = get(get(gca,'ylabel'),'position');
139      pos(1) = 0.5455;
140      set(get(gca,'ylabel'),'position',pos);
141  else
142      set(gca,'yticklabel',[]);
143  end
144
145  % drawing the current-inset in the first panel:
146  axes('units','centimeters','position',[4.5 11.4 3 1.7]);
147  set(gca,'fontname','charis sil','fontsize',10);
148
149  % plot reference curve without impurity
150  plot(ubias/1000,1000000*i(:,1,3),'linestyle',':','linewidth',1.0,'color',[0 0 0]);
151  hold on;
152  % plot curve with impurity
153  plot(ubias/1000,1000000*i(:,1,1),'linestyle','-','linewidth',1.0,'color',[0 0 0]);
154  xlim([0.78 1.1]);
155  ylim([0 5]);
156  set(gca,'xtick',0:0.1:3);
157  set(gca,'ytick',0:1:4);
158  set(gca,'yticklabel',{'0' '' '2' '' '4' '' });
159
160  if anno
161      text('units','centimeters','position',[0.6 0.4],'string','I(U) (arb. units)');
162  else
163      set(gca,'xticklabel',[]);
164  end
165
166  % annotation for dI/dU panel:
167  figax = axes('box','off','color','none',...
168          'units','normalized','position',[0 0 1 1],'visible','off');
169
170  lineanno(figax,dplot);
171
172  % Calculate the wide-tip waterfall:
173  di5 = []; i5 = [];
174  drange = 3;
175  semi.tipscreen = widetip;
176
177  % calculate I(U)-curves for each lateral distance:
178  distrange = drange:-radres:0;
179  du = imures;
180  ubias=600:du:1400;
```

```matlab
181  for dist = distrange
182      isim = ccalc(tip,semi,imp,dist,ubias);
183      di5(:,end+1) = diff(isim)'/du;
184      i5(:,end+1) = isim';
185  end
186  ubiasd = (ubias(1)+du/2):du:ubias(end);
187
188  colormap(cmjex);
189
190  % interpolate data
191  [XI,YI]=ndgrid(ubiasd(1):imuosres:ubiasd(end),drange:-radosres:0);
192  finedi5=interp2(ubiasd,distrange,di5',XI,YI,'cubic');
193  finedi5 = finedi5';
194  finedi52 = [finedi5; flipud(finedi5(1:end-1,:))];
195
196  % plot the wide-tip waterfall:
197  set(gcf,'nextplot','add');
198  ax2 = axes('units','centimeters','position',[0.8 5.22 7.5 4.12]);
199  set(gca,'fontname','charis sil','fontsize',10);
200  imd=util.real2rgb(100000000*finedi52,cmjex,[0.2 4.3]);
201
202  im = image(imd);
203  set(im,'xdata',[ubias(1) ubias(end)]/1000,'ydata',[-drange drange]);
204  set(gca,'xlim',[ubias(1)-0.5 ubias(end)+0.5]/1000,'ylim',[-drange drange]);
205  axis xy;
206  set(gca,'xtick',0.6:0.1:1.4,'xticklabel',[]);
207  set(gca,'ytick',-drange+1:1:drange);
208
209  if anno
210      ylabel('lateral distance r (nm)');
211      pos = get(get(gca,'ylabel'),'position');
212      pos(1) = 0.5455;
213      set(get(gca,'ylabel'),'position',pos);
214  else
215      set(gca,'yticklabel',[]);
216  end
217
218  % plot the tip potential shape inset into the waterfall:
219  xrng = get(gca,'xlim');
220  set(gca,'units','centimeters');
221  pos = [xrng(2)-0.35 -3 0.35 2.5];
222  rectangle('position',pos,'facecolor','w');
223  fpos = dsxy2figxy([1.05 0.5 0.35 2.5]);
224
225  axis ij;
226  axes('units','normalized','position',fpos + 0.03*[1.3 1.3 -2 -1.5]);
227  set(gca,'fontname','charis sil','fontsize',10);
```

```
228
229   % calculate tip potential:
230   X = -20:0.1:20;
231   semi.tipscreen = widetip;
232   dist = abs(X);latdecay = exp(-(5./semi.tipscreen).*...
233       (dist.^2./(1./(dist./tip.td1)+tip.td2.*dist)));
234   plot(X,latdecay,'-k','linewidth',1.5);
235   ylim([0 1.2]);
236   xlim([-11 11]);
237   set(gca,'xtick',-10:2:10);
238   set(gca,'ytick',0:0.2:1);
239   if anno
240       set(gca,'yticklabel',{'0','','','','','1' });
241       set(gca,'fontsize',6);
242       xlabel('lateral distance r (nm)');
243       h = get(gca,'xlabel');
244       pos = get(h,'pos');
245       pos = pos+[0 0.17 0];
246       set(h,'pos',pos);
247   else
248       set(gca,'yticklabel',[]);
249       set(gca,'xticklabel',[]);
250   end
251
252   % calculate the narrow-tip waterfall:
253   di3 = []; i3 = [];
254   drange = 3;
255   semi.tipscreen = narrowtip;
256
257   % calculate I(U)-curves for each lateral distance:
258   distrange = drange:-radres:0;
259   du = imures;
260   ubias=600:du:1400;
261   for dist = distrange
262       isim = ccalc(tip,semi,imp,dist,ubias);
263       di3(:,end+1) = diff(isim)'/du;
264       i3(:,end+1) = isim';
265   end
266   ubiasd = ((ubias(1)+ubias(2))/2):(ubias(2)-ubias(1)):ubias(end);
267
268   colormap(cmjex);
269
270   % interpolate data
271   [XI,YI]=ndgrid(ubiasd(1):imuosres:ubiasd(end),drange:-radosres:0);
272   finedi3=interp2(ubiasd,distrange,di3',XI,YI,'cubic');
273   finedi3 = finedi3';
274   finedi32 = [finedi3; flipud(finedi3(1:end-1,:))];
```

```
275
276   % plot the narrow-tip waterfall:
277   set(gcf,'nextplot','add');
278
279   ax3 = axes('units','centimeters','position',[0.8 1.1 7.5 4.12]);
280   set(gca,'fontname','charis sil','fontsize',10);
281
282   imd=util.real2rgb(100000000*finedi32,cmjex,[0.2 4.7]);
283   im = image(imd);
284
285   set(im,'xdata',[ubias(1) ubias(end)]/1000,'ydata',[-drange drange]);
286   set(gca,'xlim',[ubias(1)-0.5 ubias(end)+0.5]/1000,'ylim',[-drange drange]);
287
288   set(gca,'xtick',0.6:0.1:1.4);
289   set(gca,'ytick',-drange+1:1:drange);
290   set(gca,'clim',get(ax2,'clim'));
291
292   if anno
293       xlabel('U (V)')
294       ylabel('lateral distance r (nm)')
295       pos = get(get(gca,'ylabel'),'position');
296       pos(1) = 0.5455;
297       set(get(gca,'ylabel'),'position',pos);
298   else
299       set(gca,'yticklabel',[]);
300       set(gca,'xticklabel',[]);
301   end
302
303   % plot the tip potential shape inset into the waterfall:
304   xrng = get(gca,'xlim');
305   set(gca,'units','centimeters');
306   pos = [xrng(2)-0.35 -3 0.35 2.5];
307   ob = rectangle('position',pos,'facecolor','w');
308   uistack(ob,'top');
309   fpos = dsxy2figxy([1.05 0.5 0.35 2.5]);
310
311   axis ij;
312   axes('units','normalized','position',fpos + 0.03*[1.3 1.3 -2 -1.5]);
313   set(gca,'fontname','charis sil','fontsize',10);
314
315   % calculate tip potential:
316   X = -20:0.1:20;
317   semi.tipscreen = narrowtip;
318   dist = abs(X);latdecay = exp(-(5./semi.tipscreen).*...
319       (dist.^2./(1./(dist./tip.td1)+tip.td2.*dist)));
320   plot(X,latdecay,'-k','linewidth',1.5);
321   ylim([0 1.2]);
```

```matlab
322  xlim([-11 11]);
323  set(gca,'xtick',-10:2:10);
324  set(gca,'ytick',0:0.2:1);
325  if anno
326      set(gca,'yticklabel',{'0','','','','','1' });
327      set(gca,'fontsize',6);
328      xlabel('lateral distance r (nm)');
329      h = get(gca,'xlabel');
330      pos = get(h,'pos');
331      pos = pos+[0 0.17 0];
332      set(h,'pos',pos);
333  else
334      set(gca,'yticklabel',[]);
335      set(gca,'xticklabel',[]);
336  end
337
338  % produce colorbar in top diagram with scale matching the waterfall plots:
339  clims = [0.2 4.3];
340  cmin = clims(1);
341  cmax = clims(2);
342  pos = get(ax1,'pos');
343  height = pos(4);
344  ylims = get(ax1,'ylim');
345  yscale = abs(diff(ylims));
346  axes2i = axes('Parent',f1,'Tag','ax_main',...
347      'Units','centimeters',...
348      'Position',[0.8 9.34+height*cmin/yscale 0.4 height*cmax/yscale],...
349      'xlim',[0 1],'ylim',[0 1],...
350      'CLim',[-0.1 2.2]);
351  imagesc([0 1],[0 1],[256:-1:0]','Parent',axes2i,'CDataMapping','scaled');
352  set(axes2i,'box','off');
353  set(axes2i,'xtickmode','manual');
354  set(axes2i,'ytickmode','manual');
355  set(axes2i,'xtick',[]);
356  set(axes2i,'ytick',[]);
357
358  % save graphics file
359  if final
360      set(gcf,'paperpositionmode','auto');
361      print('-dmeta','-r1200','model');
362  end
```

Bibliography

[1]   Ioffe Physical Technical Institute, http://www.ioffe.rssi.ru/. 13

[2]   H. Akai. Ferromagnetism and Its Stability in the Diluted Magnetic Semiconductor (In, Mn)As. *Phys. Rev. Lett.*, **81**(14), 3002– (1998). 16

[3]   P. W. Anderson. Antiferromagnetism. Theory of Superexchange Interaction. *Physical Review*, **79**(2), 350–356 (1950). 7

[4]   N. Apsley and H. P. Hughes. Temperature- and field-dependence of hopping conduction in disordered systems. *Philosophical Magazine*, **30**, 963–972 (1974). 9

[5]   P. I. Arseev, N. S. Maslova, V. I. Panov, S. V. Savinov and C. van Haesendonck. Many-particle interaction in tunneling spectroscopy of impurity states on the InAs(110) surface. *JETP Lett.*, **77**, 172 (2003). 10

[6]   N. W. Ashcroft and N. D. Mermin. *Solid State Physics*. Saunders, Philadelphia (1976). 7, 8

[7]   A. Baldereschi and N. O. Lipari. Spherical Model of Shallow Acceptor States in Semiconductors. *Phys. Rev. B*, **8**(6), 2697–2709 (1973). 14, 15

[8]   J. Bardeen. Tunnelling from a Many-Particle Point of View. *Phys. Rev. Lett.*, **6**(2), 57–59 (1961). 22, 23

[9]   G. Bastard. *Wave Mechanics Applied to Semiconductor Heterostructures*. Les Ulis Cedex, France : Les Editions de Physique (1988). 89

[10]   G. Binnig and H. Rohrer. Scanning Tunneling Microscopy. *Helvetica Physica Acta*, **55**(6), 726 (1984). 2

[11]   G. Binnig and H. Rohrer. Scanning Tunneling Microscopy. *Physica B & C*, **127**(1-3), 37–45 (1984).

[12]   G. Binnig, H. Rohrer, C. Gerber and E. Weibel. Surface Studies by Scanning Tunneling Microscopy. *Phys. Rev. Lett.*, **49**(1), 57– (1982).

[13] G. Binnig, H. Rohrer, C. Gerber and E. Weibel. Tunneling through a controllable vacuum gap. *Appl. Phys. Lett.*, **40**(2), 178–180 (1982).

[14] G. Binnig, H. Rohrer, C. Gerber and E. Weibel. Vacuum tunneling. *Physica B &C*, **109-110**(Part 3), 2075 – 2077 (1982). ISSN 0378-4363. 16th International Conference on Low Temperature Physics. 2

[15] V. A. Bogdanova and N. A. Semikolenova. Photoluminescence Of Heavily Doped Gallium-Arsenide With An Ordered Distribution Of Impurity Complexes. *Soviet Physics Semiconductors-Ussr*, **26**(5), 460–462 (1992). 10

[16] C. Celebi, P. M. Koenraad, A. Y. Silov, W. V. Roy, A. M. Monakhov, J.-M. Tang and M. E. Flatté. Anisotropic spatial structure of deep acceptor states in GaAs and GaP. *Phys. Rev. B*, **77**(7), 075328 (2008). 10, 11, 89

[17] C. J. Chen. Theory of scanning tunneling spectroscopy. *J. Vac. Sci. Technol. A*, **6**, 319 (1988). 26, 28

[18] C. J. Chen. Tunneling matrix elements in three-dimensional space: The derivative rule and the sum rule. *Phys. Rev. B*, **42**(14), 8841–8857 (1990). 26

[19] C. J. Chen. Microscopic view of scanning tunneling microscopy. *J. Vac. Sci. Technol. A*, **9**(1), 44–50 (1991). 26

[20] S. A. Crooker and D. L. Smith. Imaging Spin Flows in Semiconductors Subject to Electric, Magnetic, and Strain Fields. *Phys. Rev. Lett.*, **94**(23), 236601 (2005). 89

[21] J. Czochralski. Ein Verfahren zur Messung der Kristallisationsgeschwindigkeit der Metalle. *Fresenius' Journal of Analytical Chemistry*, **57**(8), 373–374 (1918). 47

[22] J. E. Demuth, U. Koehler and R. J. Hamers. The STM learning curve and where it may take us. *J. Mic.*, **152**(2), 299–316 (1988). 26

[23] A. Depuydt, C. van Haesendonck, N. S. Maslova, V. I. Panov, S. V. Savinov and P. I. Arseev. Scanning tunneling microscopy and spectroscopy at low temperatures of the (110) surface of Te-doped GaAs single crystals. *Phys. Rev. B*, **60**(4), 2619 (1999). 9

[24] A. Depuydt, C. Van Haesendonck, S. Savinov and V. Panov. Low-temperature scanning tunneling microscopy of subsurface shallow dopants: depth dependence of the corrugation for the GaAs(110) surface. *Applied Physics A: Materials Science & Processing*, **72**(8), 209–212 (2001). 10

[25] R. Dombrowski. *Aufbau eines Ultrahochvakuum-Tieftemperatur-Rastertunnelmikroskops mit rotierbarem Magnetfeld und magnetfeldabhängige Rastertunnelspektroskopie an der InAs(110)-Oberfläche*. Ph.D. thesis, Universität Hamburg (1998). 38, 40

[26] P. Ebert. Defects in III-V semiconductor surfaces. *Appl. Phys. A,* **75**(1), 101–112 (2002). 74

[27] P. Ebert, B. Engels, P. Richard, K. Schroeder, S. Blügel, C. Domke, M. Heinrich and K. Urban. Contribution of Surface Resonances to Scanning Tunneling Microscopy Images: (110) Surfaces of III-V Semiconductors. *Phys. Rev. Lett.,* **77**(14), 2997–3000 (1996). 89

[28] K. W. Edmonds, P. Bogusławski, K. Y. Wang, R. P. Campion, S. N. Novikov, N. R. S. Farley, B. L. Gallagher, C. T. Foxon, M. Sawicki, T. Dietl, M. Buongiorno Nardelli and J. Bernholc. Mn Interstitial Diffusion in (Ga,Mn)As. *Phys. Rev. Lett.,* **92**(3), 037201– (2004). 15

[29] B. Engels. *Ab initio Berechnung der (110)-Oberfläche von III-V Halbleitern: Simulation von Rastertunnelmikroskopie-Aufnahmen.* Ph.D. thesis, RWTH Aachen (1992). 89

[30] B. Engels, P. Richard, K. Schroeder, S. Blügel, P. Ebert and K. Urban. Comparison between ab initio theory and scanning tunneling microscopy for (110) surfaces of III-V semiconductors. *Phys. Rev. B,* **58**(12), 7799–7815 (1998). 89

[31] R. Feenstra, J. A. Stroscio and A. Fein. Tunneling spectroscopy of the Si(111)2×1 surface. *Surface Science,* **181**(1-2), 295 – 306 (1987). ISSN 0039-6028. 29

[32] R. M. Feenstra. Electrostatic potential for a hyperbolic probe tip near a semiconductor. *J. Vac. Sci. Technol. B,* **21**(5), 2080–2088 (2003). 74, 106

[33] R. M. Feenstra, J. M. Woodall and G. D. Pettit. Observation of bulk defects by scanning tunneling microscopy and spectroscopy: Arsenic antisite defects in GaAs. *Phys. Rev. Lett.,* **71**(8), 1176–1179 (1993). 9, 57

[34] M. Fotino. Tip sharpening by normal and reverse electrochemical etching. *Rev. Sci. Instrum.,* **64**(1), 159–167 (1993). 45

[35] J. K. Furdyna and J. Kossut. *Semiconductors and Semimetals,* volume 25. Academic Press (1988). 5

[36] E. I. Georgitse, I. T. Postolaki, V. A. Smirnov and P. G. Untila. Photoluminescence of p-type InAs:Mn. *Soviet Physics–Semiconductors,* **23**, 469–70 (1989). 15

[37] J. Goodenough. Descriptions of outer d electrons in thiospinels. *Journal of Physics and Chemistry of Solids,* **30**, 261–280 (1969). 1

[38] J. B. Goodenough. An interpretation of the magnetic properties of the perovskite-type mixed crystals $La_{1-x}Sr_xCoO_{3-\lambda}$. *Journal of Physics and Chemistry of Solids,* **6**(2-3), 287 – 297 (1958). ISSN 0022-3697. 1, 7

[39] R. J. Hamers. Atomic-Resolution Surface Spectroscopy with the Scanning Tunneling Microscope. *Annual Review of Physical Chemistry*, **40**(1), 531–559 (1989). 30

[40] K. Hashimoto, C. Sohrmann, J. Wiebe, T. Inaoka, F. Meier, Y. Hirayama, R. A. Römer, R. Wiesendanger and M. Morgenstern. Quantum Hall Transition in Real Space: From Localized to Extended States. *Phys. Rev. Lett.*, **101**(25), 256802– (2008). 103

[41] D. Haude. *Rastertunnelspektroskopie auf der InAs(110)-Oberfläche : Untersuchungen an drei-, zwei- und nulldimensionalen Elektronensystemen im Magnetfeld.* Ph.D. thesis, Universität Hamburg (2001). 21

[42] A. J. Heinrich, J. A. Gupta, C. P. Lutz and D. M. Eigler. Single-Atom Spin-Flip Spectroscopy. *Science*, **306**(5695), 466–469 (2004). 102

[43] A. B. Henriques, N. F. O. Jr., S. A. Obukhov and V. A. Sanina. Giant negative magnetoresistance in a nonmagnetic semiconductor. *JETP Lett.*, **69**, 358–362 (1999). 15

[44] C. F. Hirjibehedin, C.-Y. Lin, A. F. Otte, M. Ternes, C. P. Lutz, B. A. Jones and A. J. Heinrich. Large Magnetic Anisotropy of a Single Atomic Spin Embedded in a Surface Molecular Network. *Science*, **317**(5842), 1199–1203 (2007). 102

[45] J.-M. Jancu, J.-C. Girard, M. O. Nestoklon, A. Lemaitre, F. Glas, Z. Z. Wang and P. Voisin. STM Images of Subsurface Mn Atoms in GaAs: Evidence of Hybridization of Surface and Impurity States. *Phys. Rev. Lett.*, **101**(19), 196801 (2008). 10, 11, 89

[46] J.-M. Jancu and P. Voisin. Tetragonal and trigonal deformations in zincblende semiconductors: A tight-binding point of view. *Phys. Rev. B*, **76**(11), 115202 (2007). 11

[47] T. Jungwirth, J. Sinova, J. Mašek, J. Kučera and A. H. MacDonald. Theory of ferromagnetic (III,Mn)V semiconductors. *Reviews of Modern Physics*, **78**(3), 809 (2006). 8

[48] T. Jungwirth, K. Y. Wang, J. Mašek, K. W. Edmonds, J. König, J. Sinova, M. Polini, N. A. Goncharuk, A. H. MacDonald, M. Sawicki, A. W. Rushforth, R. P. Campion, L. X. Zhao, C. T. Foxon and B. L. Gallagher. Prospects for high temperature ferromagnetism in (Ga,Mn)As semiconductors. *Phys. Rev. B*, **72**(16), 165204– (2005). 6

[49] J. Kanamori. Superexchange interaction and symmetry properties of electron orbitals. *Journal of Physics and Chemistry of Solids*, **10**(2-3), 87 – 98 (1959). ISSN 0022-3697. 7

[50] E. O. Kane. Basic concepts of tunneling. *Tunneling phenomena in solids* (1969). 21

[51] T. Kasuya. A Theory of Metallic Ferro- and Antiferromagnetism on Zener's Model. *Progress of Theoretical Physics,* **16**(1), 45–57 (1956). 8

[52] T. Kasuya and A. Yanase. Anomalous Transport Phenomena in Eu-Chalcogenide Alloys. *Rev. Mod. Phys.,* **40**(4), 684–696 (1968). 5

[53] A. Khajetoorians, B. Chilian, J. Wiebe, S. Schuwalow, F. Lechermann and R. Wiesendanger. *to be published.* 102

[54] D. Kitchen, A. Richardella, J.-M. Tang, M. E. Flatté and A. Yazdani. Atom-by-atom substitution of Mn in GaAs and visualization of their hole-mediated interactions. *Nature,* **442**(7101), 436–439 (2006). ISSN 0028-0836. 9, 10, 57, 85, 99

[55] D. S. Kitchen. *Atom-by-atom substitution of transition metals in GaAs and visualization of hole-mediated interactions.* Ph.D. thesis, University of Illinois at Urbana-Champaign (2006). 9

[56] J. Klijn. *Local density of states of the adsorbate-induced two-dimensional electron system studied at zero and strong magnetic fields.* Ph.D. thesis, Universität Hamburg (2003). 52, 53

[57] J. Klijn, L. Sacharow, C. Meyer, S. Blügel, M. Morgenstern and R. Wiesendanger. STM measurements on the InAs(110) surface directly compared with surface electronic structure calculations. *Phys. Rev. B,* **68**(20), 205327 (2003). 53, 89

[58] R. de Kort, M. C. M. M. van der Wielen, A. J. A. van Roij, W. Kets and H. van Kempen. Zn- and Cd-induced features at the GaAs(110) and InP(110) surfaces studied by low-temperature scanning tunneling microscopy. *Phys. Rev. B,* **63**(12), 125336 (2001). 10, 89

[59] K. C. Ku, S. J. Potashnik, R. F. Wang, S. H. Chun, P. Schiffer, N. Samarth, M. J. Seong, A. Mascarenhas, E. Johnston-Halperin, R. C. Myers, A. C. Gossard and D. D. Awschalom. Highly enhanced Curie temperature in low-temperature annealed [Ga,Mn]As epilayers. *Appl. Phys. Lett.,* **82**(14), 2302–2304 (2003). 7

[60] M. Linnarsson, E. Janzén, B. Monemar, M. Kleverman and A. Thilderkvist. Electronic structure of the GaAs:Mn$_{Ga}$ center. *Phys. Rev. B,* **55**(11), 6938–6944 (1997). 95

[61] S. Loth, M. Wenderoth, K. Teichmann and R. Ulbrich. Band structure related wave-function symmetry of amphoteric Si dopants in GaAs. *Solid State Commun.,* **145**(11-12), 551 – 555 (2008). ISSN 0038-1098. 89

[62]   S. Loth, M. Wenderoth and R. G. Ulbrich. Asymmetry of acceptor wave functions caused by surface-related strain and electric field in InAs. *Phys. Rev. B*, **77**(11), 115344 (2008). 10, 89, 99

[63]   S. Loth, M. Wenderoth, L. Winking, R. G. Ulbrich, S. Malzer and G. H. Döhler. Depth resolved scanning tunneling spectroscopy of shallow acceptors in galliumarsenide. *Jpn. J. Appl. Phys.*, **45**(3B), 2193–2196 (2006). 10, 89

[64]   S. Loth, M. Wenderoth, L. Winking, R. G. Ulbrich, S. Malzer and G. H. Döhler. Probing Semiconductor Gap States with Resonant Tunneling. *Phys. Rev. Lett.*, **96**(6), 066403 (2006). 82, 89

[65]   A. H. MacDonald, P. Schiffer and N. Samarth. Ferromagnetic semiconductors: moving beyond (Ga,Mn)As. *Nat. Mater.*, **4**(3), 195–202 (2005). ISSN 1476-1122. 7

[66]   O. Madelung. *Semiconductors: Data Handbook*. Springer-Verlag (2004). 13, 15

[67]   G. Mahieu, B. Grandidier, D. Deresmes, J. P. Nys, D. Stiévenard and P. Ebert. Direct Evidence for Shallow Acceptor States with Nonspherical Symmetry in GaAs. *Phys. Rev. Lett.*, **94**(2), 026407 (2005). 10, 89

[68]   F. Marczinowski, J. Wiebe, F. Meier, K. Hashimoto and R. Wiesendanger. Effect of charge manipulation on scanning tunneling spectra of single Mn acceptors in InAs. *Phys. Rev. B*, **77**(11), 115318 (2008). 61

[69]   F. Marczinowski, J. Wiebe, J.-M. Tang, M. Flatté, F. Meier, M. Morgenstern and R. Wiesendanger. Local Electronic Structure near Mn Acceptors in InAs: Surface-Induced Symmetry Breaking and Coupling to Host States. *Phys. Rev. Lett.*, **99**(15), 157202 (2007). 16, 83, 87, 98

[70]   F. Meier. *Co on Pt(111) studied by spin-polarized scanning tunneling microscopy and spectroscopy*. Ph.D. thesis, Universität Hamburg (2006). 41, 42

[71]   F. Meier, L. Zhou, J. Wiebe and R. Wiesendanger. Revealing Magnetic Interactions from Single-Atom Magnetization Curves. *Science*, **320**(5872), 82–86 (2008). 102

[72]   M. Millea, M. McColl and A. Silver. Electrical characterization of metal/InAs contacts. *J. Electron. Mater.*, **5**(3), 321–340 (1976). 52

[73]   A. M. Monakhova, N. I. Sablinaa, N. S. Averkieva, C. Çelebi and P. M. Koenraad. Spatial distribution of a hole localized on acceptor in deformed crystal. *Solid State Commun.*, **146**(9-10), 416–419 (2008). 89

[74]   M. Morgenstern. *Probing the Local Density of States of Dilute Electron Systems in Different Dimensions*, volume 10 (2002). 76

[75] N. F. Mott. *Philosophical Magazine*, **19**, 835 (1969). 9

[76] H. Munekata, H. Ohno, S. von Molnar, A. Segmüller, L. L. Chang and L. Esaki. Diluted magnetic III-V semiconductors. *Phys. Rev. Lett.*, **63**(17), 1849– (1989). 1, 6

[77] H. Ohno, D. Chiba, F. Matsukura, T. Omiya, E. Abe, T. Dietl, Y. Ohno and K. Ohtani. Electric-field control of ferromagnetism. *Nature*, **408**(6815), 944–946 (2000). ISSN 0028-0836. 1

[78] H. Ohno, A. Shen, F. Matsukura, A. Oiwa, A. Endo, S. Katsumoto and Y. Iye. (Ga,Mn)As: A new diluted magnetic semiconductor based on GaAs. *Appl. Phys. Lett.*, **69**(3), 363–365 (1996). 1, 6

[79] Y. Ohno, D. K. Young, B. Beschoten, F. Matsukura, H. Ohno and D. D. Awschalom. Electrical spin injection in a ferromagnetic semiconductor heterostructure. *Nature*, **402**(6763), 790–792 (1999). ISSN 0028-0836. 1

[80] J. Okabayashi, T. Mizokawa, D. D. Sarma, A. Fujimori, T. Slupinski, A. Oiwa and H. Munekata. Electronic structure of $In_{1-x}Mn_xAs$ studied by photoemission spectroscopy: Comparison with $Ga_{1-x}Mn_xAs$. *Phys. Rev. B*, **65**(16), 161203 (2002). 9

[81] K. Olejník, M. H. S. Owen, V. Novák, J. Mašek, A. C. Irvine, J. Wunderlich and T. Jungwirth. Enhanced annealing, high Curie temperature, and low-voltage gating in (Ga,Mn)As: A surface oxide control study. *Phys. Rev. B*, **78**(5), 054403– (2008). 2

[82] S. H. Pan. International Patent Publication Number WO 93/19494 (International Bureau, World Intellectual Property Organization), Hamburg, September 30. 1993. 43

[83] L. J. van der Pauw. A method of measuring specific resistivity and Hall effect of discs of arbitrary shape. *Philips Research Reports*, **13** (1958). 48

[84] S. Perraud, K. Kanisawa, Z.-Z. Wang and T. Fujisawa. Direct Measurement of the Binding Energy and Bohr Radius of a Single Hydrogenic Defect in a Semiconductor Quantum Well. *Phys. Rev. Lett.*, **100**(5), 056806 (2008). 89

[85] E. H. Rhoderick and R. H. Williams, editors. *Metal-Semiconductor Contacts*. Oxford University Press (1988). 52

[86] M. Rohlfing. Ph.D. thesis, Münster (1997). 89

[87] M. A. Ruderman and C. Kittel. Indirect Exchange Coupling of Nuclear Magnetic Moments by Conduction Electrons. *Phys. Rev. Lett.*, **96**(1), 99– (1954). 8

[88]   L. Sacharow. *Calculation of electronic and magnetic properties of hybrid low-dimensional structures*. Ph.D. thesis, Universität Hamburg (2006). 53

[89]   B. Sapoval and C. Hermann. *Physics of Semiconductors*. Springer-Verlag (1995). 36

[90]   M. Sawicki, D. Chiba, A. Korbecka, Y. Nishitani, J. A. Majewski, F. Matsukura, T. Dietl and H. Ohno. Experimental probing of the interplay between ferromagnetism and localization in (Ga, Mn)As. *Nature Physics*, **6**(1), 22–25 (2010). ISSN 1745-2473. 1, 6, 7

[91]   J. Schneider, U. Kaufmann, W. Wilkening, M. Baeumler and F. Köhl. Electronic structure of the neutral manganese acceptor in gallium arsenide. *Phys. Rev. Lett.*, **59**(2), 240– (1987). 16

[92]   A. Selloni, P. Carnevali, E. Tosatti and C. D. Chen. Voltage-dependent scanning-tunneling microscopy of a crystal surface: Graphite. *Phys. Rev. B*, **31**(4), 2602–2605 (1985). 28

[93]   B. L. Sheu, R. C. Myers, J.-M. Tang, N. Samarth, D. D. Awschalom, P. Schiffer and M. E. Flatté. Onset of Ferromagnetism in Low-Doped $Ga_{1-x}Mn_xAs$. *Phys. Rev. Lett.*, **99**(22), 227205 (2007). 8

[94]   Y. J. Song, S. C. Erwin, G. M. Rutter, P. N. First, N. B. Zhitenev and J. A. Stroscio. Making Mn Substitutional Impurities in InAs using a Scanning Tunneling Microscope. *Nano Lett.*, **9**(12), 4333–4337 (2009). ISSN 1530-6984. 57

[95]   J. A. Stroscio, R. M. Feenstra and A. P. Fein. Electronic Structure of the Si(111)2 × 1 Surface by Scanning-Tunneling Microscopy. *Phys. Rev. Lett.*, **57**(20), 2579–2582 (1986). 31

[96]   J. Szczytko, A. Twardowski, M. Palczewska, R. Jabłoński, J. Furdyna and H. Munekata. Electron paramagnetic resonance of Mn in $In_{1-x}Mn_xAs$ epilayers. *Phys. Rev. B*, **63**(8), 085315 (2001). 16, 48

[97]   J. Szczytko, A. Twardowski, K. Świątek, M. Palczewska, M. Tanaka, T. Hayashi and K. Ando. Mn impurity in $Ga_{1-x}Mn_xAs$ epilayers. *Phys. Rev. B*, **60**(11), 8304–8308 (1999). 16

[98]   M. Tanaka and Y. Higo. Large Tunneling Magnetoresistance in GaMnAs /AlAs /GaMnAs Ferromagnetic Semiconductor Tunnel Junctions. *Phys. Rev. Lett.*, **87**(2), 026602– (2001). 1

[99]   H. X. Tang, R. K. Kawakami, D. D. Awschalom and M. L. Roukes. Giant Planar Hall Effect in Epitaxial (Ga,Mn)As Devices. *Phys. Rev. Lett.*, **90**(10), 107201– (2003). 1

[100] J.-M. Tang and M. E. Flatté. Multiband Tight-Binding Model of Local Magnetism in $Ga_{1-x}Mn_xAs$. *Phys. Rev. Lett.*, **92**(4), 047201 (2004). 16, 90, 97, 98

[101] J.-M. Tang and M. E. Flatté. Spin-orientation-dependent spatial structure of a magnetic acceptor state in a zinc-blende semiconductor. *Phys. Rev. B*, **72**(16), 161315 (2005). 102

[102] J. Tersoff and D. R. Hamann. Theory and Application for the Scanning Tunneling Microscope. *Phys. Rev. Lett.*, **50**(25), 1998–2001 (1983). 24, 26

[103] J. Tersoff and D. R. Hamann. Theory of the scanning tunneling microscope. *Phys. Rev. B*, **31**(2), 805–813 (1985). 24, 26, 73

[104] A. Van Esch, L. Van Bockstal, J. De Boeck, G. Verbanck, A. S. van Steenbergen, P. J. Wellmann, B. Grietens, R. Bogaerts, F. Herlach and G. Borghs. Interplay between the magnetic and transport properties in the III-V diluted magnetic semiconductor $Ga_{1-x}Mn_xAs$. *Phys. Rev. B*, **56**(20), 13103– (1997). 9, 15

[105] A. Wachowiak. *Aufbau einer 300mK-Ultrahochvakuum-Rastertunnelmikroskopie-Anlage mit 14 Tesla Magnet und spinpolarisierte Rastertunnelspektroskopie an ferromagnetischen Fe-Inseln*. Ph.D. thesis, Universität Hamburg (2003). 40

[106] K. Y. Wang, K. W. Edmonds, R. P. Campion, B. L. Gallagher, N. R. S. Farley, C. T. Foxon, M. Sawicki, P. Boguslawski and T. Dietl. Influence of the Mn interstitial on the magnetic and transport properties of (Ga,Mn)As. *J. Appl. Phys.*, **95**(11), 6512–6514 (2004). 1, 15

[107] J. Wiebe. *Aufbau einer 300mK-Ultrahochvakuum-Rastertunnelmikroskopie-Anlage mit 14T-Magnet und Untersuchung eines stark ungeordneten zweidimensionalen Elektronensystems*. Ph.D. thesis, Universität Hamburg (2003). 20, 40

[108] J. Wiebe, C. Meyer, J. Klijn, M. Morgenstern and R. Wiesendanger. From quantized states to percolation: Scanning tunneling spectroscopy of a strongly disordered two-dimensional electron system. *Phys. Rev. B*, **68**(4), 041402 (2003). 76

[109] J. Wiebe, A. Wachowiak, F. Meier, D. Haude, T. Foster, M.Morgenstern and R. Wiesendanger. A 300 mK ultra-high vacuum scanning tunneling microscope for spin-resolvedspectroscopy at high energy resolution. *Rev. Sci. Instrum.*, **75**(11), 4871–4879 (2004). 40, 44

[110] R. Wiesendanger. *Scanning Probe Microscopy and Spectroscopy*. Cambridge University Press (1994). 27, 28

[111] A. P. Wijnheijmer, J. K. Garleff, K. Teichmann, M. Wenderoth, S. Loth, R. G. Ulbrich, P. A. Maksym, M. Roy and P. M. Koenraad. Enhanced Donor Binding Energy Close to a Semiconductor Surface. *Phys. Rev. Lett.*, **102**(16), 166101 (2009). 76, 79, 80, 89

[112] C. Wittneven. *Aufbau eines Ultrahochvakuum-Tieftemperatur-Rastertunnel-mikroskops mit rotierbarem Magnetfeld und Untersuchung der Streuzustände ion-isierter Dotieratome an InAs(110)*. Ph.D. thesis, Universität Hamburg (1998). 38, 39, 40

[113] C. Wittneven, R. Dombrowski, M. Morgenstern and R. Wiesendanger. Scattering States of Ionized Dopants Probed by Low Temperature Scanning Tunneling Spectroscopy. *Phys. Rev. Lett.*, **81**, 5616 (1998). 97

[114] C. Wittneven, R. Dombrowski, S. H. Pan and R. Wiesendanger. A low-temperature ultrahigh-vacuum scanning tunneling microscope with rotat-ablemagnetic field. *Rev. Sci. Instrum.*, **68**(10), 3806–3810 (1997). 38, 43

[115] U. Wurstbauer, M. Sperl, M. Soda, D. Neumaier, D. Schuh, G. Bayreuther, J. Zweck and W. Wegscheider. Ferromagnetic GaMnAs grown on (110) faced GaAs. *Appl. Phys. Lett.*, **92**(10), 102506 (2008). 15

[116] Y. B. Xu, E. T. M. Kernohan, M. Tselepi, J. A. C. Bland and S. Holmes. Single crystal Fe films grown on InAs(100) by molecular beam epitaxy. *Appl. Phys. Lett.*, **73**(3), 399–401 (1998). 52

[117] A. M. Yakunin, A. Y. Silov, P. M. Koenraad, J.-M. Tang, M. E. Flatté, J.-L. Primus, W. van Roy, J. De Boeck, A. M. Monakhov, K. S. Romanov, I. E. Panaiotti and N. S. Averkiev. Warping a single Mn acceptor wavefunction by straining the GaAs host. *Nat. Mater.*, **6**(7), 512–515 (2007). ISSN 1476-1122. 11, 89

[118] A. M. Yakunin, A. Y. Silov, P. M. Koenraad, J. H. Wolter, W. Van Roy, J. De Boeck, J.-M. Tang and M. E. Flatté. Spatial Structure of an Individual Mn Acceptor in GaAs. *Phys. Rev. Lett.*, **92**(21), 216806 (2004). 10, 16, 85

[119] K. Yosida. Magnetic Properties of Cu-Mn Alloys. *Physical Review*, **106**(5), 893– (1957). 8

[120] C. Zener. Interaction between the d-Shells in the Transition Metals. *Physical Review*, **81**(3), 440–444 (1951). 7

[121] C. Zener. Interaction between the d-Shells in the Transition Metals. II. Ferromagnetic Compounds of Manganese with Perovskite Structure. *Physical Review*, **82**(3), 403–405 (1951). 8

[122] L. Zhou, J. Wiebe, S. Lounis, E. Vedmedenko, F. Meier, S. Blügel, P. H. Dederichs and R. Wiesendanger. Strength and directionality of surface

Ruderman-Kittel-Kasuya-Yosida interaction mapped on the atomic scale. *Nature Physics*, **6**(3), 187–191 (2010). ISSN 1745-2473. 102

Publications

Articles:

F. Marczinowski, J. Wiebe, J.-M. Tang, M. Flatté, F. Meier, M. Morgenstern and R. Wiesendanger: *Local Electronic Structure near Mn Acceptors in InAs: Surface-induced Symmetry Breaking and Coupling to Host States.* Phys. Rev. Lett. **99**, 157202 (2007)

F. Marczinowski, J. Wiebe, F. Meier, K. Hashimoto and R. Wiesendanger: *Effect of Charge Manipulation on Scanning Tunneling Spectra of Single Mn Acceptors in InAs.* Phys. Rev. B **77**, 115318 (2008)

Talks and Conferences:

F. Marczinowski, J. Wiebe, F. Meier, K. Hashimoto, M. Morgenstern, R. Wiesendanger, J.-M. Tang and M. Flatté: *Scanning Tunneling Spectroscopy on Single Mn-acceptors in InAs.* 70. Frühjahrstagung der Deutschen Physikalischen Gesellschaft, Dresden, 2006 (Poster)

F. Marczinowski, J. Wiebe, J.-M. Tang, M. Flatté, M. Morgenstern and R. Wiesendanger: *The Mn Acceptor in InAs: Depth-Dependent Shape and Supression of the Conduction Band.* 71. Frühjahrstagung der Deutschen Physikalischen Gesellschaft, Regensburg, 2007 (Talk)

F. Marczinowski, F. Meier, J. Wiebe and R. Wiesendanger, *Switching the Charge of a Single Mn-Dopant in InAs with the STM in Experiment and Model.* 72. Frühjahrstagung der Deutschen Physikalischen Gesellschaft, Berlin, 2008 (Talk)

H. Gutzmann, A. Stemmann, F. Adler, J. Wiebe, F. Marczinowski, Ch. Heyn, W. Hansen and R. Wiesendanger: *STM investigation of MBE-grown GaMnAs.* 72. Frühjahrstagung der Deutschen Physikalischen Gesellschaft, Berlin, 2008 (Poster)

F. Marczinowski, J. Wiebe, F. Meier, K. Hashimoto, R. Wiesendanger, J.-M. Tang and M. Flatté: *Scanning Tunneling Spectroscopy Study on Individual Mn-Acceptors in InAs.* ICN + T'06 Basel, Schweiz (Talk)

F. Marczinowski, J. Wiebe, R. Wiesendanger: *Rastertunnelspektroskopie an Mn-Akzeptoren in InAs.* Seminar über Methoden der Festkörper- und Halbleiterphysik, IV. Physikalisches Institut, Universität Göttingen, 2006 (Invited seminar talk)

F. Marczinowski, J. Wiebe, F. Meier, K. Hashimoto, M. Morgenstern and R. Wiesendanger: *Switching the Charge of a Single Mn-Acceptor below InAs(110): STS Study and Simple Model.* ICN + T'08 Keystone, Colorado, USA (Talk)

Danksagung

Allen voran danke ich Jens Wiebe, für die umfassende und gründliche Betreuung sämtlicher Phasen meiner Promotion und für seine endlose Geduld, die ich nicht für selbstverständlich halte.

Ich danke Prof. Dr. Roland Wiesendanger für die Möglichkeit, meine Doktorarbeit in diesem hervorragenden wissenschaftlichen Umfeld anzufertigen, und für die fortwährende Unterstützung.

Ich danke Alex Khajetoorians für viele wertvolle Hinweise und Unmengen sprachliche Verbesserungen, sowie dafür, daß er ein wirklich gutes Vorbild ist.

Focko Meier, Stefan Kuck, Jens Brede und allen anderen Mitgliedern der Gruppe R danke ich für die produktive und immer angenehme Zusammenarbeit.

Sebastian Loth und Martin Wenderoth danke ich für die anregenden und produktiven Gespräche. Ole Albrecht danke ich für die SQUID-Messungen an unseren Proben.

Martin Janson danke ich für den Anstoß, mich so intensiv mit MATLAB zu beschäftigen und dafür, daß er das SPAM-Projekt in meine Obhut übergeben hat.